MASTER THESIS

Characterization of Multi-transiting Planetary Systems with Transit Timing Variations

Kento MASUDA

A thesis submitted to
the graduate school of science,
the University of Tokyo
in partial fulfillment of
the requirements for the degree
of
Master of Science in Physics

January, 2014

Abstract

As of December 2013, about 1000 planets orbiting around stars other than the Sun have been discovered on the basis of various direct and indirect methods. Characterization of such *exoplanets* is one of the most important issues in planetary science.

A group of planets called *transiting planets* is the most suitable for such characterization. These planets have edge-on orbits with respect to our line of sight, and so they periodically go across the stellar disks and partially block the lights from their host stars. The resulting variation of the stellar brightness allows us to infer the existence of the planets, even though they themselves are not identified separately. The depth of the planetary transit enables us to estimate the planetary radius, which is vital for discussing density, and hence internal structure of the planet. Since the launch of the *Kepler* space telescope in 2009, the number of known transiting exoplanets has significantly increased and exceeded 3000 including the planet candidates that have no constraint on their masses.

In spite of the above advantage for characterization, the masses of transiting exoplanets are not easy to determine. They are usually estimated by measuring the *radial velocities* (RVs) of the host star induced by the planet through the Doppler shift in the stellar spectral lines. Most of the *Kepler* target stars, however, are so distant and faint that they are not suitable for spectroscopic observations.

Fortunately, if there are *multiple* transiting planets in a system (*multi-transiting planetary system*), we can estimate the planetary mass with photometric observations alone. The motion of such planets exhibit small departure from the periodic Keplerian motion due to their mutual gravitational interaction, and so their transit times deviate from the strict periodicity; these deviations are called *transit timing variations* (TTVs). Since TTVs come from the planet-planet gravitational interaction, we can estimate the planetary parameters including their masses by constructing the dynamical model for each specific system. Characterization with TTVs is complementary to, or even better than, that with RVs, and will contribute significantly to the analysis of substantial amount of *Kepler* data, as well as those expected from future space transit missions.

In this thesis, we characterize the two multi-transiting planetary systems discovered by *Kepler*, the Kepler Object of Interest (KOI) 94 system and the Kepler-51 system, with the analysis of TTVs. Through these analyses, we aim to establish the reliability and limitation of this valuable method and to identify the tasks that should be addressed for its future application.

The KOI-94 system hosts four transiting planets with closely-packed orbits. Since the RVs have already been obtained for this system, comparison of the independent constraints on the system parameters from TTVs with those from RVs works as a valuable test to examine the reliability and limitation of both methods. After making sure that the effect from the innermost and smallest planet KOI-94b is negligible, we numerically fit

the observed TTVs of the other three planets in this system, KOI-94c, KOI-94d, and KOI-94e, and obtain the best-fit parameters including their masses, $m_{\rm c} = 9.4^{+2.4}_{-2.1} M_\oplus$, $m_{\rm d} = 52.1^{+6.9}_{-7.1} M_\oplus$, and $m_{\rm e} = 13.0^{+2.5}_{-2.1} M_\oplus$. While these values are mostly in agreement with the previous RV study, the mass of KOI-94d estimated from TTVs is significantly smaller than the RV value $m_{\rm d} = 106 \pm 11 M_\oplus$. This discrepancy poses a general question about possible systematics in either (or both) of the methods. In addition, we find that the TTV of the outermost planet KOI-94e is not well reproduced in the current modeling, suggesting the existence of another perturber that has evaded the detection so far.

The other system in which we perform a similar TTV analysis, the Kepler-51 system, consists of two confirmed transiting planets, Kepler-51b and Kepler-51c, and one transiting planet candidate KOI-620.02. Our analysis shows that their TTVs are consistently explained by the three-planet model, and constrains their masses as $m_{\rm b} = 2.1^{+1.5}_{-0.8} M_\oplus$, $m_{\rm c} = 4.0 \pm 0.4 M_\oplus$, and $m_{02} = 7.6 \pm 1.1 M_\oplus$, thus confirming KOI-620.02 as a real planet in this system. Combining these masses with their radii determined from the transit light curves, we find that all the three planets in this system are the lowest-density planets ever discovered, having $\rho_p \lesssim 0.05\,{\rm g\,cm^{-3}}$. These results may provide a powerful constraint on the theory of planet formation, since it is difficult to explain such low densities with the current model.

Remarkably, both of the two systems analyzed in this thesis are compact multi-transiting planetary systems with low-density planets. They serve as additional evidences of the recently-recognized feature that the planets characterized with TTVs tend to have lower densities than those confirmed with RVs. We discuss possible origins of this feature, referring to the remaining tasks related to the study of TTVs.

Contents

Chapter 1

Introduction

It was not until 1990s that the planetary science changed from the study of *the* solar system to that of *planetary systems*. The discovery of *exoplanets*, planets orbiting around stars other than the Sun, has revolutionized our conventional view of the planetary system, which was merely based on our solar system alone.

Many of the exoplanets indeed show the properties that are quite different from the solar-system planets: the first exoplanet discovered around a Sun-like star, 51 Pegasi b, was a Jupiter-sized planet with the orbital period of as short as ~ 4 days (Mayor and Queloz 1995). This class of planets is dubbed "hot Jupiters," and now estimated to occur around $\sim 1\%$ of F, G, and K dwarfs in the solar neighborhood (Wright et al. 2012). Other amazing examples include the planets on highly eccentric (*e.g.*, Naef et al. 2001) or retrograde (Narita et al. 2009; Winn et al. 2009) orbits, which are far from the concentric and coplanar architecture of our solar system. Now we know that the planets exist even around binary stars; such planets are called circumbinary planets (*e.g.*, Doyle et al. 2011).

While unexpected discoveries are still ongoing, the exoplanetary science has now entered the era of characterization. As of December 2013, about 1000 exoplanets have been confirmed around nearly 800 stars, and more than 100 planets are still being confirmed every year (Figure 1.1). Most of these planets were discovered with *radial velocity* (RV) technique (Lovis and Fischer 2011) and *transit* method (Winn 2011). The former spectroscopically observes the line-of-sight component of the stellar reflex motion induced by the planet, measuring the Doppler shift of the stellar spectral lines very precisely. The latter photometrically detects the decrease in the stellar flux that occurs when a planet on the edge-on orbit goes across the stellar disk (Figure 1.2).

In fact, the latter *transiting planets* are the easiest targets for their characterization. Since the fractional dimming during the transit is given by the ratio of the area of the planetary disk to that of the stellar disk, one can estimate the radii of transiting planets, which are difficult or even impossible to measure for non-transiting planets. Combining these radii with the planetary masses estimated from the dynamical methods including the RV observations, we can constrain the mean densities of the planets, which are invaluable in discussing their compositions or formation histories. Transiting planets are also suitable for the study of planetary compositions, because we can measure their atmospheric compositions by observing the lights that graze their upper atmospheres.

As is clear from Figure 1.1, the number of known transiting planets has substantially increased in the past several years. This is due to the advent of the *Kepler* space telescope (Borucki et al. 2010, 2011; Batalha et al. 2013; Burke et al. 2013). *Kepler* is implemented

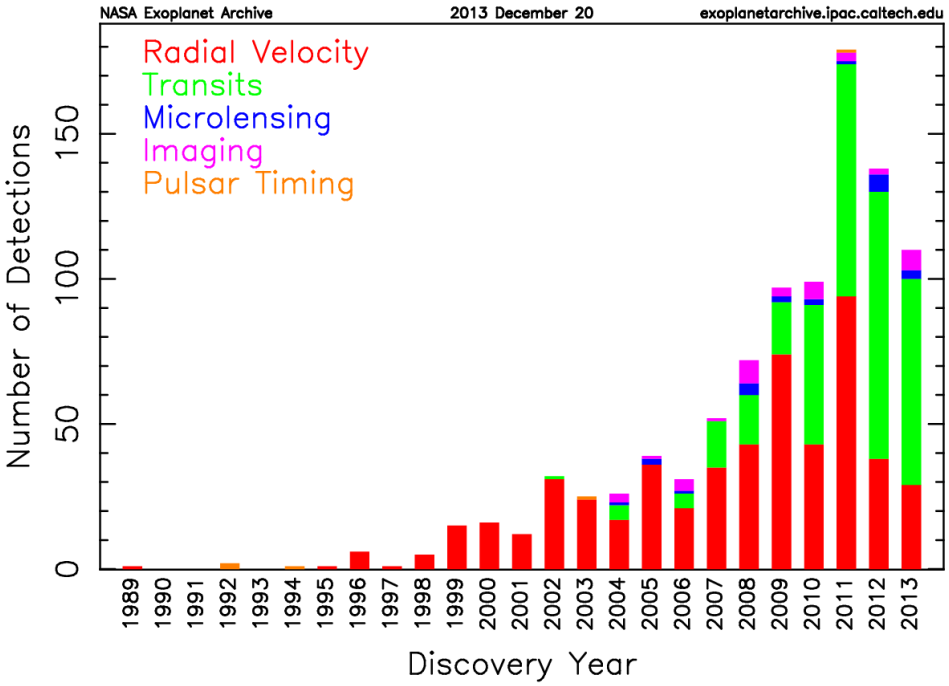

Figure 1.1 Number of exoplanets discovered each year. Different colors correspond to the different detection methods. Figure taken from NASA Exoplanet Archive `http://exoplanetarchive.ipac.caltech.edu/index.html`.

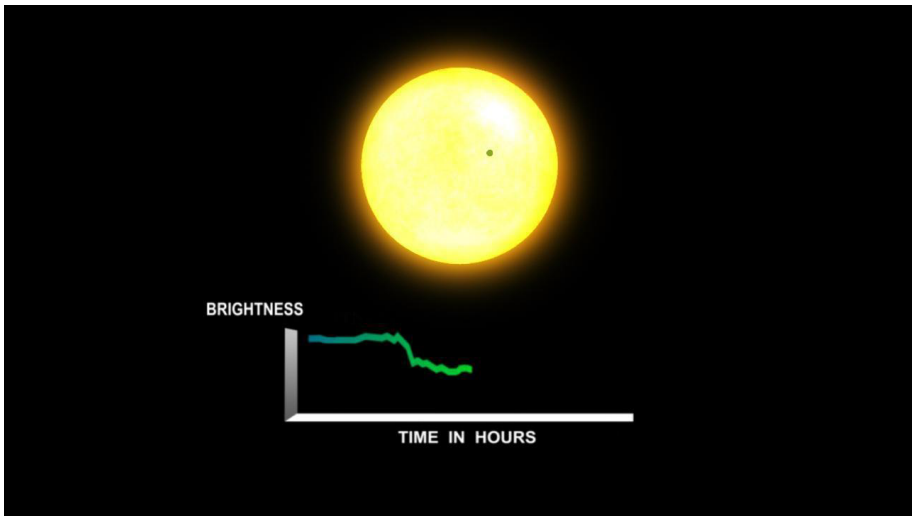

Figure 1.2 Schematic illustration of the planetary transit. Figure taken from the mission page of *Kepler* `http://kepler.nasa.gov`.

with a differential photometer with a wide (115 square degrees) field of view, and monitors the brightnesses of ~ 150000 main-sequence stars continuously and simultaneously. Since its launch in 2009, *Kepler* has found more than 3000 transiting planet candidates, for which Kepler-Object-of-Interest (KOI) numbers are given. As of December 2013, about 200 of the KOIs have been *confirmed* as real planets by determining their masses (or mass upper limits) and eliminating all the possible false positives; these planets are given Kepler numbers.[1]

A wealth of the *Kepler* data has not only made it possible to discuss the statistics of exoplanets (Howard 2013), but also revealed unprecedented planetary systems and phenomena; these include the first circumbinary planets (Doyle et al. 2011), the first planet-planet eclipse (Hirano et al. 2012a, see also Chapter 5 of this thesis), the first Earth-sized planet with an Earth-like density (Pepe et al. 2013; Howard et al. 2013), and a compact analogue to the solar system with seven planets packed inside the orbit of Venus (Cabrera et al. 2013). Continuous flux data taken by *Kepler* is not only valuable for the study of planets, but also for the stellar astrophysics; the stellar seismology has recently been shown to provide a way to accurately determine the stellar parameters (Huber et al. 2013b; Chaplin et al. 2014), and triggered several important discoveries in the field of exoplanetary science (Chaplin et al. 2013; Huber et al. 2013a).

This thesis mainly concerns another important outcome of *Kepler*: the discovery of many *multi-transiting* systems, the planetary systems that host more than one transiting planets. Indeed, more than one third of the planets discovered by *Kepler* belong to multi-transiting systems (Batalha et al. 2013). Characterization of such multi-planetary systems (not necessarily transiting) are especially valuable because reproducing the architecture of multiple planets is theoretically more demanding than a single planet, and hence the resulting constraints on the formation theories become much tighter.

In spite of its vital importance, characterization of these multi-transiting systems is not easy in a conventional manner. Although the transiting planets provide a wealth of information on the geometry of their orbits as well as their radii, the shape of the transit light curve (flux variation during the transit) contains no information on their masses. Thus, the RV observations of their host stars are required to determine their masses and to discuss their properties. It is, however, practically impossible to apply the spectroscopy to a major fraction of the *Kepler* systems, because their host stars are very distant and faint. Even if RVs are successfully observed, it is difficult to separate the contributions from multiple planets in the limited time sampling (*e.g.*, Rodigas and Hinz 2009; Anglada-Escudé et al. 2010; Wittenmyer et al. 2013).

Fortunately, multi-transiting systems exhibit a notable phenomenon that provides another method of characterization that is complementary to, or even better than, RVs: *transit timing variations* (TTVs, Miralda-Escudé 2002; Holman and Murray 2005; Agol et al. 2005), deviations of transit times from the strict periodicity due to the mutual gravitational interaction among the planets. By modeling the TTVs of several transiting planets consistently, one can precisely estimate their masses with photometric observations alone (*e.g.*, Lissauer et al. 2011). This makes it possible to apply the TTV method to

[1]Planet candidates in each KOI system are designated with the numbers after the decimal point beginning from 01, like KOI-94.01. These numbers are just given in the order of their discoveries, and have nothing to do with their distances from the host star. On the other hand, planets in confirmed systems are named as b, c, d, $\cdots$, in the increasing order of their distances from the star, like Kepler-89d. The letter a is preserved for the host star, but rarely used in reality.

multi-transiting systems for which RVs can never be obtained. In addition, TTVs are sensitive to low-mass planets below the current RV detection limit, as well as non-transiting planets (*e.g.,* Nesvorný et al. 2012). For these reasons, the TTV analysis is currently the most ideal (and often the only possible) method to characterize the substantial amount of candidate multi-planetary systems discovered by *Kepler*. Future contribution of this method is also promising, given the significant increase of data expected from the succeeding space transit missions like Transiting Exoplanet Survey Satellite (TESS).

In this thesis, we use the TTVs to characterize two of the multi-transiting systems found by *Kepler*, the KOI-94 (Kepler-89) system (Chapter 5)[2] and the Kepler-51 system (Chapter 6). We perform detailed dynamical modeling of these two systems with the aid of the numerical orbit integrations, and give constraints on the system parameters including the planetary masses. Through these analyses, we aim to evaluate the reliability and limitation of this valuable method and to identify remained tasks that should be addressed for its future application.

The plan of this thesis is as follows. We first give a brief summary of the transit method in Chapter 2. Here we fix terminology and definitions of the symbols used in later chapters, and discuss what can be inferred from the analysis of the transit light curves. Chapter 3 is the review of the TTV technique. After a brief overview of this method, we describe the physical background of this phenomenon, focusing on the recent analytic formulation. We also give a list of the *Kepler* planets confirmed using TTVs for future detailed study of these planets, as well as for the statistical discussion in Chapter 7. Chapter 4 is devoted to the description of the numerical methods we use in analyzing TTV signals. In addition to the basic description of the methods, we give some tips on applying them to the planetary orbit determination for practical use. We then apply the methods established in the preceding chapters to the KOI-94 (Kepler-89) system (Chapter 5) and the Kepler-51 system (Chapter 6). Finally, in Chapter 7, we summarize our findings in these two systems and discuss the general feature of the planets confirmed with TTVs in comparison with those characterized with other methods. We also examine possible origins of this feature, identifying future tasks in the study of TTVs.

[2]Since our analysis reliably determined the masses of the planets in this system, KOI-94 was assigned the Kepler number 89 after the publication of the results in Chapter 5.

Chapter 2

Transit Method for Exoplanets

When the orbit of a planet is edge on as seen from our line of sight, it periodically goes across its host star and causes a periodic decrease in the stellar flux. This phenomenon is called *planetary transit*, and the analysis of the flux variation during the planetary transit (*transit light curve*) provides geometric information on the planet and its orbit, including the planetary radius. In addition, spectroscopic observations of transiting planets lead to the precious knowledge about their atmospheric compositions and stellar obliquities, which are in most cases inaccessible for non-transit planets.

In this chapter, we briefly review the transit method, focusing on the modeling of transit light curves, definitions of the transit parameters that determine their shapes, and physical quantities that can be extracted from transit (sometimes combined with spectroscopic) observations. We also discuss the achievable precision of transit parameters and present simple analytic formulae based on the Fisher matrix analysis.

2.1 Keplerian Orbit

2.1.1 Solution of the Kepler Problem

Here we briefly summarize the solution of the two-body problem to fix the notation used in later chapters. The bodies are regarded as point masses denoted by subscripts 1 and 2, and only the Newtonian gravitational force is considered.

We begin with the equations of motion

$$m_1 \ddot{\boldsymbol{r}}_1 = +G\frac{m_1 m_2}{|\boldsymbol{r}|^3}\boldsymbol{r}, \tag{2.1}$$

$$m_2 \ddot{\boldsymbol{r}}_2 = -G\frac{m_1 m_2}{|\boldsymbol{r}|^3}\boldsymbol{r}, \tag{2.2}$$

where m_j and $\boldsymbol{r}_j$ are the mass and position vector of the j-th body, G is Newton's gravitational constant, and we define

$$\boldsymbol{r} = \boldsymbol{r}_2 - \boldsymbol{r}_1. \tag{2.3}$$

The sum of Equations (2.1) and (2.2) implies the conservation of the total linear momentum:

$$\boldsymbol{P} \equiv m_1 \dot{\boldsymbol{r}}_1 + m_2 \dot{\boldsymbol{r}}_2 = \text{const}, \tag{2.4}$$

and their difference gives the equation for the relative motion:

$$\ddot{\boldsymbol{r}} = -\frac{GM}{r^3}\boldsymbol{r}, \tag{2.5}$$

where $M \equiv m_1 + m_2$ and $r \equiv |\boldsymbol{r}|$. Since the right-hand side of Equation (2.5) is parallel to $\boldsymbol{r}$, this equation leads to the (specific) angular momentum conservation:

$$\boldsymbol{h} \equiv \boldsymbol{r} \times \dot{\boldsymbol{r}} = \text{const.} \tag{2.6}$$

This means that the relative motion is confined in a plane that is perpendicular to $\boldsymbol{h}$.

Let us solve Equation (2.5) in a polar coordinate system (r, θ). The radial component reduces to

$$\ddot{r} - r\dot{\theta}^2 = -\frac{GM}{r^2}, \tag{2.7}$$

and the azimuthal component reproduces Equation (2.6)

$$h = r^2\dot{\theta} = \text{const}, \tag{2.8}$$

which corresponds to Kepler's second law. Equation (2.8) can be used to eliminate $\dot{\theta}$ in Equation (2.7) to yield the equation for r alone:

$$\ddot{r} - \frac{h^2}{r^3} = -\frac{GM}{r^2}. \tag{2.9}$$

The solution of Equation (2.9) as a function of θ can be obtained by changing the variable from $r(\theta)$ to $u(\theta) \equiv 1/r(\theta)$. The resulting equation for $u(\theta)$ is

$$\ddot{u} + u = \frac{GM}{h^2}, \tag{2.10}$$

which has a general solution of the form

$$r(\theta) = \frac{1}{u(\theta)} = \frac{h^2/GM}{1 + e\cos(\theta - \varpi)}, \tag{2.11}$$

where e and ϖ are constants of integration. Equation (2.11) is the equation of conic sections, and represents the solution bound to $r < \infty$ (*i.e.*, ellipses) when $0 \leq e < 1$. In this case, we can define

$$a = \frac{h^2/GM}{1 - e^2} \tag{2.12}$$

to rewrite Equation (2.11) as

$$r = \frac{a(1 - e^2)}{1 + e\cos(\theta - \varpi)} = \frac{a(1 - e^2)}{1 + e\cos f}. \tag{2.13}$$

The constants a, e, and ϖ have clear geometrical meanings: a and e are the *semi-major axis* and *eccentricity* of the elliptical orbit, and ϖ denotes the angular position of the *periastron*, at which r takes the smallest value, $a(1 - e)$. This geometry is shown in

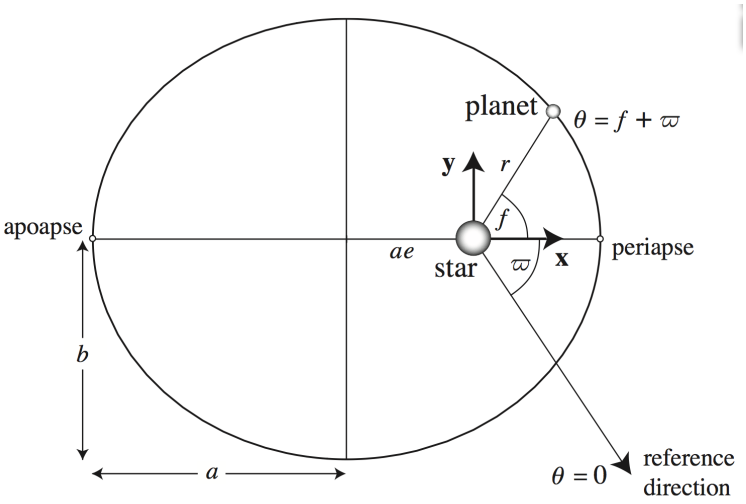

Figure 2.1 Geometry of the ellipse. In this figure, "star" and "planet" correspond to the bodies with masses m_1 and m_2, respectively. Figure taken from Murray and Correia (2011).

Figure 2.1. The angles ϖ, θ, and $f \equiv \theta - \varpi$ are called the *longitude of periastron*, *true longitude*, and *true anomaly*, respectively. It should be noted that the term longitude is used for the angular position measured from the reference line fixed in the space; on the other hand, the anomaly is measured from the periastron of the orbit, which changes its position in the presence of non-Keplerian forces. Choosing x- and y-axes as in Figure 2.1 (and z-axis in the direction of $\boldsymbol{x} \times \boldsymbol{y}$), the position vector of the planet (mass m_2) relative to the star (mass m_1) is given by

$$\boldsymbol{r} = r\cos f\hat{\boldsymbol{x}} + r\sin f\hat{\boldsymbol{y}} + 0\hat{\boldsymbol{z}}, \tag{2.14}$$

where the caret indicates the unit vector.

The area of the ellipse in Figure 2.1 is $\pi a^2\sqrt{1-e^2}$, while the area swept by the vector $\boldsymbol{r}$ per unit time is $r^2\dot{\theta}/2 = h/2$. Thus, the *orbital period* P is given by

$$P = \frac{\pi a^2\sqrt{1-e^2}}{h/2} = \sqrt{\frac{4\pi^2 a^4(1-e^2)}{GMa(1-e^2)}} = \sqrt{\frac{4\pi^2 a^3}{GM}}. \tag{2.15}$$

Defining the *mean motion* $n \equiv 2\pi/P$ of the planet, Equation (2.15) can be rewritten as

$$n^2 a^3 = GM = G(m_1 + m_2). \tag{2.16}$$

This represents Kepler's third law.

For the solution as a function of time t, we make use of the energy conservation law. Integrating Equation (2.5), we obtain

$$\frac{1}{2}|\dot{\boldsymbol{r}}|^2 - \frac{GM}{r} = C, \tag{2.17}$$

where C is a constant. The constant C can be determined in terms of orbital elements by calculating the value of $|\dot{\boldsymbol{r}}|^2$ at the periastron ($\theta = \varpi$ or $f = 0$), where $r = a(1-e)$.

Recalling that

$$|\dot{\boldsymbol{r}}|^2 = \dot{r}^2 + r^2\dot{f}^2 = \frac{h^2}{r^2}\left(1 + \frac{\dot{r}^2}{r^2\dot{f}^2}\right) \tag{2.18}$$

and that

$$\dot{r} = \frac{e\sin f}{1 + e\cos f}\, r\dot{f}, \tag{2.19}$$

we have

$$|\dot{\boldsymbol{r}}|^2_{f=0} = \frac{GMa(1-e^2)}{a^2(1-e)^2} = \frac{GM(1+e)}{a(1-e)}. \tag{2.20}$$

Substituting Equation (2.20) into Equation (2.17) and setting $f = 0$, the constant C is given as

$$C = \frac{GM}{a(1-e)}\left(\frac{1+e}{2} - 1\right) = -\frac{GM}{2a}. \tag{2.21}$$

Thus, from Equation (2.17), we obtain the equation of motion for r as

$$\dot{r} = \sqrt{2\left(C + \frac{GM}{r}\right) - \frac{h^2}{r^2}} = \frac{na}{r}\sqrt{(ae)^2 - (r-a)^2}, \tag{2.22}$$

where we use Equation (2.12) and Kepler's third law. In order to solve Equation (2.22), we introduce the *eccentric anomaly* E by

$$r = a(1 - e\cos E). \tag{2.23}$$

Then, Equation (2.22) reduces to

$$n = (1 - e\cos E)\dot{E}, \tag{2.24}$$

which can be integrated immediately to give *Kepler's equation*

$$M = E - e\sin E. \tag{2.25}$$

Here, we define the *mean anomaly* M via

$$M = n(t - \tau), \tag{2.26}$$

where τ is the time when $E = 0$, *i.e.*, the time of the periastron passage. Now we can find the orbital position at a given time, $\boldsymbol{r}(t)$, according to the following steps: (i) From time t, calculate M using Equation (2.26), (ii) Solve Equation (2.25) to find E using an appropriate numerical method, (iii) Use Equation (2.23) to relate this E to r, and (iv) Find f from Equation (2.13).

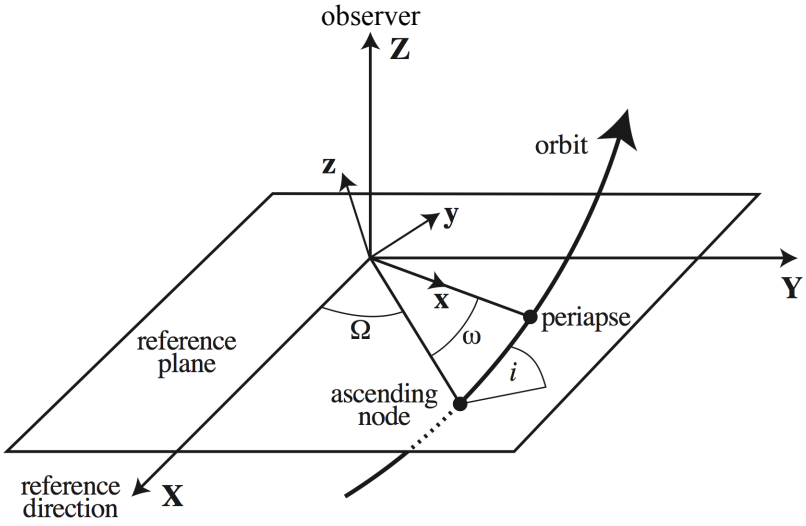

Figure 2.2 Three dimensional orbit of the planet. The origin of the coordinate system is centered on the star. In analyzing transiting systems, we conventionally choose Z-axis in the direction of our line of sight, and X- and Y-axes in the plane of the sky. Figure modified from Murray and Correia (2011).

2.1.2 Orbit in Three Dimensions

The planetary orbits we observe are in general inclined to the plane of the sky. Here we describe the planetary orbits in the three-dimensional Cartesian coordinates (X, Y, Z) centered on the star (see Figure 2.2). According to the convention in studying the transiting systems, we choose X- and Y-axes in the plane of the sky, and Z-axis in the direction of our line of sight. The three axes are chosen to form a right-handed triad. The plane spanned by X- and Y-axes are also called the *reference plane*, and it does not necessarily coincide with the planetary orbital plane. The direction of the reference line (X-axis) in the plane of the sky is arbitrary.

Clearly, we need the following three angles to specify the direction of the orbit in three dimensions. We define the *inclination*, i, as the angle between the orbital plane and the plane of the sky. The *ascending node* is the point in the reference plane at which the orbit crosses from $Z < 0$ to $Z > 0$. The angle between the reference line (X-axis) and the radius vector pointing to the ascending node is called the *longitude of ascending node*, Ω. The angle between the ascending node and the periastron of the orbit is the *argument of periastron*, ω. We can also (re-)define the *longitude of periastron* ϖ in the three dimensional orbit as

$$\varpi = \Omega + \omega. \tag{2.27}$$

Using i, Ω, and ω defined above, the position vector of the planet $\boldsymbol{r}$ in the (X, Y, Z) system is obtained by applying the series of rotations to that in the (x, y, z) system in

Table 2.1. Definitions of the Keplerian Orbital Elements and Their Related Quantities

Symbol of an Element	Definition
a	Semi-major axis
e	Eccentricity
i	Inclination
ω	Argument of periastron
Ω	Longitude of ascending node
τ	Time of periastron passage
E	Eccentric anomaly
$\varpi = \omega + \Omega$	Longitude of periastron
f	True anomaly
$\theta = f + \varpi$	True longitude
M	Mean anomaly
$\lambda = M + \varpi$	Mean longitude

Equation (2.14). Consequently, we have

$$\begin{aligned}\begin{pmatrix} X \\ Y \\ Z \end{pmatrix} &= \begin{pmatrix} \cos\Omega\cos\omega - \sin\Omega\sin\omega\cos i & -\cos\Omega\sin\omega - \sin\Omega\cos\omega\cos i & \sin\Omega\sin i \\ \sin\Omega\cos\omega + \cos\Omega\sin\omega\cos i & -\sin\Omega\sin\omega + \cos\Omega\cos\omega\cos i & -\cos\Omega\sin i \\ \sin\omega\sin i & \cos\omega\sin i & \cos i \end{pmatrix} \begin{pmatrix} r\cos f \\ r\sin f \\ 0 \end{pmatrix} \\ &= r \begin{pmatrix} \cos\Omega\cos(\omega+f) - \sin\Omega\sin(\omega+f)\cos i \\ \sin\Omega\cos(\omega+f) + \cos\Omega\sin(\omega+f)\cos i \\ \sin(\omega+f)\sin i \end{pmatrix}. \end{aligned} \tag{2.28}$$

Combining Equation (2.28) with the procedure to solve the two-dimensional motion in Section 2.1.1, we can completely specify the motion of a planet with the values of the semi-major axis a, eccentricity e, inclination i, argument of periastron ω, longitude of ascending node Ω, and time of the periastron passage τ (or, alternatively, mean anomaly M or eccentric anomaly E). This set of six components is called the *orbital elements* of the Keplerian motion, and they are summarized in Table 2.1.

2.1.3 Osculating Orbital Elements

As we will see below, the three dimensional position and velocity vectors $\boldsymbol{R} \equiv (X, Y, Z)$ and $\boldsymbol{V} \equiv (\dot{X}, \dot{Y}, \dot{Z})$ are uniquely translated into the six orbital elements $(a, e, i, \omega, \Omega, \tau)$ of the Keplerian motion. We can, therefore, define the orbital elements *at each time*, even if the motion of the planet is not Keplerian. This set of instantaneous orbital elements is called the *osculating orbital elements*. They correspond to the orbital elements of the Keplerian orbit that would be executed by the planet if all the non-Keplerian force vanished at the time.

First, note that the following quantities can be written in terms of $\boldsymbol{R}$ and $\boldsymbol{V}$:

$$\boldsymbol{h} = (\dot{Y}Z - Z\dot{Y}, Z\dot{X} - X\dot{Z}, X\dot{Y} - Y\dot{X}) \equiv (h_X, h_Y, h_Z), \tag{2.29}$$

$$\dot{R} = \pm\sqrt{V^2 - \frac{h^2}{R^2}} \quad \text{(same sign as } \boldsymbol{R}\cdot\dot{\boldsymbol{R}}\text{)}. \tag{2.30}$$

Since the rotation does not alter the vector norms, Equations (2.17) and (2.21) yield the semi-major axis as

$$a = \left(\frac{2}{R} - \frac{V^2}{GM}\right)^{-1}. \tag{2.31}$$

Then, Equation (2.12) gives the eccentricity

$$e = \sqrt{1 - \frac{h^2}{GMa}}. \tag{2.32}$$

From the definition of the inclination i and longitude of ascending node Ω, we have

$$\boldsymbol{h} = (h\sin i\sin\Omega, -h\sin i\cos\Omega, h\cos i), \tag{2.33}$$

and thus i and Ω are determined from the following relations:

$$\cos i = \frac{h_Z}{h}, \tag{2.34}$$

$$\sin\Omega = \frac{h_X}{h\sin i}, \quad \cos\Omega = -\frac{h_Y}{h\sin i}. \tag{2.35}$$

Equation (2.28) can be solved for $\omega + f$ as

$$\sin(\omega+f) = \frac{Z}{R\sin i}, \quad \cos(\omega+f) = \frac{1}{\cos\Omega}\left[\frac{X}{R} + \sin\Omega\sin(\omega+f)\cos i\right]. \tag{2.36}$$

Combining $\omega + f$ with the true anomaly f obtained from Equations (2.13) and (2.19):

$$\sin f = \frac{a(1-e^2)}{he}\dot{R}, \quad \cos f = \frac{1}{e}\left[\frac{a(1-e^2)}{R} - 1\right], \tag{2.37}$$

we obtain the argument of periastron ω. Finally, the eccentric anomaly E comes from Equations (2.22) and (2.23):

$$e\sin E = \frac{R\dot{R}}{\sqrt{GMa}}, \quad e\cos E = 1 - \frac{R}{a}. \tag{2.38}$$

This E can be translated into the time of the periastron passage τ or mean anomaly M via

$$\tau = t - \frac{M}{n} = t - \frac{E - e\sin E}{\sqrt{GM/a^3}}. \tag{2.39}$$

2.2 Planetary Transit and Occultation

2.2.1 Terminology

According to Winn (2010), we define an *eclipse* as the obscuration of a celestial body by another one. When the obscuring object is much smaller than the obscured one, this kind of eclipse is called *transit*, and the opposite case is called *occultation*. We use the word *grazing* if the obscuration is partial, *i.e.*, the path of a transiting (occulted) object is not totally inside (behind) the larger body. Note that occultations are often called *secondary eclipses* in exoplanet literatures.

2.2.2 Geometry of Eclipses

In this subsection, we discuss the transit of one planet on a Keplerian orbit. Using Equations (2.13) and (2.28), we obtain the star-planet distance projected onto the plane of the sky as

$$r_{\rm sky} \equiv \sqrt{X^2+Y^2} = \frac{a(1-e^2)}{1+e\cos f}\sqrt{1-\sin^2(\omega+f)\sin^2 i}. \tag{2.40}$$

Note that Ω does not appear in this expression (nor in other observables of transit light curves) due to the rotational symmetry of the system, as far as we consider only one planet around the star with spherically symmetric brightness distribution.

The planetary transit is centered on the minimum value of this $r_{\rm sky}$, which we define as the *transit center*. The value of f that minimizes $r_{\rm sky}$ is obtained by solving $\mathrm{d}r_{\rm sky}/\mathrm{d}f = 0$, and this equation reduces to

$$\Delta = \frac{1}{2}\arcsin\left[2e\cos(\omega+\Delta)\left(\frac{1}{\sin^2 i}-\cos^2\Delta\right) - e\sin(\omega+\Delta)\sin 2\Delta\right], \tag{2.41}$$

where we define $\Delta \equiv \pi/2-(\omega+f)$. This can be solved by iteration to give $\Delta = e\cos\omega\cot^2 i - e^2\sin 2\omega\cot^2 i(1+\cot^2 i)+\mathcal{O}(e^3)$, which is negligibly small except for planets on highly eccentric (e is large) and close-in orbits with grazing eclipses (i is far from $\pi/2$). We have, therefore, the mean anomaly at the transit center:

$$f_{\rm tra} = +\frac{\pi}{2}-\omega \tag{2.42}$$

as a very good approximation, which will be used throughout this thesis. In this approximation, the (dimensionless) *impact parameter* of the transit b, defined as the star-planet distance at the transit center divided by $R_\star$, is given by

$$b \equiv \frac{r_{\rm sky}(f=+\frac{\pi}{2}-\omega)}{R_\star} = \frac{a\cos i}{R_\star}\frac{1-e^2}{1+e\sin\omega}. \tag{2.43}$$

2.2.3 Probability of Eclipses

Suppose that we know the eccentricity e and argument of periastron ω of the planet but not the inclination i, as is often the case with radial velocity observations. In this case, the probability that the planet transits can be calculated from the impact parameter b defined above.

Transits are visible if i satisfies

$$|b| < \frac{R_\star \pm R_p}{R_\star} \quad \Leftrightarrow \quad |\cos i\,| < \frac{R_\star \pm R_p}{a}\,\frac{1+e\sin\omega}{1-e^2} \equiv \cos i_0,$$

where the "+" sign allows grazing eclipses, while the "−" sign excludes them. Thus, for a randomly placed observer, the transit probability is given by

$$p_{\rm tra} = \int_{i_0}^{\pi/2} \sin i\,{\rm d}i = \cos i_0 = \frac{R_\star \pm R_p}{a}\,\frac{1+e\sin\omega}{1-e^2}. \tag{2.44}$$

Similarly, we find the occultation probability as

$$p_{\rm occ} = \frac{R_\star \pm R_p}{a}\,\frac{1-e\sin\omega}{1-e^2}. \tag{2.45}$$

If ω is not known either, we obtain

$$p_{\rm tra} = p_{\rm occ} = \frac{R_\star \pm R_p}{a}\,\frac{1}{1-e^2} \tag{2.46}$$

by averaging Equations (2.44) and (2.45) over ω. In the limiting case that $R_p \ll R_\star$ and $e = 0$, this reduces to

$$p_{\rm tra} = p_{\rm occ} = \frac{R_\star}{a} \simeq 0.005 \left(\frac{R_\star}{R_\odot}\right)\left(\frac{a}{1\,{\rm AU}}\right)^{-1}. \tag{2.47}$$

2.3 Light-Curve Modeling and Transit Parameters

In this section, we model the variation of the stellar flux due to a planetary transit. We establish the relation between the quantities that characterize the shape of the transit and geometric information on the planetary orbits.

2.3.1 Transit Light Curve for a Planet on a Circular Orbit

Neglecting the effect of the stellar limb darkening, the shape of the extinction due to a planetary transit is well approximated by a simple trapezoid as shown in Figure 2.3. In this case, the shape of the light curve is characterized by

1. the *transit depth*: $\delta \equiv$ (relative decrease in the stellar flux),
2. the *total duration of the transit*: $T_{\rm tot} \equiv t_{\rm VI} - t_{\rm I}$,

and

3. the *duration of the full transit*: $T_{\rm full} \equiv t_{\rm III} - t_{\rm II}$,

where the durations $T_{\rm tot}$ and $T_{\rm full}$ are defined through the four contact times illustrated in Figure 2.3. We also define the durations of ingress and egress, $\tau_{\rm ing} = t_{\rm II} - t_{\rm I}$ and $\tau_{\rm egr} = t_{\rm IV} - t_{\rm III}$. When the orbit is circular, $\tau_{\rm ing}$ and $\tau_{\rm egr}$ are equal and related to the above durations as $\tau \equiv \tau_{\rm ing} = \tau_{\rm egr} = (T_{\rm tot} - T_{\rm full})/2$.

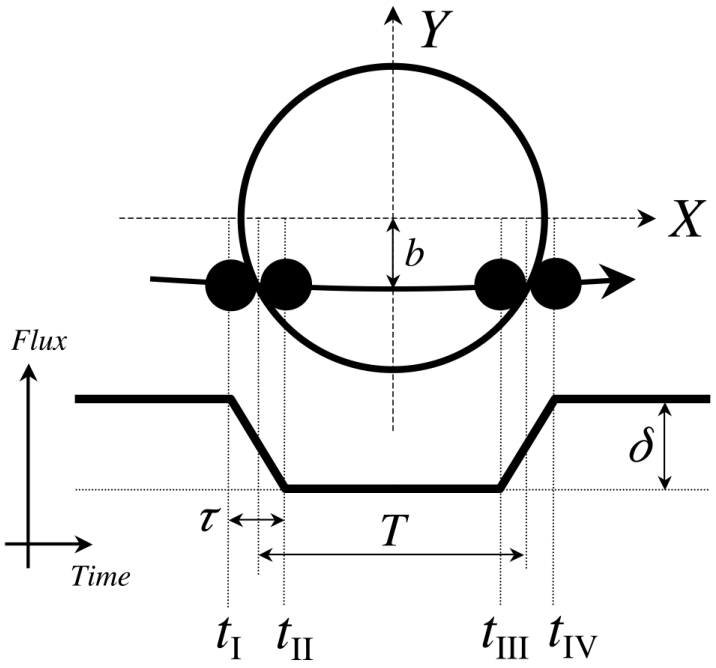

Figure 2.3 Illustration of a transit. Four contact times are defined. Figure taken from Winn (2010).

These parameters are simply related to the geometric parameters of a planet and its orbit in the following way. The transit depth δ is given as the fraction of the stellar flux blocked by the planet to the whole flux:

$$\delta = \left(\frac{R_p}{R_\star}\right)^2 . \tag{2.48}$$

The angle the planet needs to travel during a transit, divided by its angular velocity, yields the two durations as

$$T_{\rm tot} = \frac{P}{\pi} \sin^{-1}\left[\frac{R_\star}{a}\frac{\sqrt{(1+R_p/R_\star)^2 - b^2}}{\sin i}\right], \tag{2.49}$$

$$T_{\rm full} = \frac{P}{\pi} \sin^{-1}\left[\frac{R_\star}{a}\frac{\sqrt{(1-R_p/R_\star)^2 - b^2}}{\sin i}\right]. \tag{2.50}$$

In the limiting case that $R_p/R_\star \ll 1$ and $R_\star/a \ll 1$, these results are greatly simplified:

$$T \equiv \frac{T_{\rm tot} + T_{\rm full}}{2} \simeq T_{\rm tot} \simeq T_{\rm full} \simeq T_0\sqrt{1-b^2}, \tag{2.51}$$

$$\tau \simeq \frac{T_0}{\sqrt{1-b^2}}\frac{R_p}{R_\star}, \tag{2.52}$$

where T_0 is a characteristic time scale given by

$$T_0 \equiv \frac{R_\star P}{\pi a} \simeq 13\,{\rm h}\left(\frac{P}{1\,{\rm yr}}\right)^{1/3}\left(\frac{\rho_\star}{\rho_\odot}\right)^{-1/3} . \tag{2.53}$$

The above expressions for $(\delta, T_{\rm tot}, T_{\rm full})$ can be inverted to give a set of geometrical parameters

$$\frac{R_p}{R_\star} = \sqrt{\delta}, \tag{2.54}$$

$$b^2 = \frac{(1-\sqrt{\delta})^2 - (T_{\rm full}/T_{\rm tot})^2(1+\sqrt{\delta})^2}{1-(T_{\rm full}/T_{\rm tot})^2} \simeq 1 - \frac{T}{\tau}\sqrt{\delta}, \tag{2.55}$$

$$\frac{R_\star}{a} = \frac{\pi}{2\delta^{1/4}}\frac{\sqrt{T_{\rm tot}^2 - T_{\rm full}^2}}{P} \simeq \frac{\pi}{\delta^{1/4}}\frac{\sqrt{\tau T}}{P}, \tag{2.56}$$

where the last approximation holds when $\tau \ll T$. These three quantities $(R_p/R_\star, b, a/R_\star)$ (or (δ, T, τ) equivalently), along with the *time of transit center*, t_c, are called *transit parameters*, and directly related to the observables of the transit light curve. Note that the shape of transit light curves only reveals the system dimensions relative to $R_\star$.

2.3.2 Eclipse Durations for Eccentric Orbits

If the planet is on an eccentric orbit, the durations (2.49) and (2.50) are calculated via

$$t_\beta - t_\alpha = \int_{t_\alpha}^{t_\beta} {\rm d}t = \int_{f_\alpha}^{f_\beta} \left(\frac{{\rm d}f}{{\rm d}t}\right)^{-1} {\rm d}f = \frac{P(1-e^2)^{3/2}}{2\pi}\int_{f_\alpha}^{f_\beta} \frac{1}{(1+e\cos f)^2}\,{\rm d}f, \tag{2.57}$$

where $\alpha, \beta = {\rm I}, {\rm II}, {\rm III}, {\rm IV}$. Here we use $r^2\dot{f} = h = na^2\sqrt{1-e^2}$ and Equation (2.13) in the last equality, and f_α is the solution of

$$r_{\rm sky}(f_\alpha) = \frac{a(1-e^2)}{1+e\cos f_\alpha}\sqrt{1-\sin^2(\omega+f_\alpha)\sin^2 i} = R_\star \pm R_p, \tag{2.58}$$

where $+$ and $-$ signs correspond to $\alpha = {\rm I}, {\rm IV}$ and $\alpha = {\rm II}, {\rm III}$, respectively. Equation (2.58) cannot be solved analytically for f_α, but the solution to the leading orders of e and $R_\star/a$ can be obtained as

$$\frac{\pi}{2} - (\omega + f_\alpha) = \frac{1}{\sin i}\frac{R_\star}{a}\frac{1+e\sin\omega}{1-e^2}\sqrt{\left(1 \pm \frac{R_p}{R_\star}\right)^2 - b^2} \tag{2.59}$$

for $\alpha = {\rm I}, {\rm II}$. As the first approximation, therefore, $T_{\rm tot}$ and $T_{\rm full}$ for the eccentric case are

$$\begin{aligned} T_{\rm tot} &= \frac{P(1-e^2)^{3/2}}{2\pi}\cdot 2\left[\frac{\pi}{2} - (\omega + f_{\rm I})\right]\frac{1}{(1+e\sin\omega)^2} \\ &= \frac{P}{\pi}\frac{R_\star}{a}\frac{\sqrt{(1+R_p/R_\star)^2 - b^2}}{\sin i}\left(\frac{\sqrt{1-e^2}}{1+e\sin\omega}\right), \end{aligned} \tag{2.60}$$

$$T_{\rm full} = \frac{P}{\pi}\frac{R_\star}{a}\frac{\sqrt{(1-R_p/R_\star)^2 - b^2}}{\sin i}\left(\frac{\sqrt{1-e^2}}{1+e\sin\omega}\right), \tag{2.61}$$

which are just different from the circular case by the factor in the parenthesis, corresponding to the difference of orbital velocity around the transit.

For an eccentric orbit, $\tau_{\rm ing}$ and $\tau_{\rm egr}$ are generally unequal, but the difference is slight. Indeed, to the leading orders of $R_\star/a$ and e, we have

$$\frac{\tau_{\rm egr}-\tau_{\rm ing}}{\tau_{\rm egr}+\tau_{\rm ing}} \sim e\cos\omega \left(\frac{R_\star}{a}\right)^3 (1-b^2)^{3/2} \tag{2.62}$$

(Winn 2010). This quantity is less than $10^{-2}e$ for a close-in planet with $R_\star/a = 0.2$, and even smaller for more distant planets.

2.3.3 Analytic Formulae for Achievable Precisions of Transit Parameters

We usually determine the transit parameters by fitting the observed data using numerical methods like Markov chain Monte Carlo (MCMC) algorithm (see Section 4.2). However, it is useful to have simple analytic expressions for the achievable precisions of transit parameters, because they can be easily used to plan observations and/or estimate the detectability of such effects as the variations in transit parameters (including, of course, transit timing variations discussed in Chapter 3).

Carter et al. (2008) derived such formulae under the assumptions that the data have uniform time sampling Δt and independent Gaussian errors σ in the relative flux. In this case, a Fisher information analysis gives the uncertainties in the transit parameters (δ, t_c, T, τ) as

$$\sigma_\delta \simeq Q^{-1}\delta, \tag{2.63}$$

$$\sigma_{t_c} \simeq Q^{-1}T\sqrt{\tau/2T}, \tag{2.64}$$

$$\sigma_T \simeq Q^{-1}T\sqrt{2\tau/T}, \tag{2.65}$$

$$\sigma_\tau \simeq Q^{-1}T\sqrt{6\tau/T}, \tag{2.66}$$

where $Q \equiv \sqrt{N}\delta/\sigma$ and N is the number of data points obtained during the transit. These estimates are valid for $\delta \ll 1$, weak limb darkening, and the precisely known out-of-transit flux. Note that these formulae underestimate the errors in the presence of the correlated noises and strong limb darkening.

2.4 Physical Properties of Exoplanets Obtained from Transit Observations

2.4.1 Determining Absolute Dimensions

As we saw in Section 2.3, transit observations reveal only the geometry of the system relative to the stellar radius $R_\star$. Similarly, the radial velocity information gives some combination of the planetary mass M_p and stellar mass $M_\star$ but not M_p itself, because the semi-amplitude of the stellar radial velocity $K_\star$ is given by

$$K_\star = \frac{M_p}{M_\star+M_p}\frac{na\sin i}{\sqrt{1-e^2}} = \frac{GM_p}{na^2}\frac{\sin i}{\sqrt{1-e^2}} = \left(\frac{2\pi G}{P}\right)^{1/3}\frac{M_p}{(M_\star+M_p)^{2/3}}\frac{\sin i}{\sqrt{1-e^2}}. \tag{2.67}$$

In order to fix the absolute dimensions of the system, therefore, we need to know the values of $R_\star$ or $M_\star$, which are usually obtained by spectroscopic observations of the central star. For this reason, we should always keep in mind that the absolute dimensions of the planetary system are subject to the uncertainties in the stellar parameters.

That said, there is still one dimensional quantity that can be determined from transit observations alone: mean density of the central star $\rho_\star$. It is related to the time scale of the planetary orbit (*e.g.*, orbital period and transit duration), which is the only dimensional quantity constrained from transit light curves. Dividing Kepler's third law by $4\pi G R_\star^3/3$, we obtain

$$\rho_\star + \left(\frac{R_p}{R_\star}\right)^3 \rho_p = \frac{3\pi}{GP^2}\left(\frac{a}{R_\star}\right)^3 \tag{2.68}$$

(Seager and Mallén-Ornelas 2003). Since we know the value of $a/R_\star$ from the transit light curve and $(R_p/R_\star)^3$ is usually very small, we can constrain $\rho_\star$ purely from the photometric observation. This is a natural result because the orbital period P is roughly given by the free-fall time $1/\sqrt{G\overline{\rho}}$, where $\overline{\rho}$ is the mean density inside the planetary orbit. Since $\overline{\rho}$ is obtained by diluting $\rho_\star$ by the factor of $(a/R_\star)^3$, and the value of $a/R_\star$ characterizes the ratio of the orbital period P to the transit duration T, we can determine $\rho_\star$ from P and T.

In addition, if we have $K_\star$ given by Equation (2.67), the planetary surface gravity g_p can be derived as

$$g_p \equiv \frac{GM_p}{R_p^2} = \frac{1}{R_p^2}\frac{K_\star n a^2\sqrt{1-e^2}}{\sin i} = \frac{2\pi}{P}\frac{K_\star\sqrt{1-e^2}}{(R_p/a)^2\sin i}, \tag{2.69}$$

independently of the stellar parameters (Southworth et al. 2007).

2.4.2 Transmission Spectroscopy

In reality, the planetary radius constrained from the transit depth is effectively "enhanced" due to the absorption by the upper *atmosphere* of the planet. Since this absorption depends on the wavelength, we can gain the knowledge of the atmospheric composition by measuring the transmission spectrum.

Calculation of the expected signal is rather complicated (*e.g.*, Bétrémieux and Kaltenegger 2013): we need to solve radiative transfer equations of the incident light in the model atmosphere, whose architecture depends on various parameters including its chemical composition and surface gravity. However, an order-of-magnitude estimate for the radius enhancement due to absorption is simply given by introducing the *atmospheric scale height*:

$$H = \frac{k_B T_p}{\mu_m g_p}, \tag{2.70}$$

where k_B is the Boltzmann constant, T_p is the temperature, μ_m is the mean molecular mass, and g_p is the surface gravity. Using this H, and defining R_p as the radius of the disk which is optically thick at all wavelengths, the increase in the transit depth due to absorption can be estimated as

$$\Delta\delta = \frac{(R_p + N_H H)^2}{R_\star^2} - \frac{R_p^2}{R_\star^2} \simeq 2N_H\delta\left(\frac{H}{R_p}\right)^2, \tag{2.71}$$

where N_H is a fudge factor of order unity. This result shows that the effect of absorption is readily detectable at low g_p, low μ_m, and high T_p, all of which lead to a larger scale height.

Among the parameters in Equation (2.70), g_p and T_p can be estimated from usual transit or radial velocity observations combined with the stellar spectroscopy (*c.f.*, Equations (2.69) and (2.73)). Thus the atmospheric composition is mainly constrained by comparing this kind of model with the wavelength-dependent transit depth $\delta(\lambda)$ obtained from observations at multiple wavelengths. Such observations have actually been successful in detecting molecules in planetary atmospheres, but the solution that explains the observed $\delta(\lambda)$ is often degenerate at the current precision.

2.4.3 Occultation Spectroscopy

Since the occultation depth $\delta_{\rm occ}$ is determined by the ratio of the flux from the planet to that from the star, we have

$$\delta_{\rm occ} = \left(\frac{R_p}{R_\star}\right)^2 \frac{I_p}{I_\star} = \delta \, \frac{I_p}{I_\star}, \tag{2.72}$$

where I_p and $I_\star$ are mean intensities of the planetary and stellar disks. With the knowledge of the transit depth, therefore, we can constrain I_p, that consists of thermal radiation and reflected starlight. In most cases, these two components emerge in different wavelength regions because of the difference between stellar and planetary temperatures, making it possible to observe them separately. In contrast to the transmission spectroscopy, where we observe the starlight that grazes the planetary limb, occultation spectroscopy focuses on the emission averaged over the planetary disk. Thus these two methods give different and complementary information about the planetary atmospheres.

First, suppose that I_p is constant and that the observing wavelength is long enough for the thermal emission to dominate. In this case, approximating the planet and the star as blackbody radiators, we obtain

$$\delta_{\rm occ}(\lambda) = \left(\frac{R_p}{R_\star}\right)^2 \frac{B_\lambda(T_p)}{B_\lambda(T_\star)} \xrightarrow{\lambda \gg hc/k_B T_p} \left(\frac{R_p}{R_\star}\right)^2 \frac{T_p}{T_\star} \tag{2.73}$$

where $B_\lambda(T)$ is the Planck function given by

$$B_\lambda(T) \equiv \frac{2hc^2}{\lambda^5} \frac{1}{{\rm e}^{hc/\lambda k_B T} - 1} \xrightarrow{\lambda \gg hc/k_B T_p} \frac{2ck_B T}{\lambda^4}.$$

Here, the observed $\delta_{\rm occ}$ is given by integrating $\delta_{\rm occ}(\lambda)$ over the bandpass. Even when the spectrum is not described by Planck's formula, we can define a brightness temperature $T_b(\lambda)$ as the equivalent blackbody temperature. This is sometimes useful in describing wavelength-dependent intensity, which is not necessarily of thermal origin.

On the other hand, observations at shorter wavelengths (or the subtraction of thermal emission) give the reflectance spectrum of the planet's day side. The occultation depth due to this light is

$$\delta_{\rm occ}(\lambda) = A_\lambda \left(\frac{R_p}{a}\right)^2,$$

where A_λ is the geometric albedo, defined by

$$A_\lambda = \frac{\text{flux reflected by the planet at full phase}}{\text{flux that would be reflected by a Lambertian disk with the same cross section}}.$$

Since clouds can produce very large albedo variations, reflectance spectroscopy may help to understand the roles of clouds. This knowledge is particularly useful in interpreting the atmospheric spectrum because the existence, prevalence, and composition of the cloud cause great uncertainties in the atmospheric modeling.

2.4.4 The Rossiter-McLaughlin Effect

Due to the stellar rotation, one half of the stellar disk is blueshifted, while the other is redshifted. Such spatial variation of the velocity field on the stellar surface causes the time-dependent distortion of the stellar spectrum during a planetary transit, leading to an anomaly in the radial velocity of the star. In short, when the planet hides the approaching (bludshifted) side of the star, it appears to move away (redshifted) from the observer, and the opposite happens when the planet hides the receding side. This effect is known as the *Rossiter-McLaughlin (RM) effect*, which was originally proposed for an eclipsing binary (Rossiter 1924; McLaughlin 1924). It is especially important that the sky-projected *spin-orbit angle* (the angle between the stellar spin axis and planetary orbital axis), usually denoted by λ, can be measured from the pattern of the apparent motion, because this angle is intimately related to the orbital evolution history the planet has experienced.

The maximum amplitude of the resulting anomalous radial velocity is roughly given by

$$\Delta V_{\rm RM} \approx \delta\sqrt{1-b^2}\,(v_\star \sin i_\star), \tag{2.74}$$

where $v_\star \sin i_\star$ is the line-of-sight component of the equatorial rotational velocity of the star (Ohta et al. 2005). Since the value of $v_\star$ is typically larger ($\gtrsim$ km s) than the modulation of the stellar *orbital* velocity, the detection of the RM effect is fairly feasible for giant planets with $\delta \sim 0.01$. It is also important to note that, more generally, the RM effect provides a way to scan the velocity structure on the stellar disk, such as the differential rotation (Hirano et al. 2011a).

Chapter 3

Transit Timing Variations: Formulation and Observation

3.1 Overview

Although the analysis of transit light curves provides a wealth of information on the geometry of the planetary systems, the shape of the transit itself never tells us the mass of the transiting object. In order to confirm its planetary nature, therefore, the spectroscopic observations of the host star to measure its radial velocities and to determine the dynamical mass of the planet is essential. Unfortunately, however, it is often difficult or even practically impossible to apply the spectroscopy to the majority of transiting planet candidates discovered by the *Kepler* space telescope, because their host stars are very distant and dim, with their apparent magnitudes $V > 15$. Furthermore, in multiple-planetary systems, the radial velocity solutions are often degenerate in the limited time sampling (e.g., Rodigas and Hinz 2009; Anglada-Escudé et al. 2010; Wittenmyer et al. 2013), partly because we never know actually how many planets are in the system, including both transiting and non-transiting ones. For these reasons, we need another method that is capable of determining the mass of transiting objects based on the photometric data alone and, if possible, sensitive to the architecture of the planetary system.

An analysis of the *transit timing variations* (TTVs) provides the most ideal way known for such requirements. In the case of the two-body problem, the planetary orbit is perfectly periodic, and so are the transits. On the other hand, in the presence of non-Keplerian effects including the perturbations from other planets, transit times of the planet deviate from the strict periodicity. By analyzing these deviations (TTVs), we can constrain the planetary parameters, especially the planetary mass. The TTV method was originally proposed as a way of detecting the non-Keplerian effects (Miralda-Escudé 2002) or Earth-mass planets (Agol et al. 2005; Holman and Murray 2005). Then, this method was first applied to a real planetary system by Holman et al. (2010), who determined the masses of the two transiting planets in the Kepler-9 system (Kepler-9b, c) using their TTVs. After that, the TTV method has significantly contributed to the confirmations of *Kepler* multi-transiting systems including the Kepler-11 system (Lissauer et al. 2011), where the masses of the six transiting planets (only upper limit for one of them) were solely determined without radial velocity measurements. The TTV method has also succeeded in finding and characterizing a non-transiting planet from the perturbation it gives to other transiting planets (Nesvorný et al. 2012, 2013). Recently, Lithwick et al. (2012) derived simple

analytic TTV formulae for a planet pair in near a $j : j-1$ resonance (pair of planets ratio of whose periods is close to $j : j-1$, where j is an integer), which clarified the physical picture of the TTV phenomenon and contributed to the wholesale confirmations of the *Kepler* multiples (Xie 2013a,b). Since the TTV method has sensitivities to the small-mass planets down to Earth-sized ones, it is also expected to play a key role in Earth-sized transiting planet surveys such as TESS.

In this chapter, we review approximate analytic treatments of the TTVs, especially focusing on the formulation by Lithwick et al. (2012), because it provides physical insight into this phenomenon. We also make the list of *Kepler* planets confirmed using TTVs as the targets of future detailed characterization and the source of statistical arguments.

3.2 Analytic Formulation of TTVs

Since the N-body problem with $N \geq 3$ has no general analytic solution, it is impossible to obtain closed analytic formulae for TTV signals. Nevertheless, approximate analytic formulations for various specific situations have been discussed by several authors (*e.g.*, Miralda-Escudé 2002; Holman and Murray 2005; Agol et al. 2005; Nesvorný and Morbidelli 2008; Nesvorný 2009; Lithwick et al. 2012), on the basis of the techniques in celestial mechanics.

In this subsection, we have a glimpse of such formulations, mainly focusing on the work by Lithwick et al. (2012); their formulae are handy for practical use, applicable for the situations where the TTV signals become the most prominent, generalize some of the previous results, and above all physically very enlightening. In order to better understand their derivation, we briefly summarize the epicyclic approximation in Section 3.2.1, and then discuss the main topic in Section 3.2.2. We also consider the secular effects on the transit timings in Section 3.2.3, which might be detectable in the long-term data of *Kepler*.

3.2.1 Epicyclic Motion

Here we adopt the cylindrical coordinates (ξ, ϕ, z), and consider the motion of a particle in an axisymmetric potential $V(\xi, z)$. We also assume that $V(\xi, z)$ is symmetric about $z = 0$ plane and smooth at $z = 0$. In this case, the equations of motion of the particle are given by

$$\ddot{\xi} - \xi\dot{\phi}^2 = -\frac{\partial V(\xi, z)}{\partial \xi}, \tag{3.1}$$

$$\frac{d}{dt}(\xi^2\dot{\phi}) = 0, \tag{3.2}$$

$$\ddot{z} = -\frac{\partial V(\xi, z)}{\partial z}. \tag{3.3}$$

Equation (3.2) corresponds to the conservation of the z-component of the specific angular momentum:

$$h \equiv \xi^2\dot{\phi} = \text{const.} \tag{3.4}$$

This allows us to rewrite Equations (3.1) and (3.3) as

$$\ddot{\xi} = \frac{h^2}{\xi^3} - \frac{\partial V(\xi, z)}{\partial \xi} = -\frac{\partial V_{\text{eff}}(\xi, z)}{\partial \xi}, \quad \ddot{z} = -\frac{\partial V_{\text{eff}}(\xi, z)}{\partial z}, \tag{3.5}$$

where we define the effective potential:

$$V_{\rm eff}(\xi, z) \equiv V(\xi, z) + \frac{h^2}{2\xi^2}. \tag{3.6}$$

The minimum of this effective potential occurs at $(\xi, z) = (\xi_{\rm g}, 0)$, where $\xi_{\rm g}$ satisfies

$$0 = \left(\frac{\partial V_{\rm eff}(\xi, z)}{\partial \xi}\right)_{\xi=\xi_{\rm g}} \quad \Leftrightarrow \quad \left(\frac{\partial V(\xi, z)}{\partial \xi}\right)_{\xi=\xi_{\rm g}} = \frac{h^2}{\xi_{\rm g}^3} = \xi_{\rm g}^2 \dot{\phi}. \tag{3.7}$$

This $\xi_{\rm g}$, sometimes called the *guiding center radius*, corresponds to the radius of the circular orbit in $z = 0$ plane.

Let us then "solve" the equations of motion (3.5) by expanding ξ and z around $(\xi_{\rm g}, 0)$. Introducing $x \equiv \xi - \xi_{\rm g}$, the effective potential (3.6) is expanded as

$$V_{\rm eff}(x, z) = V_{\rm eff}(\xi_{\rm g}, 0) + \frac{1}{2}\left(\frac{\partial^2 V_{\rm eff}(\xi, z)}{\partial x^2}\right)_{(\xi_{\rm g},0)} x^2 + \frac{1}{2}\left(\frac{\partial^2 V_{\rm eff}(\xi, z)}{\partial z^2}\right)_{(\xi_{\rm g},0)} z^2 + \mathcal{O}(xz^2). \tag{3.8}$$

If we keep only the x^2 and z^2 terms (*epicyclic approximation*), the equations of motion (3.5) can be approximated as

$$\ddot{x} = -\kappa^2 x, \tag{3.9}$$

$$\ddot{z} = -\nu^2 z, \tag{3.10}$$

where

$$\kappa^2 \equiv \left(\frac{\partial^2 V_{\rm eff}(\xi, z)}{\partial x^2}\right)_{(\xi_{\rm g},0)}, \quad \nu^2 \equiv \left(\frac{\partial^2 V_{\rm eff}(\xi, z)}{\partial z^2}\right)_{(\xi_{\rm g},0)}. \tag{3.11}$$

These two frequencies κ and ν are called *epicyclic frequency* and *vertical frequency*, respectively. Using Equation (3.7), κ can also be written as

$$\begin{aligned}\kappa^2 &= \left(\frac{\partial^2 V(\xi, z)}{\partial x^2}\right)_{(\xi_{\rm g},0)} + \frac{3h^2}{\xi_{\rm g}^4} = \left(\frac{\partial^2 V(\xi, z)}{\partial x^2}\right)_{(\xi_{\rm g},0)} + 3\left(\frac{\partial V(\xi, z)}{\partial x}\right)_{(\xi_{\rm g},0)} \\ &= \left(\xi\frac{d\Omega^2}{d\xi} + 4\Omega^2\right)_{\xi=\xi_{\rm g}} = \left(\frac{1}{\xi^3}\frac{d(\xi^4\Omega^2)}{d\xi}\right)_{\xi=\xi_{\rm g}},\end{aligned} \tag{3.12}$$

where

$$\Omega^2(\xi) \equiv \left(\frac{1}{\xi}\frac{\partial V(\xi, z)}{\partial \xi}\right)_{z=0} \tag{3.13}$$

is the circular frequency. Since the steepness of $V(\xi, 0)$ is usually between the two extrema, the potential due to a point mass ($\sim 1/\xi$) and that formed by uniform mass distribution ($\sim \xi^2$), $\Omega^2(\xi)$ is between ξ^{-3} and ξ^0. Thus, we have

$$\Omega(\xi_{\rm g}) \lesssim \kappa \lesssim 2\Omega(\xi_{\rm g}). \tag{3.14}$$

Equations (3.9) and (3.10) can be immediately solved to give

$$x(t) = \xi - \xi_{\rm g} = -X\cos(\kappa t + \alpha), \tag{3.15}$$

$$z(t) = Z\cos(\nu t + \beta), \tag{3.16}$$

where X, Z, α, and β are constants. The solution for ϕ is obtained from Equation (3.4), which reduces to

$$\dot{\phi} = \frac{h}{\xi_{\rm g}^2}\left(1+\frac{x}{\xi_{\rm g}}\right)^{-2} \simeq \Omega(\xi_{\rm g})\left[1+\frac{2X}{\xi_{\rm g}}\cos(\kappa t+\alpha)\right] \tag{3.17}$$

to the first order of x. Integrating this equation, $\phi(t)$ is obtained as

$$\phi(t) = \Omega(\xi_{\rm g})t + \phi_0 + \frac{2\Omega(\xi_{\rm g})}{\kappa}\frac{X}{\xi_{\rm g}}\sin(\kappa t+\alpha), \tag{3.18}$$

where ϕ_0 is a constant. Defining y-axis in the direction of increasing ϕ, the motion in the Cartesian frame centered at the *guiding center* $(\xi,\phi,z) = (\xi_{\rm g}, \Omega(\xi_{\rm g})t+\phi_0, 0)$ is obtained from Equations (3.15), (3.16), and (3.18) as

$$x(t) = -X\cos(\kappa t+\alpha), \tag{3.19}$$

$$y(t) = \frac{2\Omega(\xi_{\rm g})}{\kappa}X\sin(\kappa t+\alpha) \equiv Y\sin(\kappa t+\alpha), \tag{3.20}$$

$$z(t) = Z\cos(\nu t+\beta). \tag{3.21}$$

In this way, the orbit in an axisymmetric potential is decomposed into the circular part (*i.e.*, motion of the guiding center) and the motion described by Equations (3.19) to (3.21).

Correspondence to the Keplerian Motion

In the Keplerian motion, we have $\Omega^2 \propto 1/\xi^3$, and so Equation (3.12) gives

$$\kappa = \Omega(\xi_{\rm g}). \tag{3.22}$$

In this case, the horizontal motion around the guiding center becomes an ellipse whose axis ratio is given by $X/Y = \kappa/2\Omega(\xi_{\rm g}) = 1/2$ from Equation (3.20). In addition, $\xi_{\rm g}$, $X/\xi_{\rm g}$, $Z/\xi_{\rm g}$, $\Omega(\xi_{\rm g})$, and $\kappa t+\alpha$ correspond to the semi-major axis a, orbital eccentricity e, orbital inclination i, mean motion n, and true anomaly $f = \theta - \varpi$. While these are clear from the fact that $X/\xi_{\rm g}$ and $Z/\xi_{\rm g}$ give the fractional amplitudes of the radial and vertical oscillations, they can also be checked by substituting the position and velocity obtained from Equations (3.19) to (3.21) into the expressions for osculating orbital elements in Equations (2.31) to (2.39).

Implication for Transit Timing Variations

When $\kappa = \Omega(\xi_{\rm g})$, Equation (3.18) implies

$$\phi(t) = 0 \ (\mathrm{mod}\ 2\pi) \quad \Leftrightarrow \quad t = m\left(\frac{2\pi}{\Omega_{\rm g}}\right) + \mathrm{const}, \tag{3.23}$$

where m is an integer. This means that the orbital period of the Keplerian orbit P is given by $P = 2\pi/\Omega(\xi_{\rm g}) = 2\pi/n$. In contrast, transit times deviate from the strict periodicity if n or e vary over time; such variations are usually caused by resonant terms (Section 3.2.2). Smaller effects also result from the difference between κ and n, because the sine function in Equation (3.18) has a period slightly different from P. This is equivalent to the orbital precession with the frequency $\dot{\varpi} = n-\kappa$, and the corresponding timing variation usually occurs on secular time scales (see Section 3.2.3).

3.2.2 TTV Signals for a Pair of Coplanar Planets near a First-order Mean Motion Resonance

In this subsection, we derive the analytic TTV formulae for a pair of coplanar planets in near a $j : j-1$ mean-motion resonance, following the appendix of Lithwick et al. (2012). We evaluate each of the variations of nt and e (*c.f.*, Equation (3.18)) due to the resonant terms on the basis of the Hamiltonian formulation. The secular effect is neglected because it becomes important only on a much longer time scale than that of the resonant effect considered here. We assume coplanarity throughout this subsection, and so the orbital inclination i and the longitude of the ascending node Ω do not appear in the following formulation explicitly.

Goal of This Formulation

As discussed in Section 3.2.1, the angular position of the planet on a low-eccentricity orbit is written as

$$\theta = \lambda + 2e\sin(\lambda - \varpi), \tag{3.24}$$

to the first order of e. This equation corresponds to Equation (3.18), but here we adopt the orbital elements defined in Section 2.1.2 (see Table 2.1) to describe the same equation. First, $\theta \equiv f + \varpi = f + \omega + \Omega$ is the *true longitude* of the planet, which is the *true* angular position of the planet measured from the reference line *fixed in an inertial frame*; this θ corresponds to $\phi(t)$ in Equation (3.18). Similarly, the *mean longitude* $\lambda \equiv M + \varpi = n(t-\tau)+\omega+\Omega$ gives the *mean* angular position of the planet from the same reference line, and corresponds to $\Omega(\xi_{\rm g})t + \phi_0$. As noted above, $\kappa t + \alpha$ in Equation (3.18) corresponds to the true anomaly $f = \theta - \varpi$, but here we neglect the $\mathcal{O}(e)$ difference between θ and λ because we drop $\mathcal{O}(e^2)$ terms in Equation (3.24).

Applying the same discussion in the last part of Section 3.2.1 to Equation (3.24), the deviation of transit times (*i.e.*, the solutions of $\theta(t) = \text{const.}(\text{mod } 2\pi)$) from the strict periodicity is obtained by evaluating

1. Deviation of $\lambda(t)$ from the linear function of t,

2. Variations of e and ϖ.

In what follows, we described the derivation of these two quantities.

Hamiltonian and Disturbing Function

The Hamiltonian of the system is given by

$$\mathcal{H} = -\frac{GM_\star m}{2a} - \frac{GM_\star m'}{2a'} - \frac{Gmm'}{|\boldsymbol{r} - \boldsymbol{r}'|}, \tag{3.25}$$

where G is Newton's gravitational constant and $M_\star$ is the mass of the central star. We denote the mass, semi-major axis, and position vector of the inner planet by m, a, and $\boldsymbol{r}$, respectively, and those symbols with primes indicate those of the outer planet.

Assuming that their orbits never cross (*i.e.*, $r' > r$ for any time), the third term can be expanded as

$$\frac{Gmm'}{|\boldsymbol{r}-\boldsymbol{r}'|} = \frac{Gmm'}{r'}\sum_{l=0}^{\infty}\left(\frac{r}{r'}\right)^l P_l(\cos\psi) = \frac{Gmm'}{a'}\sum_{l=0}^{\infty}\alpha^l\left(\frac{a'}{r'}\right)^{l+1}\left(\frac{r}{a}\right)^l P_l(\cos\psi), \quad (3.26)$$

where P_l is the Legendre polynomial, ψ is the angle between $\boldsymbol{r}$ and $\boldsymbol{r}'$, and we define

$$\alpha = \frac{a}{a'} < 1. \quad (3.27)$$

In general, the summation in Equation (3.26) can be written in the form of

$$\mathcal{R}^j = \sum S(a, a', e, e', i, i')\cos\varphi, \quad (3.28)$$

which is called the *disturbing function* (Murray and Dermott 1999, §6). Here, the phase φ is given in terms of ϖ, Ω, and λ as

$$\varphi = j_1\lambda' + j_2\lambda + j_3\varpi' + j_4\varpi + j_5\Omega' + j_6\Omega, \quad (3.29)$$

where the integers j_i $(i = 1, 2, \cdots, 6)$ satisfies

$$\sum_{i=1}^{6} j_i = 0. \quad (3.30)$$

Since λ and λ' have angular frequencies $n = 2\pi/P$ and $n' = 2\pi/P'$, respectively, $\cos\varphi$ averaged over the time longer than the orbital periods of the planets is small. Near a $j : j-1$ resonance, however, the terms that include the combination of

$$\lambda^j \equiv j\lambda' - (j-1)\lambda \quad (3.31)$$

vary slowly, and contribute to the time-averaged motion of the system (averaging principle). In this case, the disturbing function that describes the time-averaged motion reduces to

$$\mathcal{R}^j = fe\cos(\lambda^j - \varpi) + ge'\cos(\lambda^j - \varpi'), \quad (3.32)$$

where we set $\Omega = \Omega' = 0$. The coefficients f and g are the functions of j and α, and summarized in Table 3 of Lithwick et al. (2012).

Canonical Poincaré Variables

For describing this system, we choose the canonical Poincaré variables defined as

$$\lambda = M + \varpi, \qquad \Lambda = m\sqrt{GM_\star a}, \quad (3.33)$$

$$\gamma = -\varpi, \qquad \Gamma = m\sqrt{GM_\star a}(1 - \sqrt{1-e^2}), \quad (3.34)$$

$$\zeta = -\Omega, \qquad Z = m\sqrt{GM_\star a(1-e^2)}(1-\cos i), \quad (3.35)$$

and similarly for the outer planet. As their names suggest, (λ, γ, ζ) and (Λ, Γ, Z) are the conjugate sets of canonical coordinates and momenta (*e.g.*, Goldstein et al. 2002). Using these variables, the Hamiltonian (3.25) is written as

$$\mathcal{H} = -\frac{G^2M_\star^2m^3}{2\Lambda^2} - \frac{G^2M_\star^2m'^3}{2\Lambda'^2} - \frac{G^2M_\star mm'^3}{\Lambda'^2}\mathcal{R}^j. \quad (3.36)$$

Constants of Motion

As can be clearly seen from Equations (3.25) and (3.32), $\zeta = -\Omega$ and $\zeta' = -\Omega'$ are the cyclic coordinates of the Hamiltonian $\mathcal{H}$, and so Z and Z' are the constants of motion of this system. We can also find other two constants of motion by choosing

$$\theta_1 = j\lambda' + (1-j)\lambda + \gamma = \lambda^j - \varpi, \tag{3.37}$$
$$\theta_2 = j\lambda' + (1-j)\lambda + \gamma' = \lambda^j - \varpi', \tag{3.38}$$
$$\theta_3 = \lambda, \tag{3.39}$$
$$\theta_4 = \lambda' \tag{3.40}$$

as the other four canonical coordinates. Then, the canonical momenta Θ_i $(i = 1, 2, 3, 4)$ conjugate to θ_i are obtained from the condition for the canonical transformation:

$$\sum_{i=1}^{4} \Theta_i \mathrm{d}\theta_i = \Lambda \mathrm{d}\lambda + \Gamma \mathrm{d}\gamma + \Lambda' \mathrm{d}\lambda' + \Gamma' \mathrm{d}\gamma'. \tag{3.41}$$

The resulting relations are

$$(1-j)(\Theta_1 + \Theta_2) + \Theta_3 = \Lambda, \tag{3.42}$$
$$j(\Theta_1 + \Theta_2) + \Theta_4 = \Lambda', \tag{3.43}$$
$$\Theta_1 = \Gamma, \tag{3.44}$$
$$\Theta_2 = \Gamma'. \tag{3.45}$$

As a function of this new set of canonical variables, $(\theta_1, \theta_2, \theta_3, \theta_4, \zeta, \zeta'; \Theta_1, \Theta_2, \Theta_3, \Theta_4, Z, Z')$, the Hamiltonian (3.25) does not include θ_3 and θ_4 explicitly. Therefore, we have other two constants of motion, $K = \Theta_3$ and $K' = \Theta_4$:

$$\begin{aligned} K &= \Lambda + (j-1)(\Gamma + \Gamma') \\ &= m\sqrt{GM_\star a} + (j-1)\sqrt{GM_\star}[m\sqrt{a}(1-\sqrt{1-e^2}) + m'\sqrt{a'}(1-\sqrt{1-e'^2})], \end{aligned} \tag{3.46}$$
$$\begin{aligned} K' &= \Lambda' - j(\Gamma + \Gamma') \\ &= m'\sqrt{GM_\star a'} - j\sqrt{GM_\star}[m\sqrt{a}(1-\sqrt{1-e^2}) + m'\sqrt{a'}(1-\sqrt{1-e'^2})]. \end{aligned} \tag{3.47}$$

Variation of the Mean Longitude λ

Now, let us first evaluate the variation of the mean longitude λ associated with the variation of the semi-major axis. Hereafter, we will use the set of variables defined in Equations (3.33), (3.34), and (3.35). The Hamiltonian (3.25) gives the equation of motion for λ as

$$\frac{\mathrm{d}\lambda}{\mathrm{d}t} = \frac{\partial \mathcal{H}}{\partial \Lambda} = \frac{G^2 M_\star^2 m^3}{\Lambda^3} - \frac{G^2 M_\star m m'^3}{\Lambda'^2} \frac{\partial \mathcal{R}^j}{\partial \Lambda} \simeq \sqrt{\frac{GM_*}{a^3}}. \tag{3.48}$$

In the last equality, we neglect the term arising from the derivative of the disturbing function $\mathcal{R}^j$, which will be justified later. We then define a *time-independent* part of the semi-major axis, a_0, using Equation (3.46) as

$$a_0 \equiv \left(\frac{K}{m\sqrt{GM_\star}} \right)^2, \tag{3.49}$$

and similarly for a_0'. These a_0 and a_0' correspond to the semi-major axes when $e = e' = 0$. Also defining *time-dependent* $\delta a \equiv a - a_0 \ll a_0$, Equation (3.48) reduces to

$$\frac{\mathrm{d}\lambda}{\mathrm{d}t} \simeq \sqrt{\frac{GM_\star}{a_0^3}}\left(1 - \frac{3}{2}\frac{\delta a}{a_0}\right) = \frac{2\pi}{P} - \frac{3}{2}\frac{2\pi}{P}\frac{\delta a}{a_0}, \tag{3.50}$$

where we *define*

$$P \equiv 2\pi\sqrt{\frac{a_0^3}{GM_\star}}, \quad P' \equiv 2\pi\sqrt{\frac{a_0'^3}{GM_\star}}. \tag{3.51}$$

Equation (3.50) can be integrated to give

$$\begin{pmatrix}\lambda\\ \lambda'\end{pmatrix} = \begin{pmatrix}\frac{2\pi}{P}(t-T)\\ \frac{2\pi}{P'}(t-T')\end{pmatrix} - \frac{3}{2}\int \mathrm{d}t \begin{pmatrix}(2\pi/P)(\delta a/a_0)\\ (2\pi/P')(\delta a'/a_0'),\end{pmatrix}, \tag{3.52}$$

where T and T' are constants. We choose $\lambda = 0$ in the direction of our line of sight, in which case T and T' roughly correspond to the times of particular transit centers.

In Equation (3.52), $\delta a/a_0$ and $\delta a'/a_0'$ are obtained by substituting $a = a_0 + \delta a$ and $a' = a_0' + \delta a'$ into Equations (3.46) and (3.47). Only keeping the terms of $\mathcal{O}(\delta a/a_0)$, $\mathcal{O}(\delta a'/a_0')$, $\mathcal{O}(e^2)$, and $\mathcal{O}(e'^2)$, we obtain

$$\frac{\delta a}{a_0} = -(j-1)\left(e^2 + \frac{\mu'}{\mu\sqrt{\alpha}}e'^2\right), \tag{3.53}$$

$$\frac{\delta a'}{a_0'} = j\frac{\mu\sqrt{\alpha}}{\mu'}\left(e^2 + \frac{\mu'}{\mu\sqrt{\alpha}}e'^2\right), \tag{3.54}$$

where $\mu \equiv m/M_\star$ and $\mu' \equiv m'/M_\star$. Thus, to evaluate the variations of the mean longitudes, we need to evaluate the variations of eccentricities as will be done next.

Variation of the Eccentricity e

In order to evaluate the variations of the eccentricities, we introduce the *complex eccentricity* $z \equiv e\mathrm{e}^{\mathrm{i}\varpi}$ and $z' \equiv e'\mathrm{e}^{\mathrm{i}\varpi'}$. The disturbing function (3.32) is then rewritten as

$$\mathcal{R}^j = \mathrm{Re}\left[fe\mathrm{e}^{\mathrm{i}(\lambda^j - \varpi)} + ge'\mathrm{e}^{\mathrm{i}(\lambda^j - \varpi')}\right] = \frac{1}{2}(fz^* + gz'^*)\mathrm{e}^{\mathrm{i}\lambda^j} + \mathrm{c.c.}, \tag{3.55}$$

where the asterisk and c.c. denote the complex conjugate of the preceding terms. Noting the relation

$$\frac{\partial}{\partial\gamma} = -\frac{\partial}{\partial\varpi} = -\frac{\partial z}{\partial\varpi}\frac{\partial}{\partial z} - \frac{\partial z^*}{\partial\varpi}\frac{\partial}{\partial z^*} = 2\mathrm{Re}\left(\mathrm{i}z^*\frac{\partial}{\partial z^*}\right) \tag{3.56}$$

derived from the definition of z, the equation of motion for Γ

$$\frac{\mathrm{d}\Gamma}{\mathrm{d}t} = -\frac{\partial\mathcal{H}}{\partial\gamma} \tag{3.57}$$

is rewritten as that for z:

$$\frac{\mathrm{d}}{\mathrm{d}t}\begin{pmatrix}z\\ z'\end{pmatrix} = \mathrm{i}\frac{2\pi}{P'}\begin{pmatrix}\mu' f/\sqrt{\alpha}\\ \mu g\end{pmatrix}\mathrm{e}^{\mathrm{i}\lambda^j}. \tag{3.58}$$

In deriving Equation (3.58), we dropped the terms of $\mathcal{O}(\mu e^2)$. In order to integrate Equation (3.58), we use the relation

$$\frac{\mathrm{d}}{\mathrm{d}t}\lambda^j = \frac{2\pi j}{P'} - \frac{2\pi(j-1)}{P} + \mathcal{O}(e^2, e'^2) = -(j\Delta)\frac{2\pi}{P'} + \mathcal{O}(e^2, e'^2), \tag{3.59}$$

obtained from Equations (3.52), (3.53), and (3.54). Here we defined the normalized distance to the resonance as

$$\Delta \equiv \frac{j-1}{j}\frac{P'}{P} - 1. \tag{3.60}$$

Note that $|\Delta| \ll 1$ because the two planets are assumed to be in near a $j : j-1$ resonance (*i.e.*, $P'/P \sim j/(j-1)$). Using Equation (3.59), the solution of Equation (3.58) becomes

$$\begin{pmatrix} z \\ z' \end{pmatrix} = \begin{pmatrix} z_{\rm free} \\ z'_{\rm free} \end{pmatrix} - \frac{1}{j\Delta}\begin{pmatrix} \mu' f/\sqrt{\alpha} \\ \mu g \end{pmatrix} \mathrm{e}^{\mathrm{i}\lambda^j} \equiv \begin{pmatrix} z_{\rm free} + z_{\rm forced} \\ z'_{\rm free} + z'_{\rm forced} \end{pmatrix}, \tag{3.61}$$

where $z_{\rm free}$ and $z'_{\rm free}$ are constants called *free eccentricities*, and we defined the *force eccentricities* $z_{\rm forced}$ and $z'_{\rm forced}$ in the last equality.[1]

With these expressions, we can now evaluate $\delta a/a_0$ and $\delta a'/a'_0$ given in Equations (3.53) and (3.54). The quantity in the parentheses of these equations can be calculated using $e^2 = zz^*$ and $e'^2 = z'z'^*$ as

$$\begin{aligned} &e^2 + \frac{\mu'}{\mu\sqrt{\alpha}}e'^2 \\ &= |z_{\rm free}|^2 + \frac{\mu'}{\mu\sqrt{\alpha}}|z'^2_{\rm free}| + \frac{1}{(j\Delta)^2}\left[\frac{(\mu' f)^2}{\alpha} + (\mu g)^2\right] - \frac{1}{j\Delta}\frac{\mu'}{\sqrt{\alpha}}\left(Z^*_{\rm free}\mathrm{e}^{\mathrm{i}\lambda^j} + \text{c.c.}\right), \end{aligned} \tag{3.62}$$

where

$$Z_{\rm free} \equiv f z_{\rm free} + g z'_{\rm free}. \tag{3.63}$$

Therefore, the time-dependent parts of $\delta a/a_0$ and $\delta a'/a'_0$ become[2]

$$\begin{pmatrix} \delta a/a_0 \\ \delta a'/a'_0 \end{pmatrix} = \begin{pmatrix} \frac{j-1}{j}\mu'/\sqrt{\alpha} \\ -\mu \end{pmatrix} \frac{Z^*_{\rm free}}{\Delta}\mathrm{e}^{\mathrm{i}\lambda^j} + \text{c.c.}. \tag{3.64}$$

Substituting Equation (3.64) into Equation (3.52), we obtain

$$\begin{pmatrix} \lambda \\ \lambda' \end{pmatrix} = \begin{pmatrix} \frac{2\pi}{P}(t-T) \\ \frac{2\pi}{P'}(t-T') \end{pmatrix} + \begin{pmatrix} \mu' \frac{j-1}{j}\alpha^{-2} \\ \mu \end{pmatrix} \frac{3Z^*_{\rm free}}{2\mathrm{i}j\Delta^2}\mathrm{e}^{\mathrm{i}\lambda^j} + \text{c.c.}. \tag{3.65}$$

Here we use Equation (3.59) again to integrate $\mathrm{e}^{\mathrm{i}\lambda^j}$ in Equation (3.64).

[1] The terms "free" and "forced" seem to come from the analogy with the free and forced elements in the theory of secular perturbations (*e.g.*, Murray and Dermott 1999, §7.9). The $z_{\rm free}$ can be interpreted as the "intrinsic" eccentricity of the planet, while $z_{\rm forced}$ corresponds to the eccentricity excited by the resonant perturbations.

[2] Equation (3.62) also contains the time-independent components of $\mathcal{O}(e^2)$ and $\mathcal{O}((\mu/\Delta)^2)$), which result in the constant shifts of semi-major axes from a_0 and a'_0. For this reason, the real mean periods are slightly different from those defined in Equation (3.51).

TTV signals: Conversion from λ to θ

Now that we have the expressions for the mean longitudes, Equation (3.65), and eccentricities, Equation (3.61), we are ready to evaluate Equation (3.24). Using the complex eccentricity defined above, Equation (3.24) can be rewritten as

$$\theta = \lambda + 2e\sin(\lambda - \varpi) = \lambda + \frac{z^*}{\mathrm{i}}\mathrm{e}^{\mathrm{i}\lambda} + \text{c.c.}, \tag{3.66}$$

where the function $\lambda(t)$ is already given by Equation (3.65). The second and third terms can also be calculated from Equation (3.61) as

$$\frac{z^*}{\mathrm{i}}\mathrm{e}^{\mathrm{i}\lambda} + \text{c.c.} = \frac{z^*_{\text{free}}}{\mathrm{i}}\mathrm{e}^{\mathrm{i}\lambda} - \frac{1}{j\Delta}\frac{\mu' f}{\sqrt{\alpha}}\mathrm{e}^{\mathrm{i}(\lambda-\lambda^j)} + \text{c.c.} = \left[\frac{z^*_{\text{free}}}{\mathrm{i}} - \frac{1}{j\Delta}\frac{\mu' f}{\sqrt{\alpha}}\mathrm{e}^{\mathrm{i}\lambda^j}\right]\mathrm{e}^{\mathrm{i}\lambda} + \text{c.c.} \tag{3.67}$$

and

$$\frac{z'^*}{\mathrm{i}}\mathrm{e}^{\mathrm{i}\lambda'} + \text{c.c.} = \left[\frac{z'^*_{\text{free}}}{\mathrm{i}} - \frac{\mu g}{j\Delta}\mathrm{e}^{\mathrm{i}\lambda^j}\right]\mathrm{e}^{\mathrm{i}\lambda'} + \text{c.c.} \tag{3.68}$$

for the inner and outer planets, respectively. Since $\mathrm{e}^{\mathrm{i}\lambda}$ and $\mathrm{e}^{\mathrm{i}\lambda'}$ have almost the same periods as those of the orbital motions P and P', respectively, they can be set to unity at every transit by choosing the observer at $\lambda = 0$.[3] In this case, the first terms in the brackets of Equations (3.67) and (3.68) can also be dropped in calculating variations of the transit times. Therefore, the final expressions for θ and θ' with constant terms dropped are

$$\theta = \frac{2\pi}{P}\left[t - T - \left(\frac{V}{2\mathrm{i}}\mathrm{e}^{\mathrm{i}\lambda^j} + \text{c.c.}\right)\right], \tag{3.69}$$

$$\theta' = \frac{2\pi}{P'}\left[t - T' - \left(\frac{V'}{2\mathrm{i}}\mathrm{e}^{\mathrm{i}\lambda^j} + \text{c.c.}\right)\right], \tag{3.70}$$

where the complex TTVs are given by

$$\begin{aligned} V &= \frac{P}{\pi}\frac{\mu'}{j\Delta}\alpha^{-1/2}\left(-f - \frac{j-1}{j}\alpha^{-3/2}\frac{3Z^*_{\text{free}}}{2\Delta}\right) \\ &\simeq \frac{P}{\pi}\frac{\mu'}{j^{2/3}(j-1)^{1/3}\Delta}\left(-f - \frac{3}{2}\frac{Z^*_{\text{free}}}{\Delta}\right), \end{aligned} \tag{3.71}$$

$$V' = \frac{P'}{\pi}\frac{\mu}{j\Delta}\left(-g + \frac{3Z^*_{\text{free}}}{2\Delta}\right). \tag{3.72}$$

In the last equality of Equation (3.71), we use $\alpha = (1+\Delta)^{-2/3}(1-1/j)^{2/3}$ and drop $\mathcal{O}(\Delta)$ corrections.

Equations (3.69) and (3.70) show that the resulting TTVs are

$$\delta t = \frac{V}{2\mathrm{i}}\mathrm{e}^{\mathrm{i}\lambda^j} + \text{c.c.} = |V|\sin(\lambda^j + \arg V), \tag{3.73}$$

$$\delta t' = \frac{V'}{2\mathrm{i}}\mathrm{e}^{\mathrm{i}\lambda^j} + \text{c.c.} = |V'|\sin(\lambda^j + \arg V'), \tag{3.74}$$

[3] In Equations (3.67) and (3.68), $\mathrm{e}^{\mathrm{i}\lambda}$ and $\mathrm{e}^{\mathrm{i}\lambda'}$ are already multiplied by a small factor of $\mathcal{O}(e)$ or $\mathcal{O}(\mu)$, and so the second and third terms in Equation (3.65) can be neglected.

for the inner and outer planets, respectively, where $V = |V|\,\mathrm{e}^{\mathrm{i}\arg V}$ and $V' = |V'|\,\mathrm{e}^{\mathrm{i}\arg V'}$. Note that these two TTVs have the sinusoidal modulation of the same period

$$P^j \equiv \frac{1}{|j/P' - (j-1)/P|} = \frac{P'}{j|\Delta|} = \frac{P(1+\Delta)}{(j-1)|\Delta|} \tag{3.75}$$

derived from the definitions of λ^j and Δ in Equations (3.31) and (3.60). This P^j is called the *super-period* in Lithwick et al. (2012), and can be calculated from the observed periods of the two transiting planets alone. Another important feature is that the phases of the two TTVs are anti-correlated in the small-eccentricity limit $|Z_{\mathrm{free}}| \ll |\Delta|$, because it can be shown that f and g in Equations (3.71) and (3.72) have opposite signs (see Lithwick et al. (2012) or Appendix A). We can use these features to confirm that the two planets in near a $j : j-1$ resonance are really revolving around the same star. Applications of these formulae to real planetary systems are given in Lithwick et al. (2012) or Appendix A of this thesis.

Justification of Equation (3.48)

Finally, we check the validity of the approximation that drops the derivative of the disturbing function $\mathcal{R}^j$. Using Equations (3.33) and (3.64), Equation (3.48) can be written as

$$\begin{aligned}
\frac{\mathrm{d}\lambda}{\mathrm{d}t} &= \frac{1}{\sqrt{GM_\star}}\frac{2\sqrt{a}}{m}\frac{\partial\mathcal{H}}{\partial a} = \sqrt{\frac{GM_\star}{a^3}} - \frac{1}{\sqrt{GM_\star}}\frac{2\sqrt{a}}{m}\frac{Gmm'}{a'}\frac{\partial\mathcal{R}^j}{\partial a} \\
&= \sqrt{\frac{GM_\star}{a_0^3}}\left(1 - \frac{3}{2}\frac{\delta a}{a_0}\right) - \frac{1}{\sqrt{GM_\star}}\frac{2\sqrt{a}}{m}\mathcal{O}\left(\frac{Gmm'}{a'}\frac{e}{a}\right) \\
&= \sqrt{\frac{GM_\star}{a_0^3}}\left[1 + \mathcal{O}(\mu' e/\Delta) + \mathcal{O}(\mu' e)\right],
\end{aligned} \tag{3.76}$$

where e in the Landau symbol represents the first order in e or e'. Thus, the third term in Equation (3.76) we neglected is smaller than the second term we kept by Δ, which is typically of order 10^{-2}.

3.2.3 Contribution from the Secular Components

Here we discuss the effect of orbital precession (*i.e.*, deviation of κ from n due to non-Keplerian effects) on the transit timings. We consider the three effects below that drive the precession, following Miralda-Escudé (2002):

1. General relativity
2. Stellar quadrupole moment
3. Secular component of the perturbations from other planets

In the following discussion, we consider the time scale much shorter than the precession time scale. That is, we assume $\dot{\varpi}t = (n-\kappa)t \ll 1$. Also neglecting the terms of $\mathcal{O}((\dot{\varpi}/n)^2)$

and higher, we can iteratively solve $\phi(t) = 0 \pmod{2\pi}$, where $\phi(t)$ is given by Equation (3.18), and find

$$\begin{aligned} t &= -\frac{\phi_0}{n} + \frac{2\pi}{n}m - 2\left(1 - \frac{\dot{\varpi}}{n}\right)^{-1} \frac{e}{n}\sin(nt+\alpha) - 2e\frac{\dot{\varpi}}{n}t\cos(nt+\alpha) \\ &= -\frac{\phi_0}{n} + \frac{2\pi}{n}m - 2\left(1 - \frac{\dot{\varpi}}{n}\right)^{-1} \frac{e}{n}\sin(\alpha-\phi_0) + 2e\frac{\dot{\varpi}}{n}\frac{\phi_0}{n}\cos(\alpha-\phi_0) - 2e\frac{\dot{\varpi}}{n}\frac{2\pi m}{n}\cos(\alpha-\phi_0) \\ &= \frac{2\pi}{n}\left[1 - 2e\frac{\dot{\varpi}}{n}\cos(\alpha-\phi_0)\right]m + t_0, \end{aligned} \tag{3.77}$$

where m is an integer and

$$t_0 \equiv \frac{1}{n}\left[2e\frac{\dot{\varpi}}{n}\phi_0\cos(\alpha-\phi_0) - 2e\left(1-\frac{\dot{\varpi}}{n}\right)^{-1}\sin(\alpha-\phi_0) - \phi_0\right] \tag{3.78}$$

is a constant independent of m. Equation (3.77) shows that the deviation of the transit times δt from the mean period $P \equiv 2\pi/n$ is approximately given as

$$\frac{\delta t}{P} \simeq 2e\,\frac{\dot{\varpi}}{n}. \tag{3.79}$$

Thus, the evaluation of δt reduces to computing $\dot{\varpi}/n$. As we will see below, the secular effects are usually much smaller than those from the resonant terms, which yield $\delta t/P \sim P\mu/\Delta \gtrsim 10^{-6}/\Delta$ from Equations (3.71) and (3.72).

General Relativity

The general relativistic precession rate is given by

$$\dot{\varpi} = \frac{n}{2\pi}\frac{3\pi}{2}\left(\frac{2GM_\star}{hc}\right)^2 = n\,\frac{3}{1-e^2}\left(\frac{na}{c}\right)^2. \tag{3.80}$$

Thus, for small e, we have

$$\frac{\dot{\varpi}}{n} = 4\times10^{-7}\left(\frac{P}{10\,\mathrm{days}}\right)^{-2}\left(\frac{a}{0.1\,\mathrm{AU}}\right)^2, \tag{3.81}$$

and

$$\delta t \simeq 6\times10^{-4}\,\mathrm{min}\left(\frac{P}{10\,\mathrm{d}}\right)^{-1}\left(\frac{e}{0.05}\right)\left(\frac{a}{0.1\,\mathrm{AU}}\right)^2. \tag{3.82}$$

Stellar Quadrupole Moment

We consider a star that has an axisymmetric density distribution $\rho(\boldsymbol{r})$. In the spherical coordinate system (r,θ,φ) centered on the star, with its z-axis taken along the axis of

symmetry, the gravitational potential outside the star is given by

$$\begin{aligned}\phi(\boldsymbol{r}) &= -G\int \frac{\rho(\boldsymbol{r}')}{|\boldsymbol{r}-\boldsymbol{r}'|}\mathrm{d}^3\boldsymbol{r}' = -\frac{GM_\star}{r}\sum_{l=0}^{\infty}\frac{1}{M_\star}\int \mathrm{d}^3\boldsymbol{r}'\rho(\boldsymbol{r}')\left(\frac{r'}{r}\right)^l P_l(\cos\beta)\\ &\simeq -\frac{GM_\star}{r}\frac{1}{M_\star}\left[\int \mathrm{d}^3\boldsymbol{r}'\rho(\boldsymbol{r}') + \int \mathrm{d}^3\boldsymbol{r}'\rho(\boldsymbol{r}')\left(\frac{r'}{r}\right)^2 P_2(\cos\beta)\right]\\ &= -\frac{GM_\star}{r} - \frac{GM_\star}{r}\frac{1}{M_\star}\int \mathrm{d}^3\boldsymbol{r}'\rho(\boldsymbol{r}')\left(\frac{r'}{r}\right)^2 [P_2(\cos\theta)P_2(\cos\theta')+\cdots]\\ &= -\frac{GM_\star}{r} - \frac{GM_\star R_\star^2}{r^3}P_2(\cos\theta)\frac{1}{M_\star R_\star^2}\int \mathrm{d}^3\boldsymbol{r}'\rho(\boldsymbol{r}')r'^2 P_2(\cos\theta')\\ &= -\frac{GM_\star}{r} + \frac{J_2}{2}\frac{GM_\star R_\star^2}{r^3}(3\cos^2\theta-1),\end{aligned} \tag{3.83}$$

where β is the angle between $\boldsymbol{r}$ and $\boldsymbol{r}'$ and we use the addition theorem for the Legendre functions

$$P_l(\cos\beta) = P_l(\cos\theta)P_l(\cos\theta') + 2\sum_{m=1}^{l}\frac{(l-m)!}{(l+m)!}P_l^m(\cos\theta)P_l^m(\cos\theta')\cos m(\varphi-\varphi') \tag{3.84}$$

in the third line. The non-dimensional quantity

$$J_2 \equiv -\frac{1}{M_\star R_\star^2}\int \mathrm{d}^3\boldsymbol{r}'\rho(\boldsymbol{r}')r'^2 P_2(\cos\theta') \tag{3.85}$$

is called the *stellar quadrupole moment* (Zharkov and Trubitsyn 1974).

Suppose that a planet is moving in the $\theta = \pi/2$ plane under the influence of the potential given by Equation (3.83). Equations (3.13) and (3.12) yield

$$n^2 = \frac{1}{r}\frac{\mathrm{d}\phi(\theta=\pi/2)}{\mathrm{d}r} = \frac{GM_\star}{r^3} + \frac{3J_2}{2}\frac{GM_\star R_\star^2}{r^5}, \tag{3.86}$$

$$\kappa^2 = r\frac{\mathrm{d}n^2}{\mathrm{d}r} + 4n^2 = -\frac{3GM_\star}{r^3} - \frac{15J_2}{2}\frac{GM_\star R_\star^2}{r^5} + 4n^2 = n^2 - \frac{3J_2 GM_\star R_\star^2}{r^5}, \tag{3.87}$$

and thus

$$\dot{\varpi} = n - \kappa = \frac{3J_2 R_\star^2}{2a^2}n. \tag{3.88}$$

Here we substitute $r = a$, where a is equivalent to the guiding center radius defined by Equation (3.7) and also to the orbital semi-major axis to the first order of e. Therefore, we have

$$\frac{\dot{\varpi}}{n} = 1.5\times10^{-8}\left(\frac{J_2}{10^{-6}}\right)\left(\frac{a/R_\star}{10}\right)^{-2}, \tag{3.89}$$

and

$$\delta t \simeq 2\times10^{-5}\min\left(\frac{P}{10\,\mathrm{d}}\right)\left(\frac{e}{0.05}\right)\left(\frac{J_2}{10^{-6}}\right)\left(\frac{a/R_\star}{10}\right)^{-2}. \tag{3.90}$$

Secular Component of the Perturbations from the Outer Planet

Here we consider the two-planet system and see how the perturbations from the outer planet (mass m_2, semi-major axis a_2) affect the transit times of the inner planet (mass m, semi-major axis a). For simplicity, we assume that they are in the circular and coplanar orbits, and that $a_2 \gg a$. In this case, the time-averaged potential due to the outer planet is

$$\begin{aligned}\phi_2(r) &= -\frac{Gm_2}{a_2}\int_0^{2\pi}\frac{1}{2\pi a_2}\frac{a_2 \mathrm{d}\varphi}{\sqrt{1+(r/a_2)^2-2(r/a_2)\cos\varphi}} \\ &\simeq -\frac{Gm_2}{a_2}\frac{1}{2\pi}\int_0^{2\pi}\left[1+\left(\frac{r}{a_2}\right)^2\left(\frac{3}{2}\cos^2\varphi-\frac{1}{2}\right)\right]\mathrm{d}\varphi \\ &= -\frac{Gm_2}{a_2}\left(1+\frac{r^2}{4a_2^2}\right). \end{aligned} \tag{3.91}$$

Thus, Equations (3.13) and (3.12) give

$$n^2 = \frac{GM_\star}{r^3}-\frac{Gm_2}{2a_2^3}, \tag{3.92}$$

$$\kappa^2 = -\frac{3GM_\star}{r^3}+4n^2 = n^2-\frac{3Gm_2}{2a_2^3}, \tag{3.93}$$

and

$$\dot{\varpi} = \frac{n^2-\kappa^2}{2n} = \frac{3Gm_2}{4a_2^3 n} = \frac{3m_2a^3}{4M_\star a_2^3}\,n. \tag{3.94}$$

Equation (3.94) corresponds to

$$\frac{\dot{\varpi}}{n} = 3\times10^{-7}\left(\frac{m_2/M_\star}{3\times10^{-6}}\right)\left(\frac{a_2/a}{2}\right)^{-3}, \tag{3.95}$$

and

$$\delta t \simeq 4\times10^{-4}\min\left(\frac{P}{10\,\mathrm{d}}\right)\left(\frac{e}{0.05}\right)\left(\frac{m_2/M_\star}{3\times10^{-6}}\right)\left(\frac{a_2/a}{2}\right)^{-3}. \tag{3.96}$$

Note that Equation (3.96) results in the scaling $\delta t/P \propto (a_2/a)^{-3}$, which is much steeper than that obtained from Equation (3.71), $|V| \sim P/P' \sim (a_2/a)^{-3/2}$. Thus, the resonance perturbation dominates the secular one, even if the planets are far from the near commensurability (Agol et al. 2005).

3.3 *Kepler* Planets Confirmed with TTVs

As of December 2013, 121 *Kepler* planets have been confirmed using TTVs, as listed in Table 3.1. Among these, 33 planets in 14 multi-transiting systems have well-determined masses, based on the detailed dynamical TTV modeling as in Chapters 5 and 6 of this thesis. For the other systems, TTVs are used to show that the planet candidates in each of the systems are really revolving around the same star, by examining the presence of correlations in their TTV signals. In order to show that they are indeed planetary (not

stellar) objects, the mass upper limits are given by the condition that the dynamically interacting system is stable over the long ($\sim 10\,\mathrm{Myr}$) time scale, except for the systems confirmed by Xie (2013b) (see the note of the table). For this reason, the latter group of planets are subject to the future detailed TTV modeling, and so tabulated separately.

Table 3.1. List of *Kepler* Planets Characterized Using TTVs

Planet	Period (day)	Mass ($M_\oplus$)	Radius ($R_\oplus$)	Density ($\mathrm{g\,cm^{-3}}$)	Reference
Planets with well-determined masses					
Kepler-9b	19.243158	80.1 ± 4.1	9.43 ± 0.77	0.524 ± 0.132	Holman et al. (2010)
Kepler-9c	38.9086	54.3 ± 4.1	9.21 ± 0.75	0.383 ± 0.098	Holman et al. (2010)
Kepler-11b	10.3038	$1.9^{+1.4}_{-1.0}$	$1.80^{+0.03}_{-0.05}$	$1.72^{+1.25}_{-0.91}$	Lissauer et al. (2013)
Kepler-11c	13.025020	$2.9^{+2.9}_{-1.6}$	$2.87^{+0.05}_{-0.06}$	$0.66^{+0.66}_{-0.35}$	Lissauer et al. (2013)
Kepler-11d	22.6872	$7.3^{+0.8}_{-1.5}$	$3.12^{+0.06}_{-0.07}$	$1.28^{+0.14}_{-0.27}$	Lissauer et al. (2013)
Kepler-11e	31.9959	$8.0^{+1.5}_{-2.1}$	$4.19^{+0.07}_{-0.09}$	$0.58^{+0.11}_{-0.16}$	Lissauer et al. (2013)
Kepler-11f	46.6888	$2.0^{+0.8}_{-0.9}$	$2.49^{+0.04}_{-0.07}$	$0.69^{+0.29}_{-0.32}$	Lissauer et al. (2013)
Kepler-16(AB)b	228.776	105.8 ± 5.1	8.44 ± 0.03	$0.964^{+0.047}_{-0.046}$	Doyle et al. (2011)
Kepler-18b[1]	3.504725	6.9 ± 3.4	2.0 ± 0.1	4.9 ± 2.4	Cochran et al. (2011)
Kepler-18c[1]	7.641590	17.3 ± 1.9	5.49 ± 0.26	0.59 ± 0.07	Cochran et al. (2011)
Kepler-18d[1]	14.858880	16.4 ± 1.4	6.98 ± 0.33	0.27 ± 0.03	Cochran et al. (2011)
Kepler-30b	29.334	11.3 ± 1.4	3.9 ± 0.2	1.02 ± 0.13	Sanchis-Ojeda et al. (2012)
Kepler-30c	60.3231	640 ± 50	12.3 ± 0.4	1.88 ± 0.17	Sanchis-Ojeda et al. (2012)
Kepler-30d	143.343	23.1 ± 2.7	8.8 ± 0.5	0.19 ± 0.02	Sanchis-Ojeda et al. (2012)
Kepler-34(AB)b	288.822	$69.9^{+3.5}_{-3.2}$	$8.553^{+0.134}_{-0.157}$	$0.613^{+0.045}_{-0.041}$	Welsh et al. (2012)
Kepler-35(AB)b	131.458	40.4 ± 6.4	8.15 ± 0.157	$0.41^{+0.070}_{-0.069}$	Welsh et al. (2012)
Kepler-36b	13.8399	$4.45^{+0.33}_{-0.27}$	1.486 ± 0.035	$7.46^{+0.74}_{-0.59}$	Carter et al. (2012)
Kepler-36c	16.2386	$8.08^{+0.60}_{-0.46}$	3.679 ± 0.054	$0.89^{+0.07}_{-0.05}$	Carter et al. (2012)
Kepler-46c[2]	57.011	$119.5^{+6.7}_{-6.0}$	...	...	Nesvorný et al. (2012)
Kepler-51b	45.155502	$2.1^{+1.5}_{-0.8}$	7.1 ± 0.3	$0.03^{+0.02}_{-0.01}$	Masuda (2014)
Kepler-51c	85.3129	4.0 ± 0.4	$9.0^{+2.8}_{-1.7}$	$0.03^{+0.02}_{-0.03}$	Masuda (2014)
Kepler-51d	130.183	7.6 ± 1.1	9.7 ± 0.5	0.046 ± 0.009	Masuda (2014)
Kepler-79b	13.484697	$10.9^{+7.4}_{-6.0}$	3.47 ± 0.07	$1.43^{+0.97}_{-0.78}$	Jontof-Hutter et al. (2013)
Kepler-79c	27.4029	$5.9^{+1.9}_{-2.3}$	3.72 ± 0.08	$0.62^{+0.20}_{-0.25}$	Jontof-Hutter et al. (2013)
Kepler-79d	52.0902	$6.0^{+2.1}_{-1.6}$	$7.16^{+0.13}_{-0.16}$	$0.09^{+0.03}_{-0.02}$	Jontof-Hutter et al. (2013)
Kepler-79e	81.0659	$4.1^{+1.2}_{-1.1}$	3.49 ± 0.14	0.53 ± 0.15	Jontof-Hutter et al. (2013)
Kepler-87b	114.737	324.2 ± 8.8	13.49 ± 0.55	0.729 ± 0.026	Ofir et al. (2013)
Kepler-87c	192.363	6.4 ± 0.8	6.14 ± 0.29	0.152 ± 0.019	Ofir et al. (2013)
Kepler-88b	10.954200	8.7 ± 2.5	$3.78^{+0.39}_{-0.36}$	$0.87^{+0.42}_{-0.31}$	Nesvorný et al. (2013)
Kepler-88c[2]	22.1	$198.8^{+9.2}_{-10.6}$	...	...	Nesvorný et al. (2013)
Kepler-89c	10.423707	$9.4^{+2.4}_{-2.1}$	3.84 ± 0.06	$0.92^{+0.23}_{-0.21}$	Masuda et al. (2013)
Kepler-89d	22.343000	$52.1^{+6.9}_{-7.1}$	10.5 ± 0.15	0.25 ± 0.03	Masuda et al. (2013)
Kepler-89e	54.3199	$13.0^{+2.5}_{-2.1}$	6.18 ± 0.09	$0.30^{+0.06}_{-0.05}$	Masuda et al. (2013)
Planets with mass upper limits					
Kepler-11g	118.378	< 25	$3.33^{+0.06}_{-0.08}$	< 4	Lissauer et al. (2013)
Kepler-19c[2]	< 160	< 1906.9	...	...	Ballard et al. (2011)
Kepler-23b	7.1073	< 254.2	1.9	< 204.4	Ford et al. (2012)
Kepler-23c	10.7421	< 858.1	3.2	< 144.4	Ford et al. (2012)
Kepler-24b	8.1453	< 508.5	2.4	< 202.9	Ford et al. (2012)
Kepler-24c	12.3335	< 508.5	2.8	< 127.7	Ford et al. (2012)
Kepler-25b	6.2385	< 4036.2	2.6	< 1266.5	Steffen et al. (2012)
Kepler-25c	12.7204	< 1322.1	4.5	< 80	Steffen et al. (2012)
Kepler-26b	12.2829	< 120.8	3.6	< 14.3	Steffen et al. (2012)
Kepler-26c	17.2513	< 119.2	3.6	< 14.1	Steffen et al. (2012)
Kepler-27b	15.3348	< 2895.3	4.0	< 249.5	Steffen et al. (2012)
Kepler-27c	31.3309	< 4385.8	4.9	< 205.6	Steffen et al. (2012)

Table 3.1 (cont'd)

Planet	Period (day)	Mass ($M_\oplus$)	Radius ($R_\oplus$)	Density ($\mathrm{g\,cm^{-3}}$)	Reference
Kepler-28b	5.9123	< 479.9	3.6	< 56.7	Steffen et al. (2012)
Kepler-28c	8.9858	< 432.2	3.4	< 60.6	Steffen et al. (2012)
Kepler-29b	10.3376	< 127.1	3.6 ± 0.5	< 15	Fabrycky et al. (2012)
Kepler-29c	13.2907	< 95.3	2.9 ± 0.4	< 21.6	Fabrycky et al. (2012)
Kepler-31b	20.8613	< 2161.1	5.5 ± 1.1	< 71.6	Fabrycky et al. (2012)
Kepler-31c	42.6318	< 1493.7	5.3 ± 1.1	< 55.3	Fabrycky et al. (2012)
Kepler-32b	5.90124	< 1303	2.2 ± 0.2	< 674.9	Fabrycky et al. (2012)
Kepler-32c	8.7522	< 158.9	2.0 ± 0.2	< 109.5	Fabrycky et al. (2012)
Kepler-46b	33.6013	< 1907	$9.045^{+0.47}_{-0.481}$	< 14	Nesvorný et al. (2012)
Kepler-48b	4.777980	< 614.3	2.14 ± 0.12	< 345.7	Xie (2013a)
Kepler-48c	9.673928	< 17.9	3.14 ± 0.18	< 3.2	Xie (2013a)
Kepler-49b	7.203794	< 30.4	2.72 ± 0.12	< 8.3	Xie (2013a)
Kepler-49c	10.912934	< 67.9	2.55 ± 0.13	< 22.6	Xie (2013a)
Kepler-50b	7.812512	< 323	2.2	< 167.3	Steffen et al. (2013)
Kepler-50c	9.376137	< 238	2.79	< 60.4	Steffen et al. (2013)
Kepler-52b	7.877357	< 2870	2.1	< 1709.1	Steffen et al. (2013)
Kepler-52c	16.385	< 3440	1.84	< 3045.4	Steffen et al. (2013)
Kepler-53b	18.649	< 178.6	2.89 ± 0.17	< 40.8	Xie (2013a)
Kepler-53c	38.5583	< 61.9	3.17 ± 0.19	< 10.7	Xie (2013a)
Kepler-54b	8.010943	< 292.4	2.1	< 174.1	Steffen et al. (2013)
Kepler-54c	12.0717	< 117.6	1.23	< 348.5	Steffen et al. (2013)
Kepler-55b	27.9481	< 473.5	2.43	< 182	Steffen et al. (2013)
Kepler-55c	42.151642	< 352.8	2.21	< 180.2	Steffen et al. (2013)
Kepler-56b	10.5016	< 1627.2	3.84	< 158.5	Steffen et al. (2013)
Kepler-56c	21.4024	< 3870.9	7.85	< 44.1	Steffen et al. (2013)
Kepler-57b	5.729320	< 50.9	2.19 ± 0.95	< 26.7	Xie (2013a)
Kepler-57c	11.609257	< 15	1.55 ± 0.67	< 22.2	Xie (2013a)
Kepler-58b	10.2185	< 182.1	2.78 ± 1.18	< 46.7	Steffen et al. (2013)
Kepler-58c	15.5742	< 238.8	2.86 ± 1.21	< 56.3	Steffen et al. (2013)
Kepler-59b	11.8682	< 651.5	1.1	< 2699.5	Steffen et al. (2013)
Kepler-59c	17.9801	< 435.4	1.98	< 309.3	Steffen et al. (2013)
Kepler-60b	7.131619	< 79.5	2.28	< 37	Steffen et al. (2013)
Kepler-60c	8.91935	< 178	2.47	< 65.1	Steffen et al. (2013)
Kepler-60d	11.9016	< 216.1	2.55	< 71.9	Steffen et al. (2013)
Kepler-80b	7.05	< 41.5	2.64 ± 0.11	< 12.4	Xie (2013a)
Kepler-80c	9.52	< 110.3	2.79 ± 0.13	< 28	Xie (2013a)
Kepler-81b	5.954893	< 129.2	2.42 ± 0.38	< 50.3	Xie (2013a)
Kepler-81c	12.039901	< 8.2	2.37 ± 0.37	< 3.4	Xie (2013a)
Kepler-82b	26.4429	< 7663.6	4.00 ± 1.82	< 660.4	Xie (2013a)
Kepler-82c	51.5301	< 133.8	5.35 ± 2.44	< 4.8	Xie (2013a)
Kepler-83b	9.770513	< 265.8	2.83 ± 0.41	< 64.7	Xie (2013a)
Kepler-83c	20.0898	< 18.3	2.36 ± 0.35	< 7.7	Xie (2013a)
Kepler-84b	8.725854	< 96.7	2.23 ± 0.10	< 48.1	Xie (2013a)
Kepler-84c	12.882525	< 675.1	2.36 ± 0.11	< 283.3	Xie (2013a)
Kepler-85b	8.30599	< 56.7	1.97 ± 0.1	< 40.9	Xie (2013a)[3]
Kepler-85c	12.5122	< 154.7	2.18 ± 0.1	< 82.4	Xie (2013a)[3]
Kepler-92b	13.749	< 51.4	3.51 ± 0.1	< 6.6	Xie (2013b)
Kepler-92c	26.723	< 28.3	2.60 ± 0.08	< 8.9	Xie (2013b)

Table 3.1 (cont'd)

Planet	Period (day)	Mass ($M_\oplus$)	Radius ($R_\oplus$)	Density ($\mathrm{g\,cm^{-3}}$)	Reference
Kepler-114c	8.041	< 45.3	1.60 ± 0.18	< 61	Xie (2013b)
Kepler-114d	11.776	< 22.6	2.53 ± 0.28	< 7.7	Xie (2013b)
Kepler-128b	15.09	< 589.8	1.13 ± 0.03	< 2254.3	Xie (2013b)
Kepler-128c	22.804	< 122.9	1.13 ± 0.03	< 469.7	Xie (2013b)
Kepler-145b	22.951	< 68.3	2.65 ± 0.08	< 20.2	Xie (2013b)
Kepler-145c	42.882	< 183.1	4.32 ± 0.12	< 12.5	Xie (2013b)
Kepler-177b	35.855	< 102.4	$2.90^{+1.52}_{-0.30}$	< 23.2	Xie (2013b)
Kepler-177c	49.412	< 49.1	$7.10^{+3.71}_{-0.72}$	< 0.8	Xie (2013b)
Kepler-238b	23.654	< 188.5	$5.60^{+2.37}_{-0.46}$	< 5.9	Xie (2013b)
Kepler-238c	50.447	< 1758.5	$2.00^{+0.85}_{-0.17}$	< 1212.3	Xie (2013b)
Kepler-276b	31.884	< 82.2	$2.90^{+1.27}_{-0.28}$	< 18.6	Xie (2013b)
Kepler-276c	48.648	< 74.9	$2.80^{+1.23}_{-0.27}$	< 18.8	Xie (2013b)
Kepler-277b	17.324	< 225.2	$2.92^{+0.73}_{-0.63}$	< 49.9	Xie (2013b)
Kepler-277c	33.006	< 1085.7	$3.36^{+0.83}_{-0.72}$	< 157.8	Xie (2013b)
Kepler-279b	35.736	< 79.7	$4.30^{+1.72}_{-0.41}$	< 5.5	Xie (2013b)[3]
Kepler-279c	54.414	< 31	$3.10^{+1.24}_{-0.30}$	< 5.7	Xie (2013b)[3]
Kepler-282b	24.806	< 4462.8	$2.46^{+1.00}_{-0.20}$	< 1653.3	Xie (2013b)
Kepler-282c	44.347	< 202.6	$3.10^{+1.26}_{-0.25}$	< 37.5	Xie (2013b)
Kepler-305b	5.487	< 51.9	$3.60^{+0.9}_{-0.36}$	< 6.1	Xie (2013b)[3]
Kepler-305c	8.291	< 60.1	$3.30^{+0.82}_{-0.33}$	< 9.2	Xie (2013b)[3]
Kepler-307b	10.416	< 22.1	$3.20^{+1.20}_{-0.46}$	< 3.7	Xie (2013b)
Kepler-307c	13.084	< 239.2	$2.80^{+1.05}_{-0.41}$	< 60.1	Xie (2013b)
Kepler-328b	34.921	< 23.6	$2.30^{+0.96}_{-0.23}$	< 10.7	Xie (2013b)
Kepler-328c	71.312	< 874.5	$5.40^{+2.24}_{-0.54}$	< 30.6	Xie (2013b)
Kepler-350b	17.849	< 33.6	$3.10^{+1.42}_{-0.60}$	< 6.2	Xie (2013b)
Kepler-350c	26.136	< 1117.4	$2.80^{+1.28}_{-0.54}$	< 280.7	Xie (2013b)
Kepler-396b	42.994	< 22.2	$3.50^{+1.28}_{-0.65}$	< 2.9	Xie (2013b)[3]
Kepler-396c	88.505	< 62	$5.30^{+1.95}_{-0.99}$	< 2.3	Xie (2013b)[3]

[1]Constraints obtained by the joint analysis of TTVs and RVs.

[2]Non-transiting planet.

[3]Also analyzed by Ming et al. (2013) independently.

Note. — The values of orbital periods are from The Extrasolar Planets Encyclopedia `http://www.exoplanet.eu` (errors are omitted for brevity). The other parameters are from the references in the sixth column.

Note. — This table does not include the mass estimates using analytic formulae by Lithwick et al. (2012) (*c.f.*, Section 3.2.2), because the estimated values are highly uncertain due to the degeneracies with eccentricities.

Note. — The mass upper limits are determined by the stability analysis, except for Kepler-11g (from TTVs) and for those given by Xie (2013b). Estimates by Xie (2013b) are based on the formulae by Lithwick et al. (2012), but the degeneracies mentioned above are taken into account.

Chapter 4

Numerical Methods for Analyzing TTV Signals

Since it is generally impossible to model the TTV signals analytically, we need numerical methods to integrate the planetary orbits. The fourth-order Hermite scheme discussed in this chapter is one of the efficient ways of N-body integration, which is based on the predictor-corrector method. In order to infer the model parameters by comparing the model TTVs with the observations, we adopt Bayesian analysis using a Markov chain Monte Carlo (MCMC) algorithm. In fact, the application of the MCMC is not limited to the TTV analysis, but also includes other problems in the study of exoplanets, such as the fit of radial velocities and transit light curves.

4.1 N-body Simulation using the Fourth-order Hermite Scheme[1]

4.1.1 Formulation

Here we summarize the fourth-order Hermite scheme described in Kokubo and Makino (2004). In this method, position $\boldsymbol{x}_j$ and velocity $\boldsymbol{v}_j$ of particle j at time $t_0 + \Delta t$ are calculated from $\boldsymbol{x}_j$, $\boldsymbol{v}_j$, acceleration $\boldsymbol{a}_j$, and its time derivative $\dot{\boldsymbol{a}}_j$ at time t_0. We consider the point masses with mass m_j that move under the mutual gravitational interaction described by Newtonian gravitation.[2]

First, $\boldsymbol{x}_j(t_0 + \Delta t)$ and $\boldsymbol{v}_j(t_0 + \Delta t)$ are predicted from $\boldsymbol{x}_j(t_0)$, $\boldsymbol{v}_j(t_0)$, $\boldsymbol{a}_j(t_0)$, and $\dot{\boldsymbol{a}}_j(t_0)$ as

$$\boldsymbol{x}_{\mathrm{p},j} = \boldsymbol{x}_{0,j} + \Delta t \boldsymbol{v}_{0,j} + \frac{\Delta t^2}{2} \boldsymbol{a}_{0,j} + \frac{\Delta t^3}{6} \dot{\boldsymbol{a}}_{0,j}, \tag{4.1}$$

$$\boldsymbol{v}_{\mathrm{p},j} = \boldsymbol{v}_{0,j} + \Delta t \boldsymbol{a}_{0,j} + \frac{\Delta t^2}{2} \dot{\boldsymbol{a}}_{0,j}. \tag{4.2}$$

Here, the subscript 0 denotes the quantity evaluated at time t_0, and we define $\boldsymbol{x}_{\mathrm{p},j} \equiv$

[1] This section is mainly based on 跡部恵子 他. (2006), 富阪幸治・花輪知幸・牧野淳一郎 編 (2007), and Kokubo and Makino (2004)

[2] The other kinds of forces can also be included by calculating $\boldsymbol{a}$ and $\dot{\boldsymbol{a}}$ as in Equations (4.3) and (4.4).

$\boldsymbol{x}_j(t_0+\Delta t)$ and $\boldsymbol{v}_{\mathrm{p},j} \equiv \boldsymbol{v}_j(t_0+\Delta t)$. These are called *predictors*. The precisions of $\boldsymbol{x}_{\mathrm{p},j}$ and $\boldsymbol{v}_{\mathrm{p},j}$ are of orders Δt^3 and Δt^2, respectively.

In order to determine $\mathcal{O}(\Delta t^4)$ and $\mathcal{O}(\Delta t^5)$ terms, we need to know the second and third derivatives of the acceleration, $\boldsymbol{a}_{0,j}^{(2)}$ and $\boldsymbol{a}_{0,j}^{(3)}$. These quantities are obtained by *Hermite interpolation*, in which we construct a polynomial that interpolates the values of $\boldsymbol{a}$ at times t_0 and $t_0+\Delta t$. For this purpose, we calculate $\boldsymbol{a}_{1,j} \equiv \boldsymbol{a}_j(t_0+\Delta t)$ and $\dot{\boldsymbol{a}}_{1,j} \equiv \dot{\boldsymbol{a}}_j(t_0+\Delta t)$ from the predictors $\boldsymbol{x}_{\mathrm{p},j}$ and $\boldsymbol{v}_{\mathrm{p},j}$ as

$$\boldsymbol{a}_{1,j} = -\sum_{k\neq j} Gm_k \frac{\boldsymbol{x}_{jk}}{(x_{jk}^2+\epsilon^2)^{3/2}}, \tag{4.3}$$

$$\dot{\boldsymbol{a}}_{1,j} = -\sum_{j} Gm_k \left[\frac{\boldsymbol{v}_{jk}}{(x_{jk}^2+\epsilon^2)^{3/2}} - \frac{3(\boldsymbol{v}_{jk}\cdot\boldsymbol{x}_{jk})\boldsymbol{x}_{jk}}{(x_{jk}^2+\epsilon^2)^{5/2}}\right], \tag{4.4}$$

where G is Newton's gravitational constant, ϵ is the softening parameter to avoid the divergence,[3] $\boldsymbol{x}_{jk} \equiv \boldsymbol{x}_{\mathrm{p},j} - \boldsymbol{x}_{\mathrm{p},k}$, and $\boldsymbol{v}_{jk} \equiv \boldsymbol{v}_{\mathrm{p},j} - \boldsymbol{v}_{\mathrm{p},k}$. Since the precisions of $\boldsymbol{x}_{\mathrm{p},j}$ and $\boldsymbol{v}_{\mathrm{p},j}$ are of orders Δt^3 and Δt^2, respectively, those of $\boldsymbol{a}_{1,j}$ and $\dot{\boldsymbol{a}}_{1,j}$ are of orders Δt^3 and Δt^2 as well.

Using $\boldsymbol{a}_{1,j}$ and $\dot{\boldsymbol{a}}_{1,j}$ in Equations (4.3) and (4.4), we determine $\boldsymbol{a}_{0,j}^{(2)}$ and $\boldsymbol{a}_{0,j}^{(3)}$ as follows. We interpolate $\boldsymbol{a}_j(t)$ for $t_0 \le t \le t_0+\Delta t$ as

$$\boldsymbol{a}_j(t) = \boldsymbol{a}_{0,j} + \dot{\boldsymbol{a}}_{0,j}(t-t_0) + \frac{\boldsymbol{a}_{0,j}^{(2)}}{2}(t-t_0)^2 + \frac{\boldsymbol{a}_{0,j}^{(3)}}{6}(t-t_0)^3. \tag{4.5}$$

By definition, this polynomial has to satisfy $\boldsymbol{a}_j(t=t_0+\Delta t) = \boldsymbol{a}_{1,j}$ and $\boldsymbol{a}_j(t_0) = \boldsymbol{a}_0$ (the latter is obvious). Thus, we have

$$\boldsymbol{a}_{1,j} = \boldsymbol{a}_{0,j} + \dot{\boldsymbol{a}}_{0,j}\Delta t + \frac{\boldsymbol{a}_{0,j}^{(2)}}{2}\Delta t^2 + \frac{\boldsymbol{a}_{0,j}^{(3)}}{6}\Delta t^3, \tag{4.6}$$

$$\dot{\boldsymbol{a}}_{1,j} = \dot{\boldsymbol{a}}_{0,j} + \boldsymbol{a}_{0,j}^{(2)}\Delta t + \frac{\boldsymbol{a}_{0,j}^{(3)}}{2}\Delta t^2, \tag{4.7}$$

which can be solved inversely to give

$$\boldsymbol{a}_{0,j}^{(2)} = \frac{-6(\boldsymbol{a}_{0,j}-\boldsymbol{a}_{1,j}) - \Delta t(4\dot{\boldsymbol{a}}_{0,j} + 2\dot{\boldsymbol{a}}_{1,j})}{\Delta t^2}, \tag{4.8}$$

$$\boldsymbol{a}_{0,j}^{(3)} = \frac{12(\boldsymbol{a}_{0,j}-\boldsymbol{a}_{1,j}) + 6\Delta t(\dot{\boldsymbol{a}}_{0,j}+\dot{\boldsymbol{a}}_{1,j})}{\Delta t^3}. \tag{4.9}$$

Finally, these $\boldsymbol{a}_{0,j}^{(2)}$ and $\boldsymbol{a}_{0,j}^{(3)}$ are used to correct the predictors in Equations (4.1) and (4.2) as

$$\boldsymbol{x}_{\mathrm{c},j} = \boldsymbol{x}_{\mathrm{p},j} + \frac{\boldsymbol{a}_{0,j}^{(2)}}{24}\Delta t^4 + \alpha\,\frac{\boldsymbol{a}_{0,j}^{(3)}}{120}\Delta t^5, \tag{4.10}$$

$$\boldsymbol{v}_{\mathrm{c},j} = \boldsymbol{v}_{\mathrm{p},j} + \frac{\boldsymbol{a}_{0,j}^{(2)}}{6}\Delta t^3 + \frac{\boldsymbol{a}_{0,j}^{(3)}}{24}\Delta t^4, \tag{4.11}$$

[3] In Chapters 5 and 6, we choose $\epsilon = 0$, because there occurs no close encounters that lead to the divergence of the force.

where the accuracy of integration is of order Δt^4. Therefore, α in Equation (4.10) can be treated as a free parameter, though $\alpha = 1$ in the usual Taylor expansion. Kokubo and Makino (2004) have shown that the secular error can be reduced by choosing

$$\alpha = \frac{7}{6}, \tag{4.12}$$

without changing the order of accuracy and the time-symmetric property discussed in Section 4.1.2. We adopt this choice in Chapters 5 and 6. In proceeding to the next time step, we use the correctors $\boldsymbol{x}_{\mathrm{c},j}$ and $\boldsymbol{v}_{\mathrm{c},j}$ as the new $\boldsymbol{x}_{0.j}$ and $\boldsymbol{v}_{0,j}$. The accelerations at the next step, $\boldsymbol{a}_{0,j}$ and $\dot{\boldsymbol{a}}_{0,j}$, are obtained by replacing $\boldsymbol{x}_{jk}$ and $\boldsymbol{v}_{jk}$ in Equations (4.3) and (4.4) with $\boldsymbol{x}_{jk} \equiv \boldsymbol{x}_{\mathrm{c},j} - \boldsymbol{x}_{\mathrm{c},k}$ and $\boldsymbol{v}_{jk} \equiv \boldsymbol{v}_{\mathrm{c},j} - \boldsymbol{v}_{\mathrm{c},k}$. The time step Δt_j appropriate for particle j is empirically chosen as

$$\Delta t_j = \eta \sqrt{\frac{|\boldsymbol{a}_{1,j}||\boldsymbol{a}^{(2)}_{1,j}| + |\dot{\boldsymbol{a}}_{1,j}|^2}{|\dot{\boldsymbol{a}}_{1,j}||\boldsymbol{a}^{(3)}_{1,j}| + |\boldsymbol{a}^{(2)}_{1,j}|^2}}, \tag{4.13}$$

where η is a parameter that controls the accuracy of integration (Aarseth 1985). The values of $\boldsymbol{a}^{(2)}_{1,j}$ and $\boldsymbol{a}^{(3)}_{1,j}$ can be evaluated by $\boldsymbol{a}^{(2)}_{1,j} = \boldsymbol{a}^{(2)}_{0,j} + \Delta t \boldsymbol{a}^{(3)}_{0,j}$ and $\boldsymbol{a}^{(3)}_{1,j} = \boldsymbol{a}^{(3)}_{0,j}$, which are accurate to $\mathcal{O}(\Delta t^3)$. In this thesis, we choose the minimum value of Δt_j for all j as the time step for all the particles (*shared time step*). This method, however, becomes very inefficient when the simulation involves frequent close encounters of the particles. Other schemes including *individual timestep* or *hierarchical timestep* are required in such cases. Also note that $\boldsymbol{a}^{(2)}_{0,j}$ and $\boldsymbol{a}^{(3)}_{0,j}$ cannot be evaluated at the beginning of integration ($t = 0$). In this case, we use Equations (4.3) and (4.4) to calculate $\boldsymbol{a}_{0,j}$ and $\dot{\boldsymbol{a}}_{0,j}$, and choose

$$\Delta t_j = \eta \frac{|\boldsymbol{a}_{0,j}|}{|\dot{\boldsymbol{a}}_{0,j}|}. \tag{4.14}$$

This choice assures that the last terms in Equations (4.1) and (4.2) are much smaller than the second-last terms, which is necessary for the predictors to have $\mathcal{O}(\Delta t^2)$ precisions.

4.1.2 Advantages of the Fourth-order Hermite Scheme

In addition to is precision, the fourth-order Hermite scheme described above have several practical advantages. Unlike in ordinary implicit methods, we can start integration at any given time, without the past information of the system. Besides, use of predictors allow us to integrate the orbits of the particles with different time steps so that the particles experiencing close encounters should not slow down the calculations for the other particles that do not require such small time steps.

Furthermore, this integrator is time symmetric; such integrators are known to have no secular energy error in integrating a periodic orbit (Quinlan and Tremaine 1990; Cano and Sanz-Serna 1997). The time symmetry can be seen explicitly by substituting $\boldsymbol{a}^{(2)}_{0,j}$ and $\boldsymbol{a}^{(3)}_{0,j}$ in Equations (4.8) and (4.9) into the Taylor expansion of $\boldsymbol{x}_{1,j} \equiv \boldsymbol{x}_j(t_0 + \Delta t)$ and $\boldsymbol{v}_{1,j} \equiv \boldsymbol{v}_j(t_0 + \Delta t)$. The resulting expressions are

$$\boldsymbol{x}_{1,j} = \boldsymbol{x}_{0,j} + \frac{1}{2}(\boldsymbol{v}_{1,j} + \boldsymbol{v}_{0,j})\Delta t - \frac{\alpha}{10}(\boldsymbol{a}_{1,j} - \boldsymbol{a}_{0,j})\Delta t^2 + \frac{6\alpha - 5}{120}(\dot{\boldsymbol{a}}_{1,j} + \dot{\boldsymbol{a}}_{0,j})\Delta t^3, \tag{4.15}$$

$$\boldsymbol{v}_{1,j} = \boldsymbol{v}_{0,j} + \frac{1}{2}(\boldsymbol{a}_{1,j} + \boldsymbol{a}_{0,j})\Delta t - \frac{1}{12}(\boldsymbol{a}_{1,j} - \boldsymbol{a}_{0,j})\Delta t^2, \tag{4.16}$$

which are symmetric under the transformation $\Delta t \leftrightarrow -\Delta t$ and $0 \leftrightarrow 1$.

4.2 Bayesian Analysis using Markov Chain Monte Carlo[4]

4.2.1 Description of the Method

Bayesian Inference

Suppose that we have a joint probability distribution $p(x, y)$, where x and y are scalars or vectors. From this $p(x, y)$, we define a marginalized probability distribution for x, $p(x) \equiv \int p(x, y)\mathrm{d}y$. Using these distributions, *Bayes' theorem* can be written as

$$p(y|x) = \frac{p(x, y)}{p(x)} = \frac{p(y)p(x|y)}{\int p(x, y)\mathrm{d}y}. \tag{4.17}$$

Here $p(y|x)$ is a conditional probability distribution of y, given that the value x has been obtained, and similarly for $p(x|y)$.

In Bayesian inference, x is identified as a set of observational data $\boldsymbol{d}$ and y as a set of model parameters $\boldsymbol{\theta}$ that are not directly observed. Then, the above theorem yields a *posterior probability distribution* $p(\boldsymbol{\theta}|\boldsymbol{d})$, which represents our knowledge on $\boldsymbol{\theta}$ gained by the observations $\boldsymbol{d}$. In this case, therefore, what we need to calculate is the right-hand side of

$$p(\boldsymbol{\theta}|\boldsymbol{d}) = \frac{p(\boldsymbol{d}, \boldsymbol{\theta})}{\int p(\boldsymbol{d}, \boldsymbol{\theta})\mathrm{d}\boldsymbol{\theta}} = \frac{p(\boldsymbol{\theta})p(\boldsymbol{d}|\boldsymbol{\theta})}{\int p(\boldsymbol{d}, \boldsymbol{\theta})\mathrm{d}\boldsymbol{\theta}}. \tag{4.18}$$

However, the integral in the denominator is difficult to calculate, especially when the model parameters $\boldsymbol{\theta}$ have a large number of dimensions. The *Markov chain Monte Carlo* (MCMC) method described in this section provides an efficient way of evaluating this (and other necessary) integral.

Goal and Theoretical Foundation of the MCMC method

The goal of the MCMC method is to construct a chain of sets of model parameters $\boldsymbol{\theta}_n$ sampled from the posterior probability distribution $p(\boldsymbol{\theta}|\boldsymbol{d})$ that we need. We generate such a chain by specifying an initial set of parameters $\boldsymbol{\theta}_0$ and a transition probability from set n to $n + 1$, $p_{\mathrm{tr}}(\boldsymbol{\theta}_{n+1}|\boldsymbol{\theta}_n)$. This represents the Markov property of this method, where the transition probability depends only on the current state.

It is, of course, not at all obvious that such a chain has the desired probability. However, it has been shown that the chain does converge to the posterior probability distribution if the Markov chain satisfies the following conditions:

1. The chain is aperiodic.
2. The chain is irreducible, *i.e.*, every state with non-zero probability can be reached from any other state with non-zero probability.
3. The chain is reversible, *i.e.*, it satisfies the *detailed balance equation*

$$p(\boldsymbol{\theta}|\boldsymbol{d})p_{\mathrm{tr}}(\boldsymbol{\theta}'|\boldsymbol{\theta}) = p(\boldsymbol{\theta}'|\boldsymbol{d})p_{\mathrm{tr}}(\boldsymbol{\theta}|\boldsymbol{\theta}'). \tag{4.19}$$

[4]This section is based on Ford (2005, 2006), and Press et al. (2007).

We can understand what the condition (4.19) implies, by integrating both sides of this relation with respect to $\boldsymbol{\theta}$:

$$\int p_{\rm tr}(\boldsymbol{\theta}'|\boldsymbol{\theta})p(\boldsymbol{\theta}|\boldsymbol{d})\mathrm{d}\boldsymbol{\theta} = p(\boldsymbol{\theta}'|\boldsymbol{d})\int p_{\rm tr}(\boldsymbol{\theta}|\boldsymbol{\theta}')\mathrm{d}\boldsymbol{\theta} = \frac{p(\boldsymbol{\theta}'|\boldsymbol{d})}{p_{\rm tr}(\boldsymbol{\theta}')}\int p_{\rm tr}(\boldsymbol{\theta},\boldsymbol{\theta}')\mathrm{d}\boldsymbol{\theta} = p(\boldsymbol{\theta}'|\boldsymbol{d}), \quad (4.20)$$

where we use the definition of the marginalized probability distribution $p(\boldsymbol{\theta}')_{\rm tr} \equiv \int p_{\rm tr}(\boldsymbol{\theta},\boldsymbol{\theta}')\mathrm{d}\boldsymbol{\theta}$ in the last equality. Here the left-hand side of Equation (4.20) represents the probability that we get $\boldsymbol{\theta}'$ in the chain. Thus, Equation (4.20) shows that if $\boldsymbol{\theta}$ is sampled from the desired posterior distribution $p(\boldsymbol{\theta}|\boldsymbol{d})$, so is $\boldsymbol{\theta}'$: in other words, $p(\boldsymbol{\theta}|\boldsymbol{d})$ is a steady-state distribution for every $\boldsymbol{\theta} = \boldsymbol{\theta}_n$.

In the remaining of this subsection, we discuss how to construct the transition probability $p_{\rm tr}(\boldsymbol{\theta}'|\boldsymbol{\theta})$ that satisfies the above three conditions.

Metropolis-Hasting Algorithm

A reversible transition probability $p_{\rm tr}(\boldsymbol{\theta}'|\boldsymbol{\theta})$ can be constructed from a *non-reversible* candidate transition probability $q(\boldsymbol{\theta}'|\boldsymbol{\theta})$ according to the following procedure. This is called the *Metropolis-Hasting algorithm*.

First, we choose a trial state $\boldsymbol{\theta}_{\rm c}$ using $q(\boldsymbol{\theta}_{\rm c}|\boldsymbol{\theta})$. Then, we randomly accept or reject the state as the next step based on the *acceptance probability* defined as

$$\begin{aligned}\alpha(\boldsymbol{\theta}_{\rm c}|\boldsymbol{\theta}) &= \min\left[\frac{p(\boldsymbol{\theta}_{\rm c}|\boldsymbol{d})q(\boldsymbol{\theta}|\boldsymbol{\theta}_{\rm c})}{p(\boldsymbol{\theta}|\boldsymbol{d})q(\boldsymbol{\theta}_{\rm c}|\boldsymbol{\theta})}, 1\right] \\ &= \min\left[\frac{p(\boldsymbol{d}|\boldsymbol{\theta}_{\rm c})p(\boldsymbol{\theta}_{\rm c})q(\boldsymbol{\theta}|\boldsymbol{\theta}_{\rm c})}{p(\boldsymbol{d}|\boldsymbol{\theta})p(\boldsymbol{\theta})q(\boldsymbol{\theta}_{\rm c}|\boldsymbol{\theta})}, 1\right]. \end{aligned} \quad (4.21)$$

If the trial state is accepted, we set $\boldsymbol{\theta}' = \boldsymbol{\theta}_{\rm c}$; otherwise, we leave $\boldsymbol{\theta}$ unchanged (that is, $\boldsymbol{\theta}' = \boldsymbol{\theta}$). The transition probability constructed in this way,

$$p_{\rm tr}(\boldsymbol{\theta}'|\boldsymbol{\theta}) = q(\boldsymbol{\theta}'|\boldsymbol{\theta})\alpha(\boldsymbol{\theta}'|\boldsymbol{\theta}), \quad (4.22)$$

satisfies the above three conditions, provided that $q(\boldsymbol{\theta}'|\boldsymbol{\theta})$ allows the transition to all $\boldsymbol{\theta}'$ for which $p(\boldsymbol{\theta}'|\boldsymbol{d}) \neq 0$. We can check the detailed balance equation (4.19) by multiplying both sides of $\alpha(\boldsymbol{\theta}'|\boldsymbol{\theta})$ by $p(\boldsymbol{\theta}|\boldsymbol{d})q(\boldsymbol{\theta}'|\boldsymbol{\theta})$:

$$\min\left[p(\boldsymbol{\theta}'|\boldsymbol{d})q(\boldsymbol{\theta}|\boldsymbol{\theta}'), p(\boldsymbol{\theta}|\boldsymbol{d})q(\boldsymbol{\theta}'|\boldsymbol{\theta})\right] = p(\boldsymbol{\theta}|\boldsymbol{d})q(\boldsymbol{\theta}'|\boldsymbol{\theta})\alpha(\boldsymbol{\theta}'|\boldsymbol{\theta}) = p(\boldsymbol{\theta}|\boldsymbol{d})p_{\rm tr}(\boldsymbol{\theta}'|\boldsymbol{\theta}). \quad (4.23)$$

The left-hand side of Equation (4.23) is apparently invariant with respect to the exchange of $\boldsymbol{\theta}$ and $\boldsymbol{\theta}'$, and so is the right-hand side, $p(\boldsymbol{\theta}|\boldsymbol{d})p_{\rm tr}(\boldsymbol{\theta}'|\boldsymbol{\theta})$. Thus, Equation (4.23) implies the detailed balance equation (4.19). Note that this algorithm does not require a priori knowledge about the normalization of $p(\boldsymbol{\theta}|\boldsymbol{d})$. Also note that the transition probability (4.22) only guarantees the convergence, but does not tell us when it is achieved.

Assuming that the observational errors $\boldsymbol{\sigma}$ are Gaussian and uncorrelated, the probability that we obtain data $\boldsymbol{d}$ from a set of model parameters $\boldsymbol{\theta}$ is given by

$$p(\boldsymbol{d}|\boldsymbol{\theta}) \propto \prod_i \exp\left(-\frac{1}{2}\left[\frac{d_i - d_{{\rm model},i}(\boldsymbol{\theta})}{\sigma_i}\right]^2\right) = \exp\left[-\frac{\chi^2(\boldsymbol{\theta})}{2}\right], \quad (4.24)$$

where i is the label of each data point, $\boldsymbol{d}_{\rm model}$ denotes a set of observed quantities obtained from the model parameters $\boldsymbol{\theta}$, and

$$\chi^2(\boldsymbol{\theta}) \equiv \sum_i \left[\frac{d_i - d_{{\rm model},i}(\boldsymbol{\theta})}{\sigma_i}\right]^2 \tag{4.25}$$

is the value of chi-squared obtained from the model. If we also choose a uniform prior in $\boldsymbol{\theta}$ (*i.e.*, $p(\boldsymbol{\theta}) \sim 1$), we obtain

$$\frac{p(\boldsymbol{d}|\boldsymbol{\theta}')p(\boldsymbol{\theta}')q(\boldsymbol{\theta}|\boldsymbol{\theta}')}{p(\boldsymbol{d}|\boldsymbol{\theta})p(\boldsymbol{\theta})q(\boldsymbol{\theta}'|\boldsymbol{\theta})} = \frac{q(\boldsymbol{\theta}|\boldsymbol{\theta}')}{q(\boldsymbol{\theta}'|\boldsymbol{\theta})} \exp\left[-\frac{\chi^2(\boldsymbol{\theta}') - \chi^2(\boldsymbol{\theta})}{2}\right] \tag{4.26}$$

in Equation (4.21). Thus, the only remaining issue is how to choose $q(\boldsymbol{\theta}'|\boldsymbol{\theta})$ (and the computation of $p(\boldsymbol{\theta}')/p(\boldsymbol{\theta})$, in the case that we choose the priors that are not uniform in $\boldsymbol{\theta}$; see Section 4.2.2).

Metropolis-Hasting Algorithm within the Gibbs Sampler

An ideal way to sample the trial state $\boldsymbol{\theta}'$ is just to choose $q(\boldsymbol{\theta}'|\boldsymbol{\theta}) = p(\boldsymbol{\theta}'|\boldsymbol{d})$, in which case the acceptance probability calculated from Equation (4.21) is always unity and each state is indeed drawn from the desired posterior probability distribution $p(\boldsymbol{\theta}|\boldsymbol{d})$. This is, however, of course impossible for our application, because $p(\boldsymbol{\theta}|\boldsymbol{d})$ is exactly what we are seeking for. For this reason, it is common to use a special case of the Metropolis-Hasting algorithm, known as the Metropolis-Hasting algorithm within the *Gibbs sampler*.

The Gibbs sampler itself is a more general concept than the Metropolis-Hasting algorithm. In this algorithm, a trial state $\boldsymbol{\theta}'$ is generated by altering only a subset of $\boldsymbol{\theta}$ at each step. We first divide $\boldsymbol{\theta}$ into d components $\boldsymbol{\theta} = (\theta_1, \theta_2, \cdots, \theta_d)$, and choose their ordering, say, by random permutation. Then, for each component θ_μ, we sample a new value of θ'_μ from the conditional probability distribution

$$p(\theta_\mu|\boldsymbol{\theta}^{-\mu}, \boldsymbol{d}) \equiv p(\theta_\mu|\theta_1, \cdots, \theta_{\mu-1}, \theta_{\mu+1}, \cdots, \theta_d, \boldsymbol{d}), \tag{4.27}$$

and proceed to the next component iteratively. This scheme is especially useful in handling multidimensional parameter spaces, where it is often difficult to construct an appropriate $p_{\rm tr}(\boldsymbol{\theta}'|\boldsymbol{\theta})$ by updating all the parameters simultaneously. For such a "vector jump" to be possible, we need to have good guesses for the scale of the distribution for each component, as well as proper treatment of the correlations that may exist between some of the components; otherwise, the acceptance probability calculated from Equation (4.21) may become too low, and we never reach the next step. Of course, we need to adjust the scaling parameters even in the Gibbs sampler, but in this case we can easily monitor the acceptance probability of each parameter, which makes it relatively easy to fix the problem.

Here we modify the general form of the Gibbs sampler described above, taking into account that we cannot use $p(\boldsymbol{\theta}|\boldsymbol{d})$ to determine a transition probability. Namely, we approximately adopt a Gaussian form of $q(\theta'_\mu|\theta_\mu)$,[5]

$$q(\theta'_\mu|\theta_\mu) = \frac{1}{\sqrt{2\pi\beta_\mu^2}} \exp\left[-\frac{(\theta'_\mu - \theta_\mu)^2}{2\beta_\mu^2}\right], \tag{4.28}$$

[5]Strictly speaking, this $q(\theta'_\mu|\theta_\mu)$ may have to be written as $q(\theta'_\mu|\theta_\mu, \boldsymbol{\theta}^{-\mu})$.

for valid θ'_μ (see Section 4.2.2), and calculate $p_{\rm tr}(\boldsymbol{\theta}'|\boldsymbol{\theta})$ according to Equation (4.22). Here $\boldsymbol{\beta}$ is a set of parameters that controls the "step size" of each transition, and μ indicates each component. We (somewhat empirically) adjust the value of $\boldsymbol{\beta}$ so that the acceptance probability in Equation (4.21) becomes an optimal value. If the value of β is too large, the value of α becomes so small that the parameter space is not searched efficiently; on the other hand, if β is too small, we have the same problem even for α close to unity. The optimal acceptance probability is ~ 0.44 in one dimension, and declines to ~ 0.23 when several parameters are updated at once in high ($d \gtrsim 5$) dimensions (Gelman et al. 2003).

The candidate transition probability in Equation (4.28) has the property $q(\theta'_\mu|\theta_\mu) = q(\theta_\mu|\theta'_\mu)$. In this case, therefore, the acceptance probability given by Equations (4.21) and (4.26) reduces to

$$\alpha(\boldsymbol{\theta}'|\boldsymbol{\theta}) = \min\left\{\exp\left[\frac{\chi^2(\boldsymbol{\theta}) - \chi^2(\boldsymbol{\theta}')}{2}\right], 1\right\}. \tag{4.29}$$

Note that $\boldsymbol{\theta}'$ and $\boldsymbol{\theta}$ are different in only one component.

4.2.2 Technical Issues in Fitting Planetary Orbits

Choice of Priors

A common situation in performing the MCMC analysis is that the range of model parameters is (i) confined to some region by definition or (ii) already constrained from other observations. Here we briefly describe how to cope with these two situations.

As an example of case (i), let us consider the orbital period of a planet P, which should be always positive. In this case, $p(\boldsymbol{\theta}) = 0$ for $P < 0$, and $p(\boldsymbol{\theta}) = 1$ otherwise.[6] Using Equation (4.21), this condition is equivalent to choose $\alpha(\boldsymbol{\theta}'|\boldsymbol{\theta}) = 0$ for $\boldsymbol{\theta}'$ that includes negative P. Thus, we can properly take account of this situation by rejecting the trial state $\boldsymbol{\theta}'$ that includes invalid values of the parameters. An alternative procedure is to choose $\ln P$ as the model parameter instead, and assume the prior probability distribution uniform in $\ln P$. This prescription is effective when there is a large range of possible orbital periods, because it results in larger steps at longer periods and smaller steps at shorter periods.

The situation described in case (ii) often occurs in fitting the transit light curve for the stellar density, $\rho_\star$, using an MCMC algorithm (see Section 2.4.1). If the spectroscopic observations have already been performed for the central star, we would have some estimates for the stellar mass and radius, which are combined to constrain $\rho_\star$. It is often useful to incorporate such "prior" information into the MCMC fit for more accurate determination of the transit parameters.

Suppose the constraint from the spectroscopy is given by a Gaussian with its central value $\rho_\star^{\rm p}$ and width $\delta\rho_\star^{\rm p}$. Then the ratio of the prior probability distributions in Equation (4.21) is given by

$$\frac{p(\boldsymbol{\theta}')}{p(\boldsymbol{\theta})} = \frac{\exp\left[-(\rho'_\star - \rho_\star^{\rm p})^2/2(\delta\rho_\star^{\rm p})^2\right]}{\exp\left[-(\rho_\star - \rho_\star^{\rm p})^2/2(\delta\rho_\star^{\rm p})^2\right]}, \tag{4.30}$$

[6] There may exist more realistic limit (*e.g.*, the orbital period corresponding to the Roche limit), but the different choice of the lower (or upper) bound does not alter the procedure described below.

assuming that $\rho_\star$ is independent from the other parameters in the joint prior probability distribution $p(\boldsymbol{\theta})$ and that $p(\theta_\mu) \sim 1$ for θ_μ other than $\rho_\star$. Thus, the same arguments leading to Equation (4.29) yield $\alpha(\boldsymbol{\theta'}|\boldsymbol{\theta})$ in this case as

$$\alpha(\boldsymbol{\theta'}|\boldsymbol{\theta}) = \min\left\{\exp\left[\frac{\tilde{\chi}^2(\boldsymbol{\theta}) - \tilde{\chi}^2(\boldsymbol{\theta'})}{2}\right], 1\right\}, \tag{4.31}$$

where

$$\tilde{\chi}^2(\boldsymbol{\theta}) \equiv \chi^2(\boldsymbol{\theta}) + \left(\frac{\rho_\star - \rho_\star^{\rm p}}{\delta\rho_\star^{\rm p}}\right)^2. \tag{4.32}$$

Equation (4.31) shows that the prior information given by a Gaussian can be taken into account simply by adding the term in Equation (4.32) to the usual χ^2. Generalization to non-Gaussian priors is straightforward: we calculate the ratio in Equation (4.30), and multiply the first term in the square bracket in Equation (4.29), or Equation (4.21), if the observational errors are not assumed to be Gaussian, by this factor.

Taking Steps in Different Sets of Parameters

In Section 4.2.1, we described how to "take steps" (choose the next state in the chain) in the model parameters $\boldsymbol{\theta}$; see Equations (4.22) and (4.28). However, it often makes the convergence of the Markov chain faster to take steps in different combinations of the model parameters.

Let us consider the case where we fit $\boldsymbol{\theta} = (e, \omega)$ for example. For low-eccentricity orbits, the constraint on ω is usually weak, because ω is not well defined at $e = 0$. If we take steps in e and ω in such a case, the Markov chain has to search a broad range of ω in $[0, 2\pi]$, which reduces the efficiency of the MCMC analysis. This issue can be addressed by using the variables $e\cos\omega$ and $e\sin\omega$ instead, since the Markov chain can jump to an arbitrary value of ω in a smaller number of steps.

In this approach, we should also pay attention to the form of the prior probability distribution assumed; if we just use $\boldsymbol{\theta} = (e\cos\omega, e\sin\omega)$ in the above formulation (Section 4.2.1), this is equivalent to assuming the priors *uniform in* $e\cos\omega$ *and* $e\sin\omega$. This choice corresponds to $p(e) \sim e$, as can be seen geometrically. Therefore, to keep using the prior uniform in e, we need to modify Equation (4.29) as

$$\begin{aligned}&\alpha(e'\cos\omega', e'\sin\omega'|e\cos\omega, e\sin\omega)\\ &= \min\left\{\frac{e}{e'}\exp\left[\frac{\chi^2(e\cos\omega, e\sin\omega) - \chi^2(e'\cos\omega', e'\sin\omega')}{2}\right], 1\right\}.\end{aligned} \tag{4.33}$$

This modification corresponds to choosing

$$p(e\cos\omega, e\sin\omega) = \frac{1}{2\pi} \times \frac{1}{\sqrt{(e\cos\omega)^2 + (e\sin\omega)^2}}, \tag{4.34}$$

which indeed leads to the uniform $p(e, \omega)$:

$$p(e, \omega) = p(e\cos\omega, e\sin\omega)\frac{\partial(e\cos\omega, e\sin\omega)}{\partial(e, \omega)} = \frac{1}{2\pi}. \tag{4.35}$$

The situation described above can be formally generalized as follows. Suppose that we choose the prior probability distribution that is uniform in a set of model parameters denoted by $\boldsymbol{\theta}$, but take steps in a different set of parameters $\boldsymbol{u}(\boldsymbol{\theta})$. Since the choice of the candidate transition probability distribution is arbitrary (as long as it allows the transitions to all the states with non-zero probabilities), we use the same form of the probability distribution as given by Equation (4.28) for $\boldsymbol{u}$:

$$q(u_\mu(\boldsymbol{\theta}')|u_\mu(\boldsymbol{\theta})) = \frac{1}{\sqrt{2\pi\beta_\mu^2}} \exp\left[-\frac{(u_\mu(\boldsymbol{\theta}') - u_\mu(\boldsymbol{\theta}))^2}{2\beta_\mu^2}\right]. \tag{4.36}$$

Here β_μ controls the step sizes in $u_\mu(\boldsymbol{\theta})$, not in θ_μ. Also note that the probability distribution q in Equation (4.36) is defined with the measure $\mathrm{d}u_\mu$. In order to rewrite $q(\boldsymbol{u}'|\boldsymbol{u})$ as the probability distribution in $\boldsymbol{\theta}$ space, $\tilde{q}(\boldsymbol{\theta}'|\boldsymbol{\theta})$, we need to include the Jacobian of the transformation $\boldsymbol{u}(\boldsymbol{\theta})$. That is, $q(\boldsymbol{\theta}'|\boldsymbol{\theta})$ in Section 4.2.1 is replaced with

$$\tilde{q}(\boldsymbol{\theta}'|\boldsymbol{\theta}) = J(\boldsymbol{\theta}')q(\boldsymbol{u}(\boldsymbol{\theta}')|\boldsymbol{u}(\boldsymbol{\theta})), \tag{4.37}$$

where

$$J(\boldsymbol{\theta}) \equiv \left|\frac{\partial \boldsymbol{u}(\boldsymbol{\theta})}{\partial \boldsymbol{\theta}}\right|. \tag{4.38}$$

Thus, the ratio of q in Equation (4.26) is replaced with

$$\frac{\tilde{q}(\boldsymbol{\theta}|\boldsymbol{\theta}')}{\tilde{q}(\boldsymbol{\theta}'|\boldsymbol{\theta})} = \frac{J(\boldsymbol{\theta})q(\boldsymbol{u}(\boldsymbol{\theta})|\boldsymbol{u}(\boldsymbol{\theta}'))}{J(\boldsymbol{\theta}')q(\boldsymbol{u}(\boldsymbol{\theta}')|\boldsymbol{u}(\boldsymbol{\theta}))} = \frac{J(\boldsymbol{\theta})}{J(\boldsymbol{\theta}')}, \tag{4.39}$$

where we used $q(\boldsymbol{u}(\boldsymbol{\theta}')|\boldsymbol{u}(\boldsymbol{\theta})) = q(\boldsymbol{u}(\boldsymbol{\theta})|\boldsymbol{u}(\boldsymbol{\theta}'))$ in the last equality. Combining Equation (4.39) with Equations (4.21) and (4.26), we obtain

$$\alpha(\boldsymbol{\theta}'|\boldsymbol{\theta}) = \min\left\{\frac{J(\boldsymbol{\theta})}{J(\boldsymbol{\theta}')} \exp\left[\frac{\chi^2(\boldsymbol{\theta}) - \chi^2(\boldsymbol{\theta}')}{2}\right], 1\right\}. \tag{4.40}$$

In this formulation, the example we discussed above corresponds to the case where we choose $\boldsymbol{\theta} = (e, \omega)$ and $\boldsymbol{u}(\boldsymbol{\theta}) = (e\cos\omega, e\sin\omega)$, and assume the prior uniform in e and ω. Then, the Jacobian in Equation (4.38) is given by $J(\boldsymbol{\theta}) = e$, and so Equation (4.40) reduces to Equation (4.33). Various other choices of $\boldsymbol{\theta}$ and $\boldsymbol{u}(\boldsymbol{\theta})$ that improve the efficiency of the MCMC algorithm are discussed in Ford (2006).

Chapter 5

Characterization of the KOI-94 System with TTV Analysis and Implication for the Planet-Planet Eclipse[1]

5.1 Introduction

The Kepler Object of Interest (KOI) 94 system is a multi-transiting planetary system discovered by the *Kepler* space telescope (Borucki et al. 2011; Batalha et al. 2013), consisting of four transiting planets with periods of about 3.7 (KOI-94b), 10 (KOI-94c), 22 (KOI-94d), and 54 (KOI-94e) days (Figure 5.1). For the largest planet KOI-94d, Hirano et al. (2012a) observed the Rossiter-McLaughlin effect (Rossiter 1924; McLaughlin 1924; Queloz et al. 2000; Ohta et al. 2005; Winn et al. 2005; Hirano et al. 2011b, see also Section 2.4) for the first time in a multi-transiting system. They found $\lambda = -6^{+13}_{-11}\,\mathrm{deg}$, showing that the orbital axis of this planet is aligned with the stellar spin axis (this result was later confirmed by Albrecht et al. (2013), who obtained $\lambda = -11 \pm 11\,\mathrm{deg}$). Furthermore, the KOI-94 system is the first and only system in which a rare mutual event called a "planet-planet eclipse" (hereafter PPE) was identified; in this event, two planets transit simultaneously and partially overlap with each other on the stellar disk as seen from our line of sight. By analyzing the light curve of the PPE caused by KOI-94d and KOI-94e, Hirano et al. (2012a) concluded that the orbital planes of these two planets are also well aligned within 2 degrees. In this system, therefore, the stellar spin axis and the orbital axes of the two planets are all aligned. If their close-in orbits are due to planetary migration (*e.g.*, Lubow and Ida 2011), this result suggests that they have experienced a quiescent disk migration (Goldreich and Tremaine 1980) rather than processes that include gravitational perturbations either by planets (*e.g.*, Nagasawa et al. 2008; Wu and Lithwick 2011; Naoz et al. 2011) or stars (*e.g.*, Wu and Murray 2003). Other processes that tilt the stellar spin axis relative to orbital axes of planets (*e.g.*, Bate et al. 2010; Lai et al. 2011; Rogers et al. 2012; Batygin 2012) are also excluded, provided that the orbital planes of the multiple transiting planets trace the original protoplanetary disk from which they formed. For these reasons, the KOI-94 system is an important test bed that provides

[1]This chapter is based on Masuda et al. (2013).

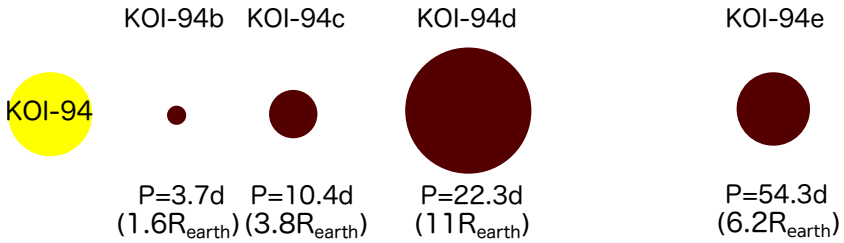

Figure 5.1 Schematic illustration of the KOI-94 system. Planetary radii are calculated from the planet-to-star radius ratio, stellar density obtained from the transit light curves, and spectroscopic stellar mass $M_\star = 1.25 M_\odot$ (Hirano et al. 2012a).

a clue to understand the formation process of closely-packed multi-transiting planetary systems, and hence deserves to be characterized in detail.

Recently, Weiss et al. (2013) measured the radial velocities (RVs) of KOI-94 from the W. M. Keck Observatory, and estimated the masses and eccentricities of the planets by a simultaneous fit to the observed RVs and the *Kepler* light curve. They showed that the masses of all the planets fall into the planetary regime, and especially obtained a fairly well constraint on the mass of KOI-94d ($m_\mathrm{d} = 106 \pm 11 M_\oplus$). However, the masses of KOI-94c ($m_\mathrm{c} = 15.6^{+5.7}_{-15.6} M_\oplus$) and KOI-94e ($m_\mathrm{e} = 35^{+18}_{-28} M_\oplus$) are weakly constrained because of the marginal detections of their RV signals. In addition, the best-fit eccentricity of KOI-94c ($e_\mathrm{c} = 0.43 \pm 0.23$) is suspiciously large in light of the long-term stability of the system, as pointed out in their paper. Hence additional RV observations are definitely important, but transit timing variations (TTVs, Holman and Murray 2005; Agol et al. 2005, see Chapter 3) can also be used to improve these estimates in a multi-transiting system like the KOI-94 system. Moreover, in the KOI-94 system, the orbital parameters are exceptionally well constrained by the observations of the Rossiter-McLaughlin effect and the PPE; this makes the KOI-94 system an ideal case to evaluate the reliability of the parameter estimates with TTVs in comparison to RVs.

Apart from such characterization of the KOI-94 system, the PPE itself is a unique phenomenon that is worth studying in a more general context. If this event is observed in the future transit observations, it can be used to precisely constrain the relative angular momentum of the planets, which is closely related to their orbital evolution processes. In fact, this phenomenon had been theoretically predicted before by Ragozzine and Holman (2010) (see also Rabus et al. 2009) as an "overlapping double transit," and they emphasized its role in constraining the relative nodal angle of the planets. However, neither the analytic formulation that clarifies the physical picture of this phenomenon, nor the discussion about how mutual gravitational interaction among the planets affects the PPE, has been presented so far.

In this chapter, we investigate the constraints on masses and eccentricities of KOI-94c, KOI-94d, and KOI-94e based on the direct numerical analysis of their TTV signals. We also construct an analytic model of the PPE, and discuss how the gravitational interaction affects the occurrence of the next PPE based on the model and the result of TTV analysis.

The plan of this chapter is as follows. First, we perform an intensive TTV analysis in Section 5.2. We discuss the constraints on transit parameters based on the phase-folded transit light curves, and those on the mass, eccentricity, and longitude of periastron based on the numerical fit to the observed TTV signals. Then in Section 5.3, we present an

Table 5.1. Definitions of the Parameters Derived in This Chapter

Parameter	Definition
Parameters derived from transit light curves	
t_0	Time of a transit center (BJD − 2454833)
P	Orbital period
$R_p/R_\star$	Planet-to-star radius ratio
$a/R_\star$	Scaled semi-major axis
b	Impact parameter of the transit ($= a\cos i/R_\star$, i: orbital inclination)
u_1, u_2	Coefficients for the quadratic limb-darkening law
Parameters derived from the PPE[1]	
Ω	Longitude of ascending node
Parameters derived from TTVs	
m	Planetary mass
e	Orbital eccentricity
$\varpi = \omega + \Omega$	Longitude of periastron

[1]PPE can only constrain the difference between the longitudes of ascending nodes of KOI-94d and KOI-94e. We have no information on that of KOI-94c.

analytic description of the PPE which elucidates how the height, duration, and central time of the brightening caused by the overlap are related to the orbital parameters. Based on this formulation, we provide a general procedure for constraining the orbits of the overlapping planets in Section 5.4. Here we also discuss a simple prediction of the next PPE on the basis of the two-body problem. Finally, based on the analytic model of the PPE and the result of TTV analysis, we show in Section 5.5 how the gravitational interaction among the planets affects the occurrence of the next PPE in the KOI-94 system, referring to the difference from the two-body prediction. Section 5.6 summarizes the chapter. The results on the properties of the KOI-94 system are all in Section 5.2, and so the readers who are only interested in the TTV analysis can skip Sections 5.3 to 5.5, where we mainly discuss the PPE.

5.2 Analysis of the Photometric Light Curves

In this section, we report the analysis of photometric light curves of KOI-94 taken by *Kepler*. We determine the orbital phases, scaled semi-major axes, scaled planetary radii, and inclinations of KOI-94c, KOI-94d, and KOI-94e from the phase-folded transit light curves, and estimate their masses, eccentricities, and longitudes of periastrons from their TTV signals (see Table 5.1). In the following analysis, we neglect the smallest and innermost planet KOI-94b, which does not affect the TTV signals of the other three, as we will see in Section 5.2.2.

Table 5.2. Parameter Values Estimated by Other Authors

Parameter	KOI-94c	KOI-94d	KOI-94e
Transit parameters determined by the Kepler team[1]			
t_0 (BJD − 2454833)	138.00718 ± 0.00093	132.74047 ± 0.00019	161.23998 ± 0.00079
P (days)	10.423707 ± 0.000026	22.343001 ± 0.000011	54.31993 ± 0.00012
$a/R_\star$	15.70 ± 0.37	26.10 ± 0.62	47.2 ± 1.1
$R_p/R_\star$	0.02544 ± 0.00012	0.06856 ± 0.00012	0.04058 ± 0.00013
b	0.019 ± 0.048	0.305 ± 0.014	0.387 ± 0.014
Parameters determined by Hirano et al. (2012a)			
Ω (deg)[2]	-6^{+13}_{-11}	···	-5^{+13}_{-11}
u_1		0.10 ± 0.06	
u_2		0.61 ± 0.08	
Parameters determined by Weiss et al. (2013)			
m ($M_\oplus$)	$15.6^{+5.7}_{-15.6}$	106 ± 11	35^{+18}_{-28}
e	0.43 ± 0.23	0.022 ± 0.038	0.019 ± 0.23

[1]Data from MAST archive `http://archive.stsci.edu/kepler/`

[2]In this chapter, we define the reference direction so that the spin-orbit angle λ measured by the Rossiter-McLaughlin effect be equal to Ω for the orbital inclination in the range $[0, \pi/2]$ (Fabrycky and Winn 2009). With this choice, the reference line points to the ascending node of a virtual circular orbit whose angular momentum is parallel to the stellar spin vector.

5.2.1 Transit Times and Transit Parameters

Data Processing

We analyze the short-cadence ($\sim$ 1 min) Pre-search Data Conditioned Simple Aperture Photometry (PDCSAP) fluxes (*e.g.*, Kinemuchi et al. 2012) from Quarters 4, 5, 8, 9, 12, and 13. We do not include the data from Quarter 1, for which only the long-cadence data is available. Since these light curves exhibit the long-term trends that affect the baseline of the transit, we remove those trends in the following manner. First, data points within ± 1 day of every transit caused by KOI-94c, KOI-94d, or KOI-94e are extracted and each set of the data is fitted with a fifth-order polynomial, masking out the points during the transit. Then we calculate the standard deviation of each fit, remove outliers exceeding 5σ, and fit the data again with the fifth-order polynomial. This process is iterated until all the 5σ outliers are removed. Finally, all the data points in each chunk (including those during the transit) are divided by the best-fit polynomial to yield a detrended and normalized transit light curve. In our analysis of the TTV, we exclude the transits whose ingress or egress is not completely observed due to the data cadence of *Kepler*. We also exclude the "double-transit" events, during which two planets transit the stellar disk at the same time. As an exception, the double transit of KOI-94d and KOI-94e around BJD = 2454211.5 (in which a PPE was observed) is included in our analysis; in this case the ingresses and egresses of both transits are clearly seen because of their close mid-transit times. The above criteria leave us with 44, 21, and 8 transits for KOI-94c, KOI-94d, and KOI-94e, respectively.

Transit Parameters

Before analyzing the TTV signals, we revise the transit parameters of KOI-94c, KOI-94d, and KOI-94e obtained by the Kepler team (Table 5.2) so that they are consistent with the light curves obtained in the above procedure. Here we first use the parameters publicized by the Kepler team to phase fold the observed transit light curves, and then refit those phase curves to obtain the revised transit parameters.

In the first step, we fit each of the detrended light curve centered at the transit (for ~ 1.7 times its duration) to obtain the times of transit centers t_c, using a Markov chain Monte Carlo (MCMC) algorithm (*c.f.*, Section 4.2). Here we use a light curve model by Ohta et al. (2009), and fix $a/R_\star$, $R_p/R_\star$, and b to the values obtained by the Kepler team, assuming $e = 0$. We model the limb darkening using a quadratic law:

$$\frac{I(\mu)}{I(0)} = 1 - u_1(1-\mu) - u_2(1-\mu)^2, \tag{5.1}$$

where $\mu = (1-r^2)^{1/2}$ and r is the radial coordinate on the stellar disk normalized to the stellar radius. We adopt the limb-darkening coefficients u_1 and u_2 obtained by Hirano et al. (2012a) (all these parameters are summarized in Table 5.2). Since the detrend procedure above can remove only the out-of-transit outliers, we also exclude in-transit 5σ outliers of this fit, if any, and fit the light curve again. Using the series of t_c obtained in this way, we construct the phase-folded transit light curve for each planet.

As the second step, we fit the resulting phase-folded transit light curves for $a/R_\star$, $R_p/R_\star$, b, u_1, and u_2 using the same light curve model as above. In this way, we obtain the revised values of the set of parameters shown in Table 5.3 and the corresponding

Table 5.3. Revised Transit Parameters Obtained from Phase-folded Light Curves

	KOI-94c	KOI-94d	KOI-94e
$a/R_\star$	$15.643^{+0.070}_{-0.151}$	$26.24^{+0.20}_{-0.19}$	$47.69^{+0.67}_{-0.64}$
$R_p/R_\star$	$0.025618^{+0.000097}_{-0.000093}$	$0.07029^{+0.00014}_{-0.00015}$	$0.04132^{+0.00016}_{-0.00018}$
b	$0.089^{+0.079}_{-0.064}$	$0.299^{+0.022}_{-0.025}$	$0.371^{+0.031}_{-0.036}$
u_1	0.35 ± 0.06	0.40 ± 0.02	0.36 ± 0.07
u_2	0.21 ± 0.11	0.14 ± 0.03	0.19 ± 0.10
χ^2/d.o.f	25843/23611	15473/13766	6827/5934

Note. — The quoted error bars denote 1σ confidence intervals obtained from the posterior distributions. The values of $a/R_\star$ and b for KOI-94c and KOI-94e are determined with the prior information about the stellar density based on the result for KOI-94d (see the main text).

best-fit light curves (Figures 5.2 to 5.4).[2] In this fit, all the parameters converge well in the case of KOI-94d. In contrast, $a/R_\star$ and b of KOI-94c and KOI-94e do not converge well moving back and forth between several local minima in a strongly correlated fashion, because they show smaller transit depths and the ingresses/egresses of their transits are less clear. For this reason, we impose an additional constraint that all the planets share the same host star: we convert the well-constrained $a/R_\star$ for KOI-94d into stellar density $\rho_\star$ via Equation (2.68), $\rho_\star \approx (3\pi/GP^2)(a/R_\star)^3$, and calculate the corresponding values and uncertainties of $a/R_\star$ for KOI-94c and KOI-94e. The phase curves of KOI-94c and KOI-94e are fitted with prior constraints centered on these values and with Gaussian widths of their uncertainties using the method described in Section 4.2.2. With this prescription, all the transit parameters of KOI-94c and KOI-94e converge well. Therefore, it does not make sense here to discuss the consistency of $\rho_\star$ calculated from the transit parameters to check the possible false positives. It is important to note, however, that the limb-darkening coefficients for each planet obtained individually are consistent within their 1σ error bars (those obtained by Hirano et al. (2012a) are different from our values because they fixed smaller $R_p/R_\star$ for KOI-94d; see Table 5.2). This supports the notion that these three planets are indeed revolving around the same host star.

[2]We also repeated the same analysis taking account of the quarter-to-quarter flux contaminations publicized by the *Kepler* team and available at MAST archive. As expected, we obtained larger R_p by a fraction of $\sim c/2$, where c is the fractional contamination (*e.g.*, Fabrycky et al. 2012), but the other parameters were consistent within 2.1σ except for a_c and a_e. These two parameters were different from those in Table 5.3 by $\sim 1\%$, corresponding to a slight change in the value of a_d. In this chapter, we do not apply this correction because the smaller values of R_p lead to more conservative estimates for the PPE occurrence.

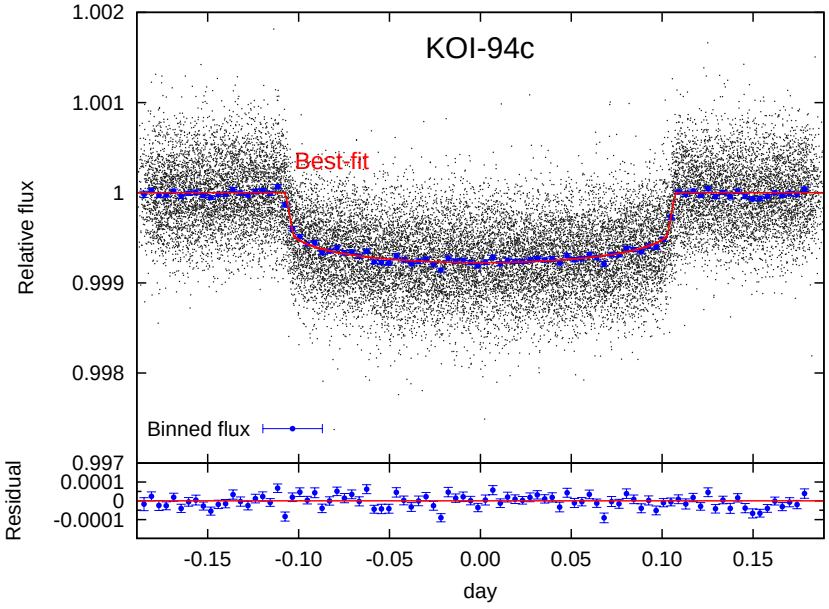

Figure 5.2 Phase-folded transit light curve of KOI-94c. The best-fit model is shown with the red solid line. Small gray dots are all the short-cadence data points. Blue points are fluxes binned to 0.1 hr bins and their error bars are calculated by 1.4826 × median absolute deviation.

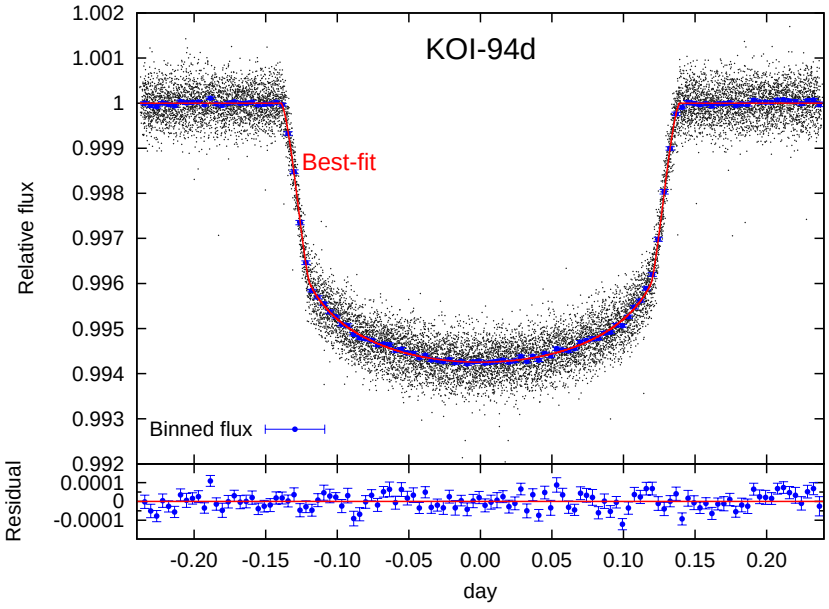

Figure 5.3 Phase-folded transit light curve of KOI-94d (same as Figure 5.2).

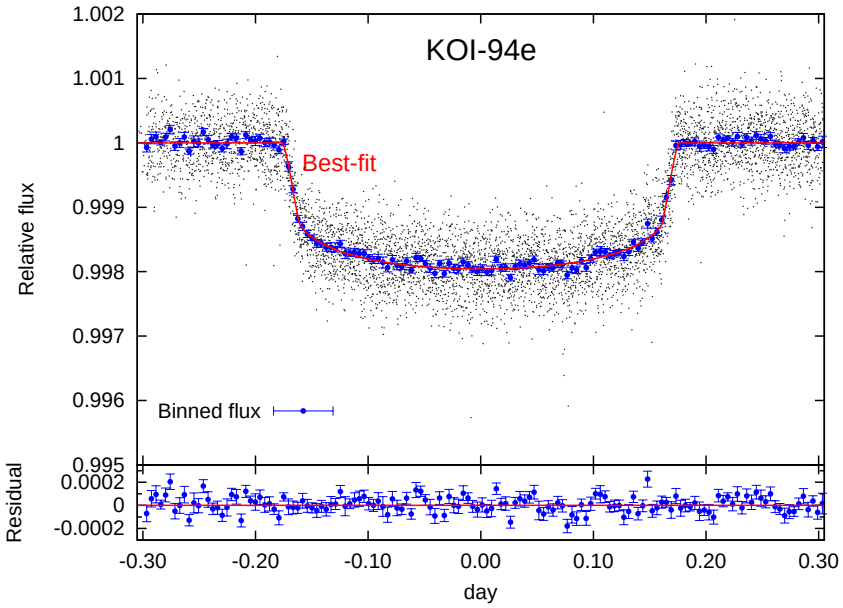

Figure 5.4 Phase-folded transit light curve of KOI-94e (same as Figure 5.2).

TTV Signals

Fixing $a/R_\star$, $R_p/R_\star$, b, u_1, and u_2 at the values in Table 5.3, we refit the transit light curves of each planet to find the values of t_c given in Tables 5.4 to 5.6, with the values of reduced χ^2 and 1σ upper/lower limits obtained from the posterior. The column labeled as $O-C$ tabulates the residuals of a linear fit to t_c versus transit number, in which linear ephemerides in Table 5.7 are extracted. The values of reduced χ^2 of the linear fits in this table indicate the significant deviations of the transit times from the linear ephemerides (*i.e.*, TTVs) for all the three planets, as shown in Figure 5.5. Note that the TTV of KOI-94c shows the sinusoidal modulation with the period of $(1/P_{\rm c} - 2/P_{\rm d})^{-1} \simeq 155\,{\rm days}$ (*c.f.*, Equation 3.75), which clearly comes from the proximity to the 2 : 1 resonance of KOI-94c and KOI-94d, as pointed out by Xie et al. (2013) (see also Appendix A).

Table 5.4. Transit Times of KOI-94c

Transit number	t_c (BJD − 2454833)	$1\sigma_{\rm lower}$	$1\sigma_{\rm upper}$	χ^2/d.o.f	$O-C$ (days)
21	356.90817	0.00102	0.00092	1.10	0.00245
22	367.33115	0.00110	0.00136	1.17	0.00174
23	377.75187	0.00142	0.00133	0.97	−0.00124
24	388.17539	0.00094	0.00086	1.15	−0.00140
26	409.02071	0.00231	0.00269	1.08	−0.00346
27	419.44211	0.00082	0.00085	1.02	−0.00575
28	429.86657	0.00197	0.00148	1.02	−0.00497
29	440.29072	0.00080	0.00087	1.24	−0.00452
30	450.71607	0.00120	0.00115	1.00	−0.00286
31	461.13894	0.00231	0.00170	1.10	−0.00368
32	471.56699	0.00124	0.00133	1.17	0.00069
33	481.99307	0.00072	0.00073	1.05	0.00308
34	492.41692	0.00116	0.00138	1.18	0.00324
35	502.84201	0.00107	0.00102	1.13	0.00464
36	513.26385	0.00101	0.00115	1.14	0.00279
37	523.68733	0.00101	0.00095	1.05	0.00259
38	534.10875	0.00100	0.00093	1.22	0.00032
58	742.57675	0.00088	0.00091	1.11	−0.00546
61	773.85373	0.00147	0.00122	1.17	0.00045
62	784.27831	0.00165	0.00115	1.17	0.00135
63	794.70489	0.00076	0.00085	1.13	0.00423
65	815.55087	0.00127	0.00128	1.10	0.00283
66	825.97556	0.00069	0.00072	0.94	0.00384
67	836.39887	0.00097	0.00114	1.01	0.00346
68	846.81847	0.00101	0.00126	1.13	−0.00063
69	857.24112	0.00111	0.00096	1.08	−0.00167
71	878.08547	0.00094	0.00089	1.09	−0.00469
72	888.51143	0.00146	0.00191	1.16	−0.00243
73	898.93547	0.00092	0.00087	1.07	−0.00207
93	1107.41537	0.00097	0.00127	1.01	0.00405
95	1128.26345	0.00112	0.00145	1.11	0.00475
96	1138.68565	0.00111	0.00091	1.06	0.00326
97	1149.10740	0.00118	0.00121	0.94	0.00133
98	1159.52802	0.00122	0.00116	1.02	−0.00174
99	1169.95296	0.00095	0.00108	1.10	−0.00049
100	1180.37319	0.00136	0.00161	1.00	−0.00395
101	1190.79857	0.00119	0.00116	1.14	−0.00226
102	1201.21882	0.00100	0.00119	1.19	−0.00570
103	1211.64373	0.00122	0.00119	1.06	−0.00448
104	1222.06922	0.00076	0.00073	1.17	−0.00268
105	1232.49526	0.00147	0.00137	1.29	−0.00032
106	1242.92076	0.00113	0.00132	0.96	0.00149

Table 5.4 (cont'd)

Transit number	t_c (BJD − 2454833)	$1\sigma_{\rm lower}$	$1\sigma_{\rm upper}$	χ^2/d.o.f	$O-C$ (days)
107	1253.34432	0.00091	0.00085	1.17	0.00136
108	1263.77117	0.00136	0.00095	1.17	0.00452

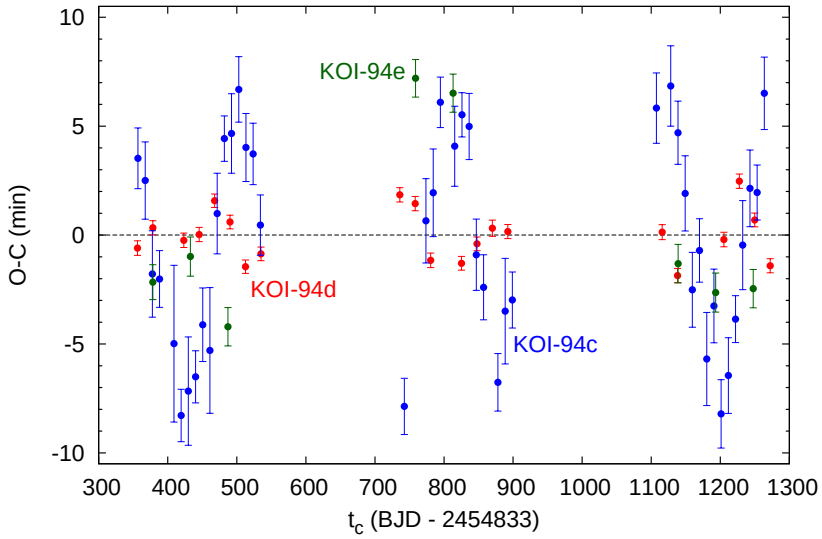

Figure 5.5 Observed TTV signals of KOI-94c (blue), KOI-94d (red), and KOI-94e (green).

5.2.2 Numerical Analysis of the TTV Signals Using RV Mass of KOI-94d

We numerically analyze the TTV signals in Figure 5.5 to constrain the masses, eccentricities, and longitudes of periastrons of KOI-94c, KOI-94d, and KOI-94e (nine parameters in total). In this section, we fix the mass of KOI-94d at $m_{\rm d} = 106 M_\oplus$, the best-fit RV value obtained by Weiss et al. (2013). Since this value is only marginally consistent with $m_{\rm d} = 73 \pm 25 M_\oplus$ obtained by Hirano et al. (2012a) based on the out-of-transit RVs taken by the Subaru telescope, we also investigate the case of $m_{\rm d} = 73 M_\oplus$ here.

Calculation of the Simulated TTV

Orbits of the planets are integrated using the fourth-order Hermite scheme with the shared time step (Kokubo and Makino 2004), as described in Section 4.1. The time step (typically ~ 0.025 days) is chosen so that the fractional energy change due to the integrator during ~ 1000 days integration should always be smaller than 10^{-9}. All the simulations presented in this section integrate planetary orbits beginning at the same epoch T_0(BJD) = 2455189.1703 (the first transit time of KOI-94d), until BJD = 2456133.0 (approximately the last transit time of KOI-94d we analyzed).

For each planet, the initial value of the orbital inclination i is fixed at the value obtained from $a/R_\star$ and b (see Table 5.3), assuming that $e = 0$. Here, all the i values

Table 5.5. Transit Times of KOI-94d

Transit number	t_c (BJD − 2454833)	$1\sigma_{\rm lower}$	$1\sigma_{\rm upper}$	χ^2/d.o.f	$O-C$ (days)
10	356.17032	0.00023	0.00023	1.10	−0.00041
11	378.51394[1]	0.00023	0.00023	1.25	0.00023
13	423.19948	0.00023	0.00023	1.17	−0.00017
14	445.54263	0.00022	0.00023	1.14	0.00002
15	467.88668	0.00021	0.00022	1.06	0.00109
16	490.22897	0.00022	0.00022	1.07	0.00042
17	512.57051	0.00021	0.00021	1.17	−0.00101
18	534.91389	0.00022	0.00022	1.08	−0.00060
27	736.00250	0.00023	0.00023	1.00	0.00128
28	758.34519	0.00023	0.00023	1.10	0.00100
29	780.68635	0.00023	0.00023	1.13	−0.00080
31	825.37220	0.00022	0.00022	1.06	−0.00090
32	847.71579	0.00022	0.00022	1.14	−0.00028
33	870.05926	0.00026	0.00026	1.03	0.00022
34	892.40212	0.00022	0.00022	1.11	0.00011
44	1115.83180	0.00024	0.00024	2.02	0.00009
45	1138.17339	0.00023	0.00023	1.10	−0.00129
48	1205.20344	0.00023	0.00023	1.11	−0.00014
49	1227.54827	0.00022	0.00023	1.01	0.00172
50	1249.89001	0.00022	0.00022	1.08	0.00048
51	1272.23152	0.00022	0.00023	0.94	−0.00098

[1]Double transit with KOI-94e: obtained simultaneously with the relative nodal angle and t_c for KOI-94e.

Table 5.6. Transit Times of KOI-94e

Transit number	t_c (BJD − 2454833)	$1\sigma_{\rm lower}$	$1\sigma_{\rm upper}$	χ^2/d.o.f	$O-C$ (days)
4	378.51677[1]	0.00056	0.00055	1.25	−0.00150
5	432.83744	0.00062	0.00063	1.22	−0.00068
6	487.15505	0.00060	0.00062	1.11	−0.00292
11	758.76221	0.00059	0.00060	0.98	0.00500
12	813.08158	0.00061	0.00061	1.10	0.00452
18	1138.99524	0.00060	0.00062	1.21	−0.00091
19	1193.31417	0.00062	0.00063	1.19	−0.00183
20	1247.63414	0.00060	0.00062	1.24	−0.00171

[1]Double transit with KOI-94d: obtained simultaneously with the relative nodal angle and t_c for KOI-94d.

Table 5.7. Lineaer Ephemerides of KOI-94c, KOI-94d, and KOI-94e

Parameter	KOI-94c	KOI-94d	KOI-94e
t_0 (BJD − 2454833)	138.00826 ± 0.00038	132.74103 ± 0.00012	161.23888 ± 0.00046
P (days)	10.4236888 ± 0.0000053	22.3429698 ± 0.0000036	54.319849 ± 0.000035
χ^2/d.o.f	10.4	13.7	29.2

are chosen in the range $[0, \pi/2]$.[3] The values of $\Omega_{\rm d}$ and $\Omega_{\rm e}$ are fixed at those in Table 5.2. Since we have no information on the nodal angle of KOI-94c, we assume $\Omega_{\rm c} = 0$ deg. Initial semi-major axes are calculated via Kepler's third law with $M_\star = 1.25 M_\odot$ (Hirano et al. 2012a), orbital periods in Table 5.7, and planetary masses adopted in each simulation. The phases of the planets are determined from the transit ephemerides: for each planet, we convert the transit time closest to T_0 into the sum of the argument of periastron and true anomaly $\omega + f$, taking account of the non-zero eccentricity if any, and then move it backward in time to T_0, assuming a Keplerian orbit.

The mid-transit times of each planet are determined by minimizing the sky-plane distance D between the star and the planet, where the roots of the time derivative of D are found by the Newton-Raphson method (Fabrycky 2010). Then these transit times are fitted with a straight line and thereby the TTVs (= residuals of the linear fit), as well as the linear ephemeris (P and t_0), are extracted. We compute the chi squares of the simulated TTVs obtained in this way as

$$\chi_j^2 = \sum_{\substack{i:\text{observed} \\ \text{transits}}} \left[\frac{\mathrm{TTV}_{\rm sim}^{(j)}(i) - \mathrm{TTV}_{\rm obs}^{(j)}(i)}{\sigma_{\rm obs}^{(j)}(i)} \right]^2, \quad (j = \mathrm{c}, \mathrm{d}, \mathrm{e}) \tag{5.2}$$

where $\mathrm{TTV}_{\rm sim}^{(j)}(i)$ and $\mathrm{TTV}_{\rm obs}^{(j)}(i)$ are the i-th values of simulated and observed TTVs of planet j, respectively, and $\sigma_{\rm obs}^{(j)}(i)$ is the observational uncertainty of the i-th transit time of planet j.

Note that we do not fit the transit times directly but only the *deviations* from the periodicity in our analysis, assuming that they provide sufficient information on the gravitational interaction among the planets. Indeed, although the initial values of semi-major axes are chosen to match the observed periods, periods derived from the simulations are different typically by ~ 0.01 days. This is because strong gravitational interaction among massive, closely-packed planets in this system causes the oscillations of their semi-major axes with amplitudes dependent on the parameters of the planets adopted in each run. We will show that this simplified method still yields reasonable results in the last part of Section 5.2.4.

[3] As we will see in Section 5.4, the observed PPE light curve requires that if we (arbitrarily) choose $i_{\rm d}$ in $[0, \pi/2]$, $i_{\rm e}$ is also in this range. There is no justification to choose $i_{\rm c}$ also in this range, but this choice does not affect the result significantly because the value of $i_{\rm c}$ is very close to $\pi/2$, as suggested by the small value of $b_{\rm c}$ (*c.f.*, Table 5.3)

Table 5.8. Semi-amplitude of the Simulated TTV (in Units of Minutes) for Each Planet Pair

TTV \ Pair	KOI-94b	KOI-94c	KOI-94d	KOI-94e	Major Parameters for TTV
KOI-94c	$\lesssim 0.05$	$\cdots$	11	$\lesssim 0.05$	$m_{\rm d}$, $\boldsymbol{e}_{\rm c}$, $\boldsymbol{e}_{\rm d}$
KOI-94d	$\lesssim 0.05$	0.47	$\cdots$	2.1	$m_{\rm c}$, $m_{\rm e}$, $\boldsymbol{e}_{\rm c}$, $\boldsymbol{e}_{\rm d}$, $\boldsymbol{e}_{\rm e}$
KOI-94e	$\lesssim 0.05$	0.15	0.83	$\cdots$	$m_{\rm d}$, $\boldsymbol{e}_{\rm d}$, $\boldsymbol{e}_{\rm e}$, ($m_{\rm c}$, $\boldsymbol{e}_{\rm c}$)

Estimates for the TTV Amplitudes

Before directly fitting the observed TTV signals, we evaluate the contribution from each planet to the TTVs of KOI-94c, KOI-94d, and KOI-94e. We divide the four planets into six pairs and integrate circular orbits for each pair using the best-fit masses by Weiss et al. (2013) listed in Table 5.2. Semi-amplitudes of the resulting TTVs of KOI-94c, KOI-94d, and KOI-94e are shown in Table 5.8. Considering the uncertainties of transit times listed in Tables 5.4 to 5.6 (typically 1.4 min, 0.3 min, and 0.9 min for KOI-94c, KOI-94d, and KOI-94e, respectively), this result indicates that KOI-94b has negligible contribution to the TTVs of the other three. In the following analysis, therefore, we integrate the orbits of the other three planets (KOI-94c, KOI-94d, and KOI-94e) only. We also find that the TTVs of KOI-94c and KOI-94e are mainly determined by the perturbation from the neighboring planet KOI-94d, while that of KOI-94d depends on both of its neighbors. Such dependence is naturally understood from the architecture of this system (see Figure 5.1). Consequently, each planet's TTV mainly depends on the parameters listed in the rightmost column of Table 5.8, where we define $\boldsymbol{e}_j = (e_j \cos\varpi_j, e_j \sin\varpi_j)$ $(j = {\rm c, d, e})$. Note that the TTV of each planet is insensitive to its own mass. This is why m_j $(j = {\rm c, d, e})$ is not included in the row for planet j.

Results

TTV of KOI-94e. — Since the TTV of KOI-94e is mainly determined by $\boldsymbol{e}_{\rm d}$ and $\boldsymbol{e}_{\rm e}$ (and $m_{\rm d}$, of course, which we fix at the RV value), we fit it first so as to constrain these parameters. We calculate $\chi^2_{\rm e}$ for $|e_{\rm d}\cos\varpi_{\rm d}|$, $|e_{\rm d}\sin\varpi_{\rm d}| \le 0.06$ and $|e_{\rm e}\cos\varpi_{\rm e}|$, $|e_{\rm e}\sin\varpi_{\rm e}| \le 0.25$ (which well cover the 1σ regions for these parameters obtained from the RVs) at the grid spacing of 0.01, fixing $e_{\rm c} = 0$ and planetary masses at the best-fit values from the RVs. However, we cannot fit the observed TTV well in both $m_{\rm d} = 106 M_\oplus$ and $73 M_\oplus$ cases. The best-fit for the former case, which gives $\chi^2_{\rm e} = 122$ for 4 degrees of freedom, is shown in Figure 5.6. For this reason, in addition to the fact that we have only eight transits observed for KOI-94e, we decide not to use the TTV of this planet to constrain the system parameters, but fit only the TTVs of KOI-94c and KOI-94d. The large discrepancy in the amplitudes of simulated and observed TTVs may suggest another source of perturbation which is not included in our model, such as a non-transiting planet or other minor bodies.

Grid-search for an initial parameter set. — Then we perform the grid-search fit to the TTVs of KOI-94c and KOI-94d to find an appropriate initial parameter set for the fol-

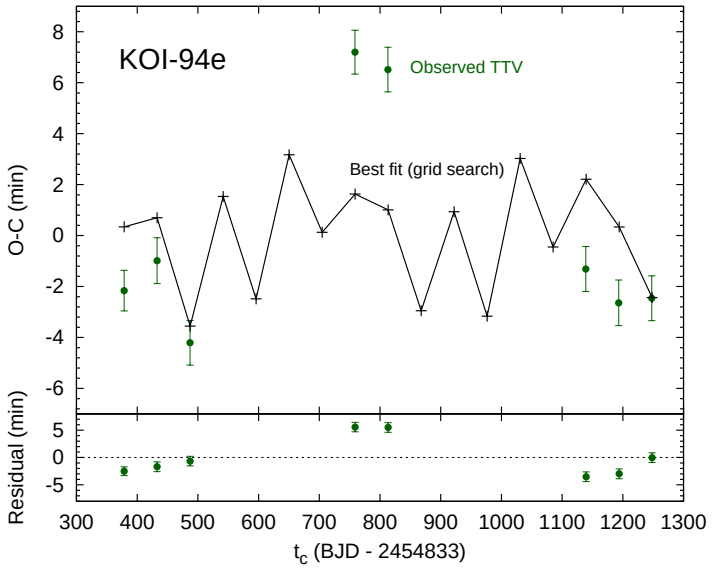

Figure 5.6 Best-fit simulated TTV of KOI-94e obtained by the grid-search for $m_{\rm d} = 106M_\oplus$ (black crosses connected with the solid line) with observed data (green points). The best-fit corresponds to $\boldsymbol{e}_{\rm d} = (0.02, 0.02)$ and $\boldsymbol{e}_{\rm e} = (0.04, 0.02)$.

lowing MCMC analysis. Based on the estimates given in Table 5.8, we fit these TTVs separately as follows. We first fit the TTV of KOI-94c varying $\boldsymbol{e}_{\rm c}$ and $\boldsymbol{e}_{\rm d}$ in $|e_j \cos\varpi_j|$, $|e_j \sin\varpi_j| \leq 0.10$ ($j = {\rm c}, {\rm d}$) at the grid-spacing of 0.01, and find one minimum of $\chi^2_{\rm c}$ for both $m_{\rm d} = 106M_\oplus$ and $m_{\rm d} = 73M_\oplus$ cases. Next, for all the sets of $(e_{\rm c}, \varpi_{\rm c}, e_{\rm d}, \varpi_{\rm d})$ in 2σ ($m_{\rm d} = 106M_\oplus$ case) or 1σ ($m_{\rm d} = 73M_\oplus$ case) confidence regions around the minimum, we run integrations varying $e_{\rm e}\cos\varpi_{\rm e}$ and $e_{\rm e}\sin\varpi_{\rm e}$ from -0.1 to 0.1 at the grid spacing of 0.01, $m_{\rm c}$ from 0 to $24M_\oplus$ at the grid spacing of $6M_\oplus$, and $m_{\rm e}$ from 7 to $57M_\oplus$ at the grid spacing of $10M_\oplus$ (all of these cover the 1σ intervals from RVs), to find the set of eight parameters that best fits the TTV of KOI-94d.

MCMC fit to the TTVs of KOI-94c and KOI-94d. — Choosing the above set as initial parameters, we then simultaneously fit the TTVs of KOI-94c and KOI-94d using an MCMC algorithm. In this fit, we use $\chi^2_{\rm c} + \chi^2_{\rm d}$ as the χ^2 statistic. The resulting best-fit parameters and their 1σ uncertainties are summarized in Table 5.9 for the two choices of $m_{\rm d}$ (the second and third columns). The best-fit simulated TTVs are plotted in Figures 5.7 and 5.8 for KOI-94c and KOI-94d, respectively.

Note that uncertainties of $e_{\rm c}\cos\varpi_{\rm c}$, $e_{\rm d}\cos\varpi_{\rm d}$, and $e_{\rm e}\cos\varpi_{\rm e}$ are relatively large for $m_{\rm d} = 73M_\oplus$ case. This is because the posterior distributions of these parameters have two peaks, the smaller of which lies close to the best-fit value for $m_{\rm d} = 106M_\oplus$ case. Considering this fact, the two results are roughly consistent with each other. Nevertheless, a total χ^2 in $m_{\rm d} = 73M_\oplus$ case is smaller by 40 for 57 d.o.f. than in $m_{\rm d} = 106M_\oplus$ case. This suggests that the TTV alone favors $m_{\rm d}$ smaller than the RV best-fit value, as will be confirmed in the next subsection.

Table 5.9. Best-fit Parameters Obtained from TTV Analysis

Parameter	Value ($m_{\rm d} = 106 M_\oplus$)	Value ($m_{\rm d} = 73 M_\oplus$)	Value (TTV only)
	KOI-94c		
$m_{\rm c}$ $(M_\oplus)$	$11.8^{+1.6}_{-1.5}$	$13.9^{+2.7}_{-2.7}$	$9.4^{+2.4}_{-2.1}$
$e_{\rm c} \cos \varpi_{\rm c}$	$0.0329^{+0.0047}_{-0.0055}$	$0.0092^{+0.0264}_{-0.0050}$	$0.0143^{+0.0080}_{-0.0059}$
$e_{\rm c} \sin \varpi_{\rm c}$	$-0.0104^{+0.0038}_{-0.0042}$	$-0.0031^{+0.0067}_{-0.0061}$	$0.0045^{+0.0091}_{-0.0079}$
$\chi^2_{\rm c}$	84	62	56
	KOI-94d		
$m_{\rm d}$ $(M_\oplus)$	106 (fixed)	73 (fixed)	$52.1^{+6.9}_{-7.1}$
$e_{\rm d} \cos \varpi_{\rm d}$	$0.055^{+0.011}_{-0.014}$	$-0.016^{+0.064}_{-0.011}$	$-0.022^{+0.014}_{-0.011}$
$e_{\rm d} \sin \varpi_{\rm d}$	$0.012^{+0.011}_{-0.012}$	$0.009^{+0.018}_{-0.018}$	$0.008^{+0.021}_{-0.018}$
$\chi^2_{\rm d}$	66	48	43
	KOI-94e		
$m_{\rm e}$ $(M_\oplus)$	$15.9^{+2.4}_{-2.2}$	$12.9^{+3.0}_{-2.3}$	$13.0^{+2.5}_{-2.1}$
$e_{\rm e} \cos \varpi_{\rm e}$	$0.067^{+0.014}_{-0.019}$	$-0.069^{+0.120}_{-0.018}$	$-0.078^{+0.021}_{-0.014}$
$e_{\rm e} \sin \varpi_{\rm e}$	$0.042^{+0.012}_{-0.017}$	$-0.022^{+0.032}_{-0.016}$	$-0.025^{+0.017}_{-0.014}$
$(\chi^2_{\rm c} + \chi^2_{\rm d})$/d.o.f	150/57	110/57	99/56

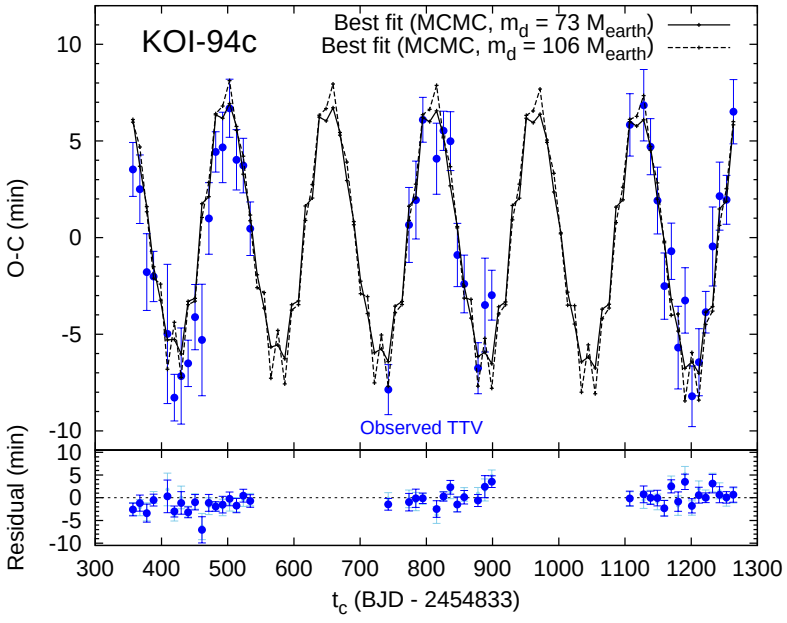

Figure 5.7 Best-fit simulated TTVs of KOI-94c obtained by the MCMC fit (black crosses connected with lines) with observed data (points with error bars). The result for $m_{\rm d} = 73 M_\oplus$ is plotted with solid lines (in $O - C$ plot) and blue points (in residual plot), and that for $m_{\rm d} = 106 M_\oplus$ with dashed lines and sky-blue points.

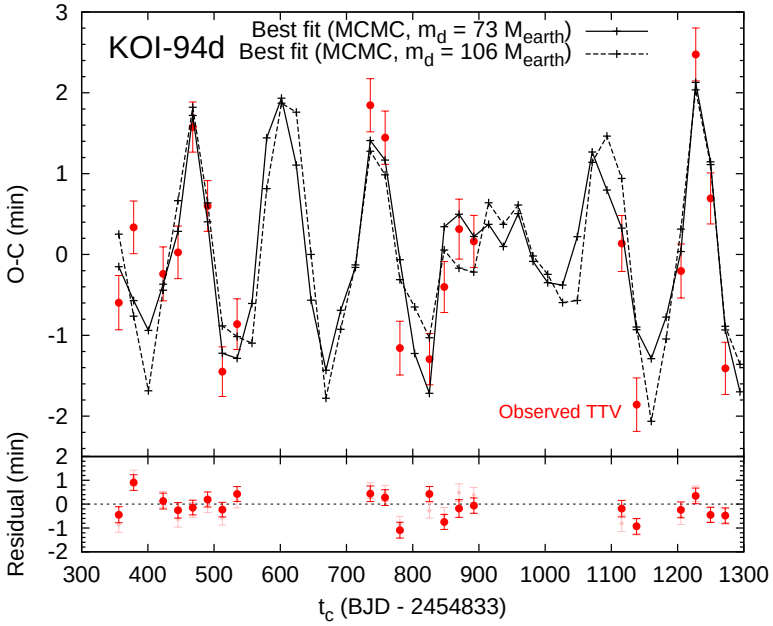

Figure 5.8 Best-fit simulated TTVs of KOI-94d obtained by the MCMC fit (black crosses connected with lines) with observed data (points with error bars). The result for $m_{\rm d} = 73 M_\oplus$ is plotted with solid lines (in $O-C$ plot) and red points (in residual plot), and that for $m_{\rm d} = 106 M_\oplus$ with dashed lines and pink points.

5.2.3 Solution Based Only on TTV

In order to obtain a solution independent of RVs, we perform the same MCMC analysis of TTVs of KOI-94c and KOI-94d, this time also allowing $m_{\rm d}$ to float. Since the above analyses suggest that the eccentricities of all the planets are small, we choose circular orbits with the best-fit RV masses as an initial parameter set. The resulting best-fit parameters are summarized in the rightmost column of Table 5.9, and the corresponding best-fit simulated TTVs are shown in Figures 5.9 and 5.10. As expected, we find a solution with small eccentricities and with $m_{\rm d}$ smaller than the RV best-fit value. This solution is similar to that for $m_{\rm d} = 73 M_\oplus$ case, except that $m_{\rm d}$ is even smaller.

5.2.4 Discussion: Comparison with the RV Results

While the values of $e_{\rm d}$ and $e_{\rm e}$ obtained in our TTV analysis are consistent with the RV values in Table 5.2, the best-fit $e_{\rm c}$ obtained from the TTV is $\sim 1.8\sigma$ smaller than the RV best fit ($e_{\rm c} = 0.43 \pm 0.23$). Considering the marginal detection of KOI-94c's RV and the dynamical stability of the system, however, the TTV value seems to be preferred. In fact, this value is robustly constrained by the clear TTV signal of KOI-94c; in the grid search performed in Section 5.2.2, we searched the region where $e_{\rm c} \lesssim 0.14$ to fit the TTV of this planet, but the resulting $\chi^2_{\rm c}$ strongly disfavored large $e_{\rm c}$ regions in both $m_{\rm d} = 106 M_\oplus$ and $m_{\rm d} = 73 M_\oplus$ cases.

The TTV values of $m_{\rm c}$ and $m_{\rm e}$ are consistent with the RV results, but $m_{\rm e}$ is constrained to a rather lower value than the RV best fit. Using this value, along with the photometric values of $R_p/R_\star$ and $\rho_\star$, and spectroscopic value of $M_\star$, the density of KOI-94e is given as $\rho_{pe} \sim 0.3\,{\rm g\,cm^{-3}}$. This implies that KOI-94e is one of the least-dense exoplanets discovered

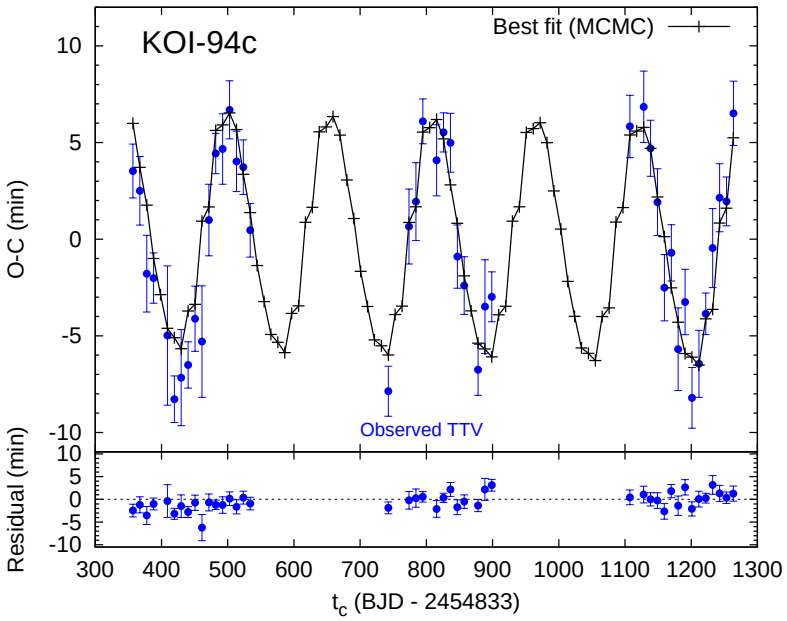

Figure 5.9 Best-fit simulated TTV of KOI-94c based on the TTV data alone (black crosses connected with lines) with observed data (blue points).

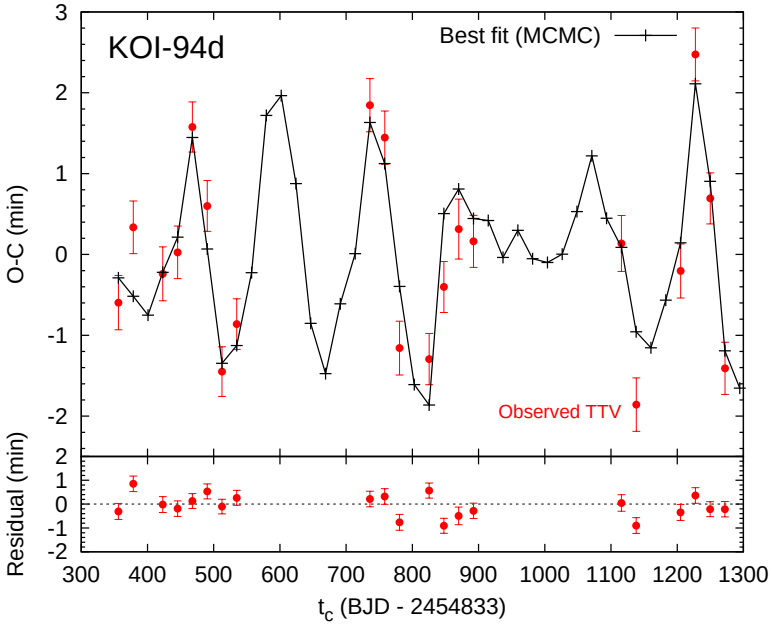

Figure 5.10 Best-fit simulated TTV of KOI-94d based on the TTV data alone (black crosses connected with lines) with observed data (red points).

so far.

The largest discrepancy arises in the value of $m_{\rm d}$, mass of KOI-94d, for which the TTV best-fit value is smaller than the RV value by $\sim 4\sigma$. The worse fit in the case of $m_{\rm d} = 106 M_\oplus$ is mainly due to the fact that the observed TTV amplitude of KOI-94c is smaller than expected from this value of $m_{\rm d}$. As shown in Table 5.8, the TTV of this planet is completely dominated by the perturbation from KOI-94d, and so the parameters relevant to this TTV are $m_{\rm d}$, $\boldsymbol{e}_{\rm c}$, and $\boldsymbol{e}_{\rm d}$. Table 5.8 also shows that $m_{\rm d} = 106 M_\oplus$ leads to the TTV semi-amplitude of ~ 11 min for $e_{\rm c} = e_{\rm d} = 0$, which is much larger than the observed TTV amplitude of KOI-94c (see Figure 5.5). As a result, the values of $\boldsymbol{e}_{\rm c}$ and $\boldsymbol{e}_{\rm d}$ are fine tuned to fit the observed signal, resulting in strict constraints on these parameters. The problem is that these values of $\boldsymbol{e}_{\rm c}$ and $\boldsymbol{e}_{\rm d}$ do not fit the TTV of KOI-94d well. In the grid search, we first fit the TTV of KOI-94c alone, and the best fit gives $\chi^2_{\rm c} = 66$ for $m_{\rm d} = 106 M_\oplus$. However, this value is largely increased in the simultaneous MCMC fit to the TTVs of KOI-94c and KOI-94d (Table 5.9), which implies that these two TTVs cannot be explained with the same set of $\boldsymbol{e}_{\rm c}$ and $\boldsymbol{e}_{\rm d}$. On the other hand, this tension does not exist in $m_{\rm d} = 73 M_\oplus$ case, in which both of the grid search and MCMC return the same values for the best-fit $\chi^2_{\rm c}$. In fact, the analysis using the analytic formulae of TTVs from two coplanar planets lying near a $j : j-1$ resonance (Lithwick et al. 2012) also supports the above reasoning, suggesting that $m_{\rm d}$ expected from the TTV of KOI-94c is rather small (see Appendix A).

For these reasons, it is clear that the TTV favors the solution with $m_{\rm d}$ smaller than the RV best-fit value. It is also true, however, that the RV of KOI-94d is detected with high significance, in contrast to those of the other planets. Indeed, we calculate the RVs using the best-fit TTV parameters and find that the resulting amplitude is much smaller than that observed by Weiss et al. (2013). Since its origin is not yet clear, this discrepancy motivates further investigation of the KOI-94 system including additional RV/TTV observations.

Finally, we note again that in the above analysis we just fit the *TTVs* rather than the *transit times* of KOI-94c and KOI-94d. For this reason, our solution corresponds to the planetary orbits whose periods are slightly different from the actually observed values. One may argue that such an approximate method leads to an incorrect solution. In order to assure that this is not the case, we fit the transit times of the two planets, choosing m, a, $e\cos\varpi$, $e\sin\varpi$, and $\omega + f$ of KOI-94c, KOI-94d, and KOI-94e at time T_0 as free parameters (fifteen parameters in total). We run two MCMC chains starting from (i) circular orbits with RV best-fit masses and (ii) a local minimum reached by the Levenberg-Marquardt method (Markwardt 2009) starting from the TTV best-fit parameters (rightmost column of Table 5.9). We find that the best-fit values of (m, e, ϖ) obtained in these ways show similar trends as the TTV best fit in Section 5.2.3, giving comparable values of reduced χ^2. Namely, the mass of KOI-94d is much smaller than the RV best fit and eccentricities of the three planets are close to zero.

Incidentally, as in the case of the fit to TTVs, the transit times of KOI-94d are less well reproduced than those of KOI-94c. In fact, the fit to transit times gives a better $\chi^2_{\rm c}$ than that to TTVs because the small linear trend apparent in the lower panel of Figure 5.9 is removed; on the other hand, the values of $\chi^2_{\rm d}$ are not very different in both cases. The difficulty in completely reproducing the orbit of KOI-94d may also indicate the presence of the additional perturber discussed in Section 5.2.2.

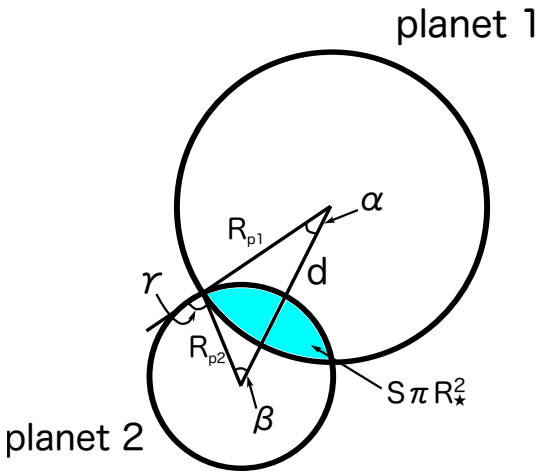

Figure 5.11 Two overlapping planets 1 and 2. The definitions of angles α, β, and γ are shown. Area of the shaded region corresponds to S in Equation (5.3) times the area of the stellar disk.

5.3 Analytic Formulation of the PPE

In this section, we present a general analytic model of the PPE caused by two planets 1 and 2 on circular orbits (see Appendix B for the formulation taking account of O(e) terms). In what follows, we use the stellar radius $R_\star$ as the unit length because all the observables are only related to the lengths normalized to this value.

5.3.1 Flux Variation Due to a PPE

A PPE is observed as an increase in the relative flux of a star (or a "bump" in the light curve) during the double transit of two planets. Assuming that the two overlapping planets are spherical and neglecting the effect of limb darkening, the increase in the relative flux S is given by the area of overlapping region of the two planets divided by that of the stellar disk (Figure 5.11):

$$S = \begin{cases} 0 & \text{for} \quad R_{p1} + R_{p2} < d, \\ \frac{1}{2\pi} R_{p1}^2 (2\alpha - \sin 2\alpha) + \frac{1}{2\pi} R_{p2}^2 (2\beta - \sin 2\beta) & \text{for} \quad |R_{p1} - R_{p2}| < d < R_{p1} + R_{p2}, \\ (\min(R_{p1}, R_{p2}))^2 & \text{for} \quad d < |R_{p1} - R_{p2}|, \end{cases} \tag{5.3}$$

where d is the distance between the centers of the two planets in the plane of the sky, and the angles α and β are defined as

$$\cos\alpha = \frac{R_{p1}^2 + d^2 - R_{p2}^2}{2R_{p1}d}, \ \cos\beta = \frac{R_{p2}^2 + d^2 - R_{p1}^2}{2R_{p2}d}. \tag{5.4}$$

An alternative expression of S for $|R_{p1} - R_{p2}| < d < R_{p1} + R_{p2}$ can be obtained from the derivative of S with respect to d. Using $\mathrm{d}\alpha/\mathrm{d}d$ and $\mathrm{d}\beta/\mathrm{d}d$ obtained from Equation (5.4) and $R_{p1}\sin\alpha = R_{p2}\sin\beta$, we obtain

$$\frac{\mathrm{d}S}{\mathrm{d}d} = -\frac{1}{\pi}\sqrt{-d^2 + 2(R_{p1}^2 + R_{p2}^2) - \left(\frac{R_{p1}^2 - R_{p2}^2}{d}\right)^2} \tag{5.5}$$

for $|R_{p1} - R_{p2}| < d < R_{p1} + R_{p2}$. Equation (5.5) can be integrated from $R_{p1} + R_{p2}$ to d by changing the variable from d to

$$\gamma \equiv \alpha + \beta = \pi - \arccos\left(\frac{R_{p1}^2 + R_{p2}^2 - d^2}{2R_{p1}R_{p2}}\right). \tag{5.6}$$

The result is

$$S = \frac{1}{\pi}\left[\frac{R_{p1}^2 + R_{p2}^2}{2}\gamma - R_{p1}R_{p2}\sin\gamma - (R_{p1}^2 - R_{p2}^2)\arctan\left(\frac{R_{p1} - R_{p2}}{R_{p1} + R_{p2}}\tan\frac{\gamma}{2}\right)\right]. \tag{5.7}$$

Here, S is given as a function of a single angle γ. These two expressions of S show that the shape of a bump due to a PPE is solely determined by d as a function of time, which will be derived in the following subsection.

The effect of limb darkening can be included in our model by multiplying S by a factor that corresponds to the limb darkening at the position on the stellar disk over which a PPE occurs. We adopt the quadratic limb-darkening law in Equation (5.1). For a PPE that occurs totally within the stellar disk, the approximation by Mandel and Agol (2002), which is valid for a small planet whose radius is less than about $0.1R_\star$, yields the modified relative brightening S' as

$$S' = S \cdot \frac{I(r_*)}{\int_0^1 dr 2rI(r)} = S \cdot \frac{1 - u_1(1 - \mu_*) - u_2(1 - \mu_*)^2}{1 - u_1/3 - u_2/6}, \tag{5.8}$$

where r_* is the distance to the overlapping region and $\mu_* = \mu(r_*)$. During the whole PPE, r_* is given in terms of d, $\Delta R_{12}^2 \equiv R_{p1}^2 - R_{p2}^2$, and r_j $(j = 1, 2)$, the radial coordinate of the planet j's center, as $r_* = \sqrt{(r_1^2 + r_2^2)/2 - d^2/4 + (r_2^2 - r_1^2 + \Delta R_{12}^2/2)\Delta R_{12}^2/2d^2}$.

5.3.2 Distance Between the Planets During a Double Transit

Hereafter, we adopt the Cartesian coordinate system (X, Y, Z) centered on the star, where $+Z$-axis is chosen in the direction of our line of sight, and X- and Y-axes are in the plane of the sky, forming a right-handed triad (see Figure 2.2). As stated in the note of Table 5.2, we align $+X$ axis with the ascending node of a virtual circular orbit whose angular momentum vector is parallel to the stellar spin vector, without loss of generality. In this coordinate system, the three-dimensional position of a planet is given by Equation (2.28).

Suppose that the two planets 1 and 2 are on Keplerian orbits whose semi-major axes are a_1 and a_2, respectively. Neglecting the corrections arising from the non-zero eccentricity, the two-dimensional position vectors $\boldsymbol{r}_j$ $(j = 1, 2)$ of these planets in the plane of the sky can be written as

$$\boldsymbol{r}_j = \begin{pmatrix} a_j\cos\Omega_j\cos(\omega_j + f_j) - b_j\sin\Omega_j\sin(\omega_j + f_j) \\ a_j\sin\Omega_j\cos(\omega_j + f_j) + b_j\cos\Omega_j\sin(\omega_j + f_j) \end{pmatrix} = \begin{pmatrix} \cos\Omega_j & -\sin\Omega_j \\ \sin\Omega_j & \cos\Omega_j \end{pmatrix}\begin{pmatrix} a_j\cos(\omega_j + f_j) \\ b_j\sin(\omega_j + f_j) \end{pmatrix}. \tag{5.9}$$

If the transits of the two planets are observed, a_j, b_j, R_{pj}, and the periods P_j are obtained as in Section 5.2. In this case, the relative motion of the planets is completely described except for the dependence on the relative nodal angle defined as

$$\Omega_{21} = -\Omega_{12} = \Omega_2 - \Omega_1. \tag{5.10}$$

Note that photometric surveys determine the absolute value of b, but not its sign. For a single transiting planet, b is conventionally defined to be positive (or equivalently, i is chosen to be in the range $[0, \pi/2]$), because the choice of its sign does not affect the transit signals. For multiple transiting planets, however, a different choice of the relative signs of b corresponds to a different orbital configuration. In this chapter, we choose b_1 to be positive (*i.e.*, $0 \leq i_1 \leq \pi/2$), but allow b_2 to be either positive or negative (*i.e.*, $0 \leq i_2 \leq \pi$). The sign of b_2, as well as the relative nodal angle Ω_{21}, is determined from the observed data of a PPE event.

During a double transit by planets $j = 1$ and 2, their phases at time t are given by

$$\omega_j + f_j = \frac{\pi}{2} + n_j(t - t_c^{(j)}), \tag{5.11}$$

where $n_j = 2\pi/P_j$ is the mean motion and $t_c^{(j)}$ is the central transit time of planet j in this double transit. We then expand Equation (5.9) to the first order of $n(t - t_c) \sim \mathcal{O}(a^{-1})$ to obtain

$$\boldsymbol{r}_j = \boldsymbol{v}_j(t - t_c^{(j)}) + \boldsymbol{r}_0^{(j)}, \tag{5.12}$$

where

$$\boldsymbol{v}_j = -a_j n_j \begin{pmatrix} \cos\Omega_j \\ \sin\Omega_j \end{pmatrix}, \quad \boldsymbol{r}_0^{(j)} = -b_j \begin{pmatrix} \sin\Omega_j \\ -\cos\Omega_j \end{pmatrix}. \tag{5.13}$$

These give the distance between the two planets d as[4]

$$d^2 = |\boldsymbol{r}_2 - \boldsymbol{r}_1|^2 = v^2 \left(t + \frac{r_0 \cos\theta_0}{v} \right)^2 + r_0^2 \sin^2\theta_0, \tag{5.14}$$

where $\boldsymbol{v} \equiv \boldsymbol{v}_2 - \boldsymbol{v}_1$, $\boldsymbol{r}_0 \equiv \boldsymbol{r}_0^{(2)} - \boldsymbol{v}_2 t_c^{(2)} - \boldsymbol{r}_0^{(1)} + \boldsymbol{v}_1 t_c^{(1)}$, $v \equiv |\boldsymbol{v}|$, $r_0 \equiv |\boldsymbol{r}_0|$, and θ_0 is the angle between $\boldsymbol{v}$ and $\boldsymbol{r}_0$. Thus, the minimum value of d in this double transit

$$d_{\min} \equiv r_0 \sin\theta_0, \tag{5.15}$$

is reached at the time

$$t = t_{\min} \equiv -\frac{r_0 \cos\theta_0}{v}. \tag{5.16}$$

If $d_{\min} < R_{p1} + R_{p2}$, a PPE occurs during this double transit for a duration of

$$\Delta t = \frac{2}{v} \sqrt{(R_{p1} + R_{p2})^2 - d_{\min}^2}. \tag{5.17}$$

Equations (5.15) to (5.17) can be readily understood by considering the geometry of the PPE shown in Figure 5.12. The explicit expressions of v, r_0, and $\cos\theta_0$ are

$$v^2 = a_1^2 n_1^2 + a_2^2 n_2^2 - 2a_1 n_1 a_2 n_2 \cos\Omega_{21}, \tag{5.18}$$

$$\begin{aligned} r_0^2 = {} & (a_1 n_1 t_c^{(1)})^2 + (a_2 n_2 t_c^{(2)})^2 + b_1^2 + b_2^2 + 2(a_1 n_1 t_c^{(1)} b_2 - a_2 n_2 t_c^{(2)} b_1) \sin\Omega_{21} \\ & - 2(a_1 n_1 t_c^{(1)} a_2 n_2 t_c^{(2)} + b_1 b_2) \cos\Omega_{21}, \end{aligned} \tag{5.19}$$

$$\begin{aligned} \cos\theta_0 = \frac{1}{v r_0} \big[& -(a_1 n_1)^2 t_c^{(1)} - (a_2 n_2)^2 t_c^{(2)} + (a_2 n_2 b_1 - a_1 n_1 b_2) \sin\Omega_{21} \\ & + a_1 n_1 a_2 n_2 (t_c^{(1)} + t_c^{(2)}) \cos\Omega_{21} \big]. \end{aligned} \tag{5.20}$$

[4]Strictly speaking, this expression of d contains $\mathcal{O}((n(t - t_c))^2)$ terms, and so we should use the second-order expansion in Equation (5.12). Nevertheless, this only introduces the correction of order $(b/a)^2 \sim a^{-2}$, which can be safely neglected in our treatment below.

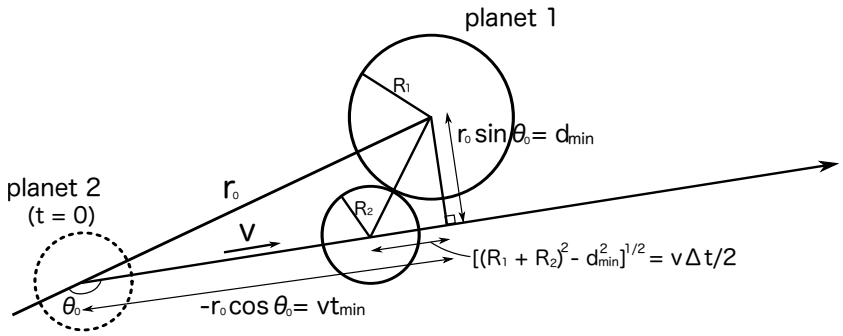

Figure 5.12 Geometry of the PPE. The relations between $(d_{\min}, t_{\min}, \Delta t)$ and (v, r_0, θ_0) are depicted. Note that the relative position of planet 2 at $t = 0$ is not its real position at the time, but is determined by extrapolating the linear orbit given by Equation (5.12). This geometry shows that a PPE occurs only when $\cos\theta_0 < 0$, in which case $t_{\min}$ given by Equation (5.16) is always positive.

5.3.3 Reconstruction of the Mutual Inclination Ω_{21}

The observed shape of a bump is characterized by its maximum height $S_{\max}$, central time $t_{\min}$, and duration Δt. If the bump is not saturated, *i.e.*, $d_{\min} > |R_{p1} - R_{p2}|$, $S_{\max}$ is uniquely translated into $d_{\min}$ via Equation (5.3). In this case, we can use Equations (5.15) to (5.17), the expressions for the three observables of a bump ($d_{\min}$, $t_{\min}$, Δt), to calculate

$$v = \frac{2}{\Delta t}\sqrt{(R_{p1} + R_{p2})^2 - d_{\min}^2}, \tag{5.21}$$

$$r_0^2 = d_{\min}^2 + (vt_{\min})^2 = d_{\min}^2 + \left(\frac{2t_{\min}}{\Delta t}\right)^2 \left[(R_{p1} + R_{p2})^2 - d_{\min}^2\right], \tag{5.22}$$

$$\tan\theta_0 = -\frac{d_{\min}}{vt_{\min}} = -\frac{\Delta t}{2t_{\min}} \frac{d_{\min}}{\sqrt{(R_{p1} + R_{p2})^2 - d_{\min}^2}}. \tag{5.23}$$

Furthermore, Equations (5.18) and (5.19), the explicit expressions for v and r_0, are rewritten as

$$\cos\Omega_{21} = \frac{a_1^2 n_1^2 + a_2^2 n_2^2 - v^2}{2a_1 a_2 n_1 n_2}, \tag{5.24}$$

$$\sin\Omega_{21} = \frac{r_0^2 - x_1^2 - x_2^2 + 2(\boldsymbol{x}_1 \cdot \boldsymbol{x}_2)\cos\Omega_{21}}{2|\boldsymbol{x}_1 \times \boldsymbol{x}_2|}, \tag{5.25}$$

where we define $\boldsymbol{x}_1 = (a_1 n_1 t_c^{(1)}, b_1)$ and $\boldsymbol{x}_2 = (a_2 n_2 t_c^{(2)}, b_2)$. In this way, the relative nodal angle Ω_{21} can be specified explicitly from ($d_{\min}$, $t_{\min}$, Δt) along with the photometrically obtained parameters $(a_j, b_j, n_j, t_c^{(j)}, R_{pj})$, provided that the sign of b_2 is determined. Although we do not present any general procedure to determine the sign of b here, it is possible to do so at least empirically, as described in Section 5.4. Equation (5.25) shows that $\sin\Omega_{21}$ is only weakly constrained when $a_1 n_1 / b_1 \simeq a_2 n_2 / b_2$, in which case the coefficients in front of $\sin\Omega_{21}$ in Equations (5.19) and (5.20) are close to zero because $t_c^{(1)} \simeq t_c^{(2)}$.

In the case of $d_{\min} < |R_{p1} - R_{p2}|$, only the upper limit on $d_{\min}$ can be obtained, and so the entire shape of the bump is required to determine Ω_{21}.

Note that the formulation in this section is also valid even in the presence of non-Keplerian effects. In such a case, the Keplerian orbital elements in this formulation should be interpreted as the osculating orbital elements (*c.f.*, Section 2.1.3) around a certain double transit.

5.4 Application to the PPE Observed in the KOI-94 System

Hirano et al. (2012a) fit the whole light curve of the PPE for u_1, u_2, $t_c^{(\mathrm{d})}$, $t_c^{(\mathrm{e})}$, and Ω_{de} using an MCMC algorithm, and estimated the relative nodal angle between KOI-94d (planet 1 in Section 5.3) and KOI-94e (planet 2 in Section 5.3) to be $\Omega_{\mathrm{ed}} = 1.15 \pm 0.55$ deg.[5] In their analysis, the light curve is modeled as a sum of two single transit light curves (Ohta et al. 2009) and the bump function, which is calculated essentially in the same way as described in Section 5.3, but neglecting the effect of limb darkening. In this section, we confirm that this is a unique solution expected from the observed features of the bump, based on analytic expressions obtained in the previous section.

The top panel of Figure 5.13 plots d_{min} as a function of Ω_{ed} in the double transit during which the PPE was observed, calculated by Equations (5.15), (5.19), and (5.20). In Figure 5.13, we fix a_j, b_j, n_j, and R_{pj} at the values publicized by the *Kepler* team (Table 5.2), and $t_c^{(j)}$ at the best-fit values obtained by Hirano et al. (2012a). The red and blue lines correspond to the cases of $b_{\mathrm{e}} > 0$ and $b_{\mathrm{e}} < 0$, respectively, and the solid parts of the lines show the range of Ω_{ed} for which the PPE occurs, *i.e.*, $d_{\mathrm{min}} < R_{p\mathrm{d}} + R_{p\mathrm{e}}$. This panel implies that the PPE itself could have occurred for a wide range of Ω_{ed} except for those around ± 50 deg. The central time t_{min} and duration Δt for a specific value of Ω_{ed} can be obtained from the middle and bottom panels. These also indicate that a wide variety of bumps could have resulted depending on the value of Ω_{ed}.

Indeed, these three observables have enough information to reconstruct the value of Ω_{ed}, in addition to the sign of b_{e}. As for the observed eclipse, the best-fit light curve yields $S_{\mathrm{max}} \approx 3.88 \times 10^{-4}$, $t_{\mathrm{min}} \approx 378.508$ day (BJD $-$ 2454833), and $\Delta t \approx 0.076$ days. Equation (5.3) shows that the above value of S_{max} uniquely translates into $d_{\mathrm{min}} \approx 0.0829$. The values of these d_{min}, t_{min}, and Δt are plotted in Figure 5.13 in horizontal dashed lines.[6] For the observed value of d_{min}, Figure 5.13 allows eight solutions, four for each of $b_{\mathrm{e}} > 0$ and $b_{\mathrm{e}} < 0$. However, the asymmetry of t_{min} curve in the middle panel of Figure 5.13 shows that only the solutions around $\Omega_{\mathrm{ed}} \sim 0$ deg (slightly positive, $b_{\mathrm{e}} > 0$) or $\Omega_{\mathrm{ed}} \sim 180$ deg ($b_{\mathrm{e}} < 0$) are possible. These correspond to the nearly parallel and anti-parallel planetary orbits, respectively. This degeneracy can be broken with the value of Δt: the retrograde (anti-parallel) orbit results in a much shorter bump due to the larger relative velocity between the planets than the prograde (parallel) case. The bottom panel of Figure 5.13 shows that the observed duration allows only the prograde orbit with $b_{\mathrm{e}} > 0$. In this way, $\Omega_{\mathrm{ed}} = 1.15$ deg (and $b_{\mathrm{e}} > 0$) proves to be the unique solution that reproduces the observed features of the bump. In fact, one can show that any set of $(d_{\mathrm{min}}, t_{\mathrm{min}}, \Delta t)$ allows

[5] Note that the "mutual inclination" δ defined in Hirano et al. (2012a) corresponds to $\Omega_{\mathrm{de}} = -\Omega_{\mathrm{ed}}$ in our definition.

[6] The analysis that includes the effect of limb darkening by Equation (5.8) returned the same values of d_{min}, t_{min}, and Δt with a slightly different $\Omega_{\mathrm{ed}} \sim 1.21$ deg, in which case the following discussion is also valid.

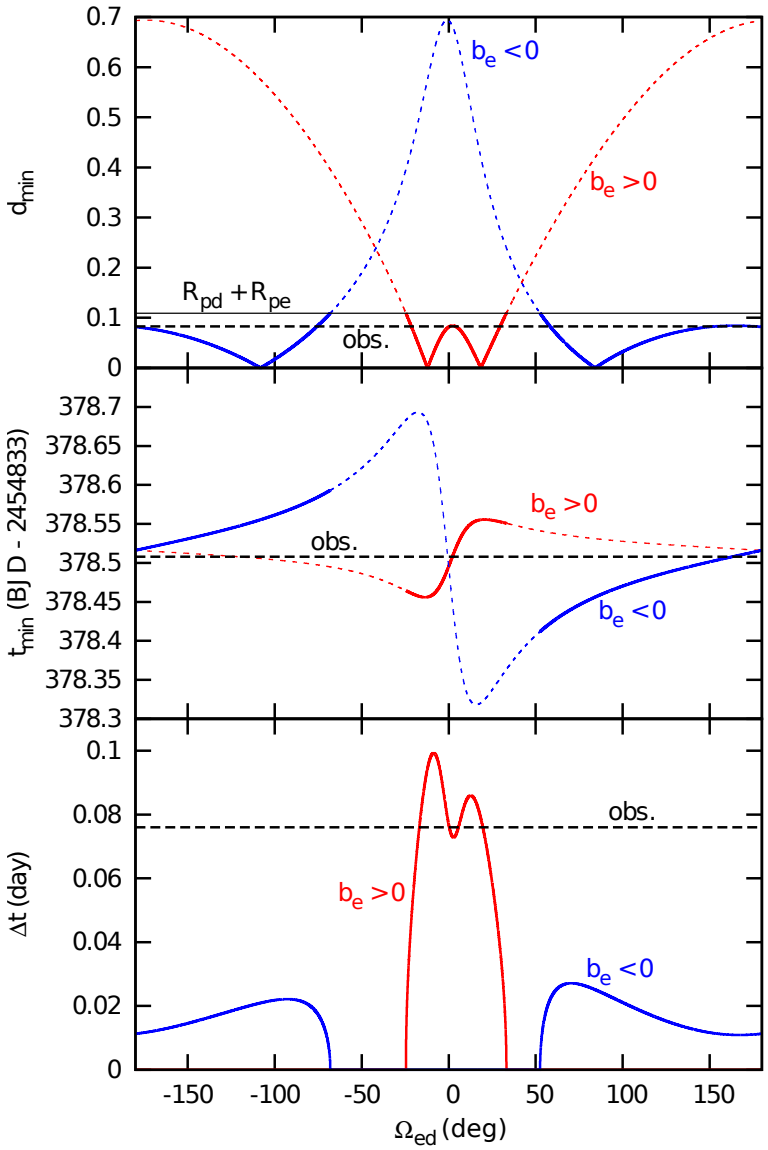

Figure 5.13 Plots to determine $\Omega_{\rm ed}$ and the sign of $b_{\rm e}$ from the observed bump features. (Top) Relation between $d_{\rm min}$ and $\Omega_{\rm ed}$ based on Equations (5.15), (5.19), and (5.20). The red and blue lines correspond to the $b_{\rm e} > 0$ and $b_{\rm e} < 0$ cases, respectively. The solid parts show the region where $d_{\rm min}$ is less than $R_{pd} + R_{pe}$ (black solid line), *i.e.*, the PPE occurs. The dashed black line shows the value of $d_{\rm min}$ obtained from the fit for the observed PPE light curve. (Middle) Relation between $t_{\rm min}$ and $\Omega_{\rm ed}$ based on Equations (5.16) and (5.18) to (5.20). (Bottom) Relation between Δt and $\Omega_{\rm ed}$ based on Equations (5.17), (5.15), and (5.18) to (5.20).

the unique determination of $\Omega_{\rm ed}$ in the case discussed here. Mathematically, this comes from the fact that the curve $(d_{\rm min}, t_{\rm min}, \Delta t)$ parametrized by $\Omega_{\rm ed}$ has no self intersection.

Combining $\Omega_{\rm ed}$ with the result of the spin-orbit angle measurement, both $\Omega_{\rm d}$ and $\Omega_{\rm e}$ can be constrained. Since we have assumed that $b_{\rm d} > 0$ or $0 \leq i_{\rm d} \leq \pi/2$, the observed spin-orbit angle λ is equal to $\Omega_{\rm d}$ in our definition, and so $\Omega_{\rm d} = -6^{+13}_{-11}$ deg. Thus, $\Omega_{\rm ed} = \Omega_{\rm e} - \Omega_{\rm d} = 1.15 \pm 0.55$ deg (Hirano et al. 2012a) gives $\Omega_{\rm e} = -5^{+13}_{-11}$ deg (Table 5.2). Using these two parameters along with the transit parameters in Table 5.2, we trace the orbits of KOI-94d and KOI-94e for one hundred years, assuming that their orbits never change over time. The result of this calculation indicates that the next PPE will occur in the double transit around BJD = 2461132.4 (date in UT 2026 April 1/2), which is the third double transit after the one discussed here. The same conclusion is obtained even when we vary $\Omega_{\rm ed}$ within its 3σ interval. In a real system, however, it is not at all obvious that the next PPE will occur in this double transit, because orbital elements do change over time; in the next section, we discuss how the mutual gravitational interaction among the planets affects this result.

5.5 Implication for the Next PPE: the Effect of Multi-body Interaction

In Section 5.2, we obtained a set of system parameters by analyzing photometric light curves of the three planets. Based on this result, we now address the question whether the PPE will occur in the same double transit as predicted in Section 5.4, even in the presence of the mutual gravitational interaction among the planets.

5.5.1 Fixing Double-transit Parameters

In order to determine the relative nodal angle crucial in predicting the next PPE, we refit the transit light curve around BJD = 2454211.5, in which the PPE was observed. We model the light curve as described in Section 5.4 including the effect of limb darkening to obtain $R_{p\rm d}$, $R_{p\rm e}$, $a_{\rm d}$, $a_{\rm e}$, $b_{\rm d}$, $b_{\rm e}$, $t_c^{(\rm d)}$, $t_c^{(\rm e)}$, and $\Omega_{\rm ed}$. Here, the same prior as used in fitting the phase-folded light curve is assumed to fix the value of $a_{\rm e}$. We adopt the limb-darkening coefficients obtained from the light curve of KOI-94d, $u_1 = 0.40$ and $u_2 = 0.14$, which are determined with the best precision among the three planets. The result is summarized in Table 5.10.

In this fit, $R_{p\rm d}/R_\star$ is different from our revised mean value ($R_{p\rm d}/R_\star = 0.07029^{+0.00014}_{-0.00015}$) by 1.8σ. We suspect that this difference comes from the systematics introduced in the detrending procedure. When an artifact or some other astrophysical processes (*e.g.*, star spots) accidentally increase the relative flux just before (or after) the transit, the result of detrending is biased towards such features in setting the baseline of the transit light curve. If we use a wider range of data points, the effect of such a small feature is averaged out and does not change the result significantly. In contrast, if a narrow region around a transit is used, the baseline is somewhat distorted and the resulting detrended light curve becomes either deeper or shallower. Such systematics are averaged in the phase-folded light curves, but may be significant in an individual transit. In the case of the double transit light curve analyzed here, the relative flux begins to increase just before the ingress, and the depth of the transit is shallower in the first half of the transit than in the latter, making

Table 5.10. Best-fit Parameters for the PPE Light Curve

Parameter	Best-fit Value
$R_{pd}/R_\star$	0.06942 ± 0.00046
$R_{pe}/R_\star$	0.04118 ± 0.00069
$a_d/R_\star$	26.39 ± 0.29
$a_e/R_\star$	47.87 ± 0.68
b_d	$0.273^{+0.036}_{-0.040}$
b_e	$0.347^{+0.036}_{-0.041}$
$t_c^{(d)}$ (BJD $-$ 2454833)	378.51372 ± 0.00023
$t_c^{(e)}$ (BJD $-$ 2454833)	378.51788 ± 0.00060
Ω_{ed} (deg)	1.19 ± 0.55
χ^2/d.o.f	746/687

the light curve slightly asymmetric. This feature, along with the fact that the revised R_{pd} gives better χ^2 in all the other transit light curves than R_{pd} given by the *Kepler* team, suggests that the discrepancy in R_{pd} is caused by such an incidental brightening. To test this scenario, we repeat the analysis above changing the span of detrending from ~ 1 day to ~ 0.5 days, and find that the resulting mean transit parameters are consistent with those above, but the depth of the double-transit light curve becomes deeper, consistently with our revised parameters.

5.5.2 Evaluation of the Multi-body Effect

The occurrence of the PPE in the multi-body context can be assessed in a similar way as in Section 5.4; we compare $R_{pd} + R_{pe}$ with $d_{\min}$ calculated from Equations (5.15), (5.19), and (5.20), but this time the variation of orbital elements must be taken into account. Specifically, we need to evaluate the variations of the parameters relevant to $d_{\min}$, *i.e.*, scaled semi-major axis $a/R_\star$, mean motion n, transit center of the double transit t_c, impact parameter b, and nodal angle Ω (as long as the eccentricities are small). In order to give an estimate for these variations, we integrate the orbits of the three planets using the best-fit (m, e, ϖ) in the rightmost column of Table 5.9 up to BJD = 2461132.4, the double transit in which the PPE is expected from the two-body analysis in Section 5.4. The results are the following:

1. The oscillation amplitudes of a_d and a_e are less than 5×10^{-5} AU ($\sim 0.03\%$) and 4×10^{-4} AU ($\sim 0.13\%$), respectively. Since these are much smaller than the observed uncertainties of $a_d/R_\star$ and $a_e/R_\star$ ($\sim 1\%$), the multi-body effect can be neglected for these two parameters.

2. Corresponding to the oscillations in semi-major axes above, n_d and n_e also show the modulations whose peak-to-peak amplitudes are $\sim 2\pi(0.01\,\mathrm{day})^{-1}$ and $\sim 2\pi(0.1\,\mathrm{day})^{-1}$, respectively. These are much larger than the uncertainties in n_d and n_e that come from those in P_d and P_e, and so the multi-body effect is important for these parameters.

3. The differences of the periods calculated from the transit centers in the first ~ 1000 days (the range in which we analyzed the TTVs) of integration and from the whole orbit are at most comparable to the observed uncertainties of these parameters in Table 5.7. Thus the uncertainties of $t_c^{(\mathrm{d})}$ and $t_c^{(\mathrm{e})}$ can be evaluated using those of P and t_0 in the table. Note that the effect of TTV is taken into account in obtaining these errors.

4. Monotonic increase in i_d and decrease in i_e lead to at most $\sim 30\,\%$ variations of b_d and b_e, larger than the observed errors. The multi-body effect is dominant for these parameters.

5. $\Omega_\mathrm{d}/\Omega_\mathrm{e}$ also monotonically increases/decreases, but only by $< 0.03\,\mathrm{deg}$. This means that the uncertainty in the relative nodal angle Ω_ed is completely dominated by the error in Table 5.10, and the multi-body effect is negligible.

The above results indicate that the multi-body effect is the most significant for b_d and b_e. In order to relate the values of these parameters to the occurrence of the PPE during the double transit around BJD = 2461132.4, we use Equations (5.15), (5.19), and (5.20) to calculate the maximum value of d_min during this double transit in terms of b_d and b_e, varying (i) a_d, a_e, $t_c^{(\mathrm{d})}$, $t_c^{(\mathrm{e})}$, and Ω_ed within 1σ intervals estimated by the photometric analyses, and (ii) n_d and n_e by the amplitudes of modulations estimated above. The region of (b_d, b_e) plane in which $d_\mathrm{min} < R_{p\mathrm{d}} + R_{p\mathrm{e}}$, *i.e.*, the PPE occurs in this double transit, is shown in Figure 5.14 with light-gray shade.[7] When we vary the parameters in the set (i) within their 2σ and 3σ intervals, the edges of the shaded region can be as narrow as solid- and dashed-black lines. In fact, the gray-shaded region is mainly determined by the difference between b_d and b_e, as seen from this figure, and the edge of this region is found to be most sensitive to the uncertainties in $t_c^{(\mathrm{d})}$ and $t_c^{(\mathrm{e})}$. The former fact originates from the well-aligned orbital planes of KOI-94d and KOI-94e: since their orbital planes are nearly parallel in the plane of the sky, the minimum separation during the double transit in which KOI-94d overtakes KOI-94e is nearly the same as the difference between b_d and b_e. However, if their transit times are too far away from each other, such closest encounter may occur out of the double transit. This explains the latter feature. The PPE occurrence for different choices of (m, e, ϖ) can be judged by evaluating the variations of b_d and b_e in this plot. Since the variations of a, n, t_c, and Ω_ed would be of the same order as long as the resulting TTVs are consistent with the observation, we fix the shaded area in Figure 5.14 determined by these parameters. We perform a similar MCMC calculation as in Section 5.2.3 to obtain the distribution of (b_d, b_e) in the double transit at issue; we fit the observed TTVs again using the same χ^2, but this time extend the orbit integration up to BJD = 2461132.4 and record the final values of b_d and b_e calculated via $b = a\cos i/R_\star$.[8] The resulting distribution of (b_d, b_e) is plotted with red points in Figure 5.14. We also repeat the same procedures fixing $m_\mathrm{d} = 106 M_\oplus$ and $m_\mathrm{d} = 73 M_\oplus$, and the distributions for these cases are plotted with blue points for comparison. In these calculations, we choose

[7] Here, the small uncertainties in $R_{p\mathrm{d}}$ and $R_{p\mathrm{e}}$ are neglected.

[8] Here we adopt $R_\star = (1.37 \pm 0.02) R_\odot$ obtained from photometric $a_\mathrm{d}/R_\star$, P_d, and spectroscopic $M_\star$. This value is slightly smaller than $R_\star = (1.52 \pm 0.14) R_\odot$ obtained by Weiss et al. (2013) using the Spectroscopy Made Easy (Valenti and Piskunov 1996), but this difference is consistent with the conclusion of Torres et al. (2012) that the $\log g$ value based on the Spectroscopy Made Easy is systematically underestimated for stars with $T_\mathrm{eff} \gtrsim 6,000\,\mathrm{K}$.

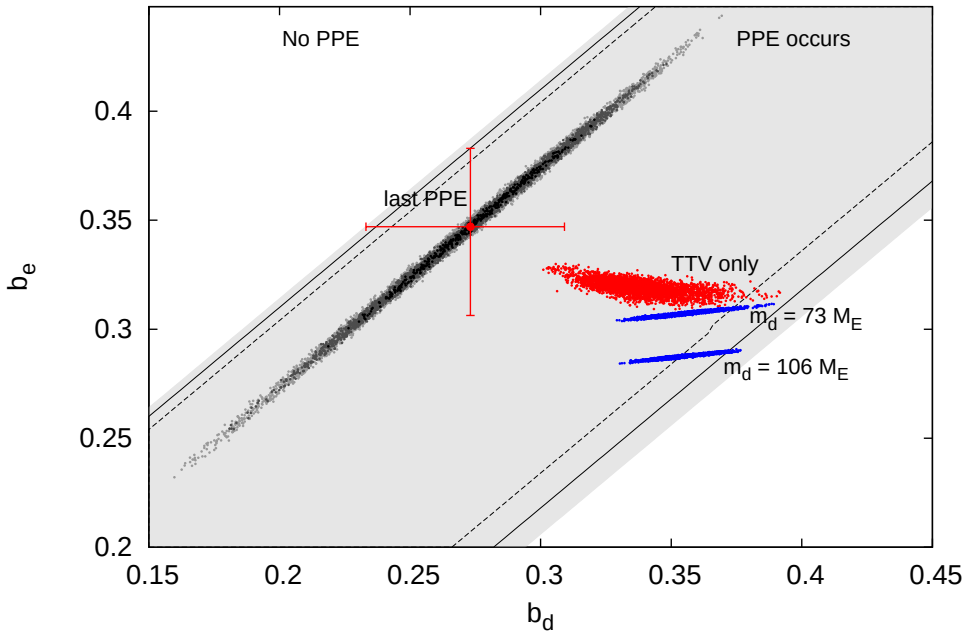

Figure 5.14 Relation between the occurrence of the PPE by KOI-94d and KOI-94e and the values of their impact parameters in the double transit around BJD = 2461132.4. If $(b_{\rm d}, b_{\rm e})$ in this double transit is inside the gray-shaded region, PPE occurs for all the values of photometrically derived parameters within 1σ of their best-fit values. When we vary them within their 2σ and 3σ intervals, the corresponding boundaries become solid- and dashed-black lines, respectively. The values of ($b_{\rm d}$, $b_{\rm e}$) at the last PPE is shown by the red point with error bars, and black, dark-gray, and light-gray points around it respectively show their 1σ, 2σ, and 3σ confidence regions. Red and blue points are the distributions of ($b_{\rm d}$, $b_{\rm e}$) in the double transit around BJD = 2461132.4 for the three different solutions in Table 5.9. The scattering of each set of points reflects the uncertainties in (m, e, ϖ).

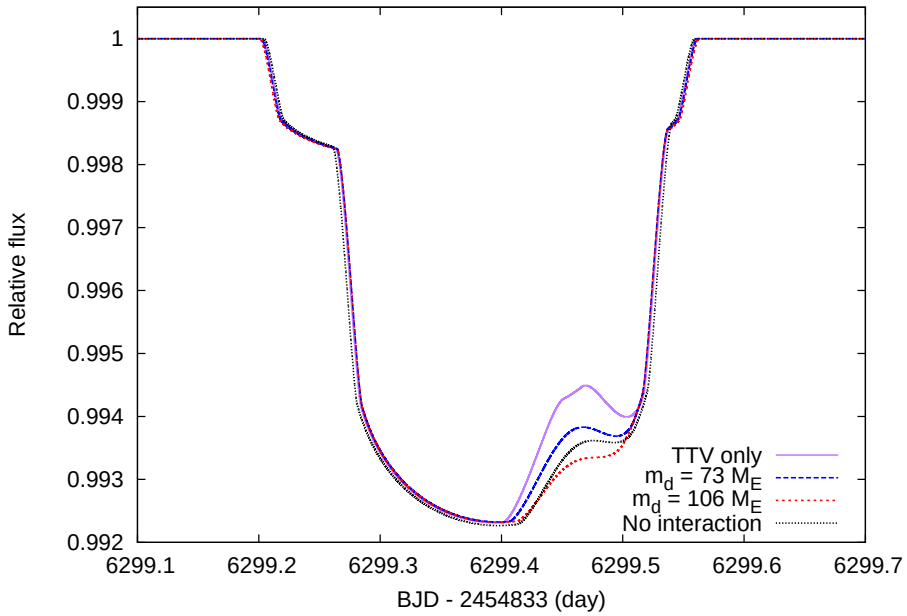

Figure 5.15 Expected light curves of the PPE in the double transit around BJD = 2461132.4 (date in UT 2026 April 1/2). The black dotted curve (No interaction) shows the result for the parameters in Table 5.10. The other curves use the median values of $(b_{\rm d}, b_{\rm e})$ for the three distributions in Figure 5.14, with other parameters fixed at the same values as above.

the initial values of $i_{\rm d}$ and $i_{\rm e}$ based on $(b_{\rm d}, b_{\rm e}) = (0.2951, 0.3693)$ in Table 5.10, a red point with error bars in Figure 5.14, rather than the mean values obtained from the phase-folded light curves in Table 5.3. This is because the mean parameters do not take account of the actual occurrence of the PPE. The black, dark-gray, and light-gray points around the double-transit value in Figure 5.14 respectively show its 1σ, 2σ, and 3σ confidence regions based on the posterior distribution of the double-transit fit. Here, the difference between $b_{\rm d}$ and $b_{\rm e}$ is rather sharply constrained by the minimum separation between the planets, namely, the height of the bump caused by the PPE. Even considering this uncertainty in the initial $(b_{\rm d}, b_{\rm e})$, as well as the significant variation of impact parameters (or inclinations) due to the multi-body effect, $(b_{\rm d}, b_{\rm e})$ around BJD = 2461132.4 are well inside the region where the PPE occurs, at least within 1σ of transit and TTV parameters for all the three solutions.

For the best-fit (m, e, ϖ) obtained from the TTV alone, the expected height of the bump is much larger than in the last PPE (Figure 5.15), and so the detection of this PPE is highly feasible. In contrast, for (m, e, ϖ) based on the RV values of $m_{\rm d}$, the bump height is comparable to the last PPE. This difference may be used to settle the difference of $m_{\rm d}$ values in RV and TTV analyses. For the RV-based solutions, the blue distributions in Figure 5.14 indicate that the PPE may not even happen when the variation of $b_{\rm d}$ is too large (corresponding to the large $m_{\rm c}$ values), and/or $\gtrsim 2\sigma$ deviations of $t_c^{(\rm d)}$ and $t_c^{(\rm e)}$ from the linear ephemerides make the shaded region too narrow for the PPE to occur (see solid and dashed lines).

We also check the other two double transits before the one discussed above (around BJD = 2457982 and BJD = 24583612), in case that the variations of $b_{\rm d}$ and $b_{\rm e}$ lead to the

PPE which never happens without the interaction among the planets. In both of them, we find that the PPE does not happen for any possible values of $b_{\rm d}$ and $b_{\rm e}$ (from 0 to 1). Therefore, we can safely conclude that the next PPE will still occur during the same double transit as predicted by the two-body calculation, even when we include the mutual gravitational interaction among the planets.

5.6 Summary of This Chapter

We have performed an intensive TTV analysis in the KOI-94 system, which is the first multi-planetary system exhibiting the PPE (planet-planet eclipse, Hirano et al. 2012a). Comparison of the resulting system parameters with those estimated independently of the RV (radial velocity) data (Weiss et al. 2013) works as a valuable test to examine the reliability and limitation of the TTV analysis for other planetary systems for which the RV data are difficult to obtain. Furthermore, a possible discrepancy between the two estimates, if any, would be even useful in exploring additional planets or other interesting implications (*e.g.*, Nesvorný et al. 2012).

Among the four planets reported so far, we considered the TTVs of KOI-94c, KOI-94d, and KOI-94e; we made sure that the contribution from the innermost and smallest planet KOI-94b is negligible at the current level of observational uncertainties.

We numerically integrated the orbits of the three planets that are directly incorporated in the MCMC search for the best-fit values of their masses, eccentricities, and longitudes of periastrons; our best-fit values include $m_{\rm c} = 9.4^{+2.4}_{-2.1} M_\oplus$, $m_{\rm d} = 52.1^{+6.9}_{-7.1} M_\oplus$, $m_{\rm e} = 13.0^{+2.5}_{-2.1} M_\oplus$, and $e \lesssim 0.1$ for all the three planets. Those results are in reasonable agreement with the RV results (Weiss et al. 2013), but here we note a few possible interesting points:

1. Although the RV analysis results in a fairly large eccentricity for KOI-94c ($e_{\rm c} = 0.43 \pm 0.23$), the TTVs indicate a significantly smaller value. In fact, the stability analysis of the system favors the TTV result.

2. The TTV best-fit value of $m_{\rm d}$ differs from the RV result $m_{\rm d} = 106 \pm 11 M_\oplus$ by $\sim 4\sigma$ level. If the TTV value is correct, KOI-94d has low density and may be inflated, in contrast to the conclusion obtained by Weiss et al. (2013).

3. The TTV of the outermost planet KOI-94e is not well reproduced in the current modeling with the three planets. This might suggest the presence of additional planets and/or minor bodies that have evaded the detection so far.

It is premature to draw any decisive conclusions at this point. Nevertheless, the above possible discrepancies between the TTV and RV analyses point to the importance of future follow-up observations of the KOI-94 system.

In addition, we constructed an analytic model of the PPE. We derived a practical approximate formula that explicitly yields the difference between the longitudes of ascending nodes (mutual inclination in the plane of the sky) of the two planets in terms of the observed height, central time, and duration of the brightening caused by the PPE. We showed that the PPE light curve observed in the KOI-94 system indeed gives a unique solution for the mutual inclination. The effect of the non-zero eccentricities is taken into account in the formulation described in Appendix B, though it can be safely neglected

for the KOI-94 system. Combining the TTV best-fit parameters with our analytic PPE model, the next PPE in this system is predicted to occur in the double transit around BJD = 2461132.4 (date in UT 2026 April 1/2). The occurrence of the next PPE is robust against the 1σ uncertainties of the parameters. Since the predicted height of the bump is much larger than the last one, the detection of this PPE is highly feasible. Indeed, the predicted height of the next PPE sensitively changes with the value of $m_{\rm d}$. Thus, the observation may be used to distinguish between the TTV and RV solutions.

Chapter 6

TTV Analysis in the Kepler-51 System and an Anomaly Similar to a Planet-Planet Eclipse Event[1]

6.1 Introduction

This chapter focuses on another multi-transiting system found by *Kepler*, the Kepler-51 (KOI-620) system. This system hosts three transiting planet candidates, two of which were confirmed by Steffen et al. (2013). They made sure that these two planets, Kepler-51b (KOI-620.01) and Kepler-51c (KOI-620.03), are revolving around the same star by confirming that their TTVs are anti-correlated, and showed that they are indeed planetary by giving mass upper limits based on the long-term stability of the system. In this chapter, we perform a numerical analysis of their TTVs to more fully characterize the system and to confirm that the mass of KOI-620.02 is also in the planetary range.

We also discuss a very intriguing light curve of Kepler-51 recently made public on the Space Telescope Science Institute (STScI) MAST archive, which shows a feature similar to a PPE event.

6.2 Stellar and Planet Properties

We adopt the stellar properties in Table 6.1 taken from the NASA Exoplanet Archive.[2] As an initial guess for the limb-darkening coefficients for the quadratic law, we adopt $(u_1, u_2) = (0.36, 0.28)$, the values for $(T_{\rm eff}, \log g, Z, \xi) = (6000\,{\rm K}, 4.5\,{\rm dex}, 0.0, 0.0\,{\rm km/s})$ in the grid of Claret and Bloemen (2011). Linear ephemerides and transit parameters are retrieved from the MAST archive (Table 6.2) as a starting point for the iterative determination of these parameters in Section 6.3.

[1] This chapter is based on Masuda (2014).

[2] `http://exoplanetarchive.ipac.caltech.edu/`

Table 6.1. Stellar Properties of Kepler-51 (KOI-620)

Parameter	Value
$K_{\rm p}$	14.669
$T_{\rm eff}$ (K)	6018 ± 107
$\log g$ (dex)	4.510 ± 0.300
$M_\star(M_\odot)$	1.04 ± 0.12
$R_\star(R_\odot)$	0.940 ± 0.500
Age (Gyr)	0.3 ± 2.3

Table 6.2. Properties of the Kepler-51 System Determined by Other Authors

Parameter	Kepler-51b	Kepler-51c	KOI-620.02
Transit parameters determined by the Kepler team[1]			
t_0 (BJD - 2454833)	159.10435 ± 0.00062	295.321 ± 0.002	212.02345 ± 0.00062
P (days)	45.155503 ± 0.000072	85.31287 ± 0.00096	130.1831 ± 0.00033
$a/R_\star$	63.880 ± 0.640	97.630 ± 0.970	129.400 ± 1.300
$R_p/R_\star$	0.07074 ± 0.00020	0.0573 ± 0.0081	0.0972 ± 0.00024
b	0.030 ± 0.020	0.972 ± 0.028	0.061 ± 0.010
$\rho_\star$(g cm^{-3})		2.42 ± 0.07	
Mass limit from the stability analysis (Steffen et al. 2013)			
Maximum mass ($M_{\rm J}$)	3.23	2.60	-

[1]Data from the MAST archive `http://archive.stsci.edu/kepler/`.

6.3 Analysis of the Transit Light Curves

6.3.1 Data Processing

We analyze the short-cadence ($\sim$ 1 min) Pre-search Data Conditioned Simple Aperture Photometry (PDCSAP) fluxes from Quarters 12 to 16 as well as the long-cadence ($\sim$ 30 min) fluxes from Quarters 1 to 11, for which short-cadence data are not available. We first extract data points within ± 1 day of every transit, and iteratively fit the points outside the transit with a third-order polynomial until all the out-of-transit outliers exceeding 5σ are excluded. Then we divide all the points in the chunk by the best-fit polynomial to give a detrended and normalized transit light curve. Also excluding the transits that are not fully observed, we obtain 30, 11, and 10 transits for Kepler-51b, Kepler-51c, and KOI-620.02, respectively. We note that the Kepler-51b's transit around BJD = 2456346.8 occurred simultaneously with that of KOI-620.02 (double transit). Since this particular transit shows a possible sign of a PPE (Hirano et al. 2012a; Masuda et al. 2013), we will discuss it in more detail in Section 6.5.

6.3.2 Transit Times and Transit Parameters

From the transit light curves obtained in Section 6.3.1, we determine the transit times and transit parameters of the three planets by iterative fit using a Markov chain Monte Carlo (MCMC) algorithm (Section 4.2). We repeat the following two steps: (i) We fit each transit for the time of the transit center t_c using the light curve model by Ohta et al. (2009). Here we assume $e = 0$ and fix the values of P, $R_p/R_\star$, b (of each planet), u_1, u_2, and $\rho_\star$. From the series of transit times, period P and time of a transit center t_0 are extracted by linear regression. (ii) Using the transit times obtained in step (i), we phase fold the transits of each planet and fit the three phase curves simultaneously for $R_p/R_\star$, b (of each planet), u_1, u_2, and $\rho_\star$. Here the values of P are fixed at those in step (i) and $e = 0$ is assumed for all the planets.

Starting from the values in Table 6.2 (and in Section 6.2 for u_1 and u_2), all the parameters converge sufficiently well after five iterations. The resulting transit parameters, ephemerides, and transit times are summarized in Tables 6.3 to 6.6. The quoted best-fit parameters ($a/R_\star$ to $\rho_\star$ and t_c) denote the median values of their posteriors, and uncertainties exclude 15.87% of values at upper and lower extremes. The corresponding best-fit transit models with the phase-folded transits are shown in Figure 6.1. As reported in previous analyses (Steffen et al. 2013; Mazeh et al. 2013), we find significant TTVs for all the three planets as shown in Figure 6.2. Note that the TTV amplitude of KOI-620.02 in our analysis is about twice as large as that first reported by Mazeh et al. (2013), who analyzed the first twelve quarters of *Kepler* data.

Several comments should be added on our revised values of transit parameters in comparison to those in Table 6.2. With the longer baselines, we refine the orbital periods of the three planets with better precision than the previous values. We also find the larger values for $R_p/R_\star$, albeit with relatively large uncertainties; this is because the slight variations of transit depths we identify in the archived light curves, probably due to the star-spot activities (see also the discussion in Section 6.5). In fact, our analysis completely neglects such spot effects, and so the values of $R_p/R_\star$ we determined may be overestimated. The constraint on $R_p/R_\star$ is especially poor for Kepler-51c, whose grazing

Table 6.3. Revised Transit Parameters Obtained from the Phase-folded Transit Light Curves

Parameter	Kepler-51b	Kepler-51c	KOI-620.02
t_0 (BJD − 2454833)	159.10653 ± 0.00033	295.3131 ± 0.0018	212.03246 ± 0.00039
P (days)	45.155314 ± 0.000019	85.31644 ± 0.00022	130.178058 ± 0.000071
$a/R_\star$	$61.5^{+1.5}_{-1.2}$	$94.1^{+2.2}_{-1.9}$	$124.7^{+3.0}_{-2.5}$
$R_p/R_\star$	$0.07414^{+0.00059}_{-0.00061}$	$0.094^{+0.028}_{-0.017}$	$0.10141^{+0.00084}_{-0.00085}$
b	$0.251^{+0.073}_{-0.138}$	$1.017^{+0.034}_{-0.023}$	$0.250^{+0.075}_{-0.141}$
u_1		$0.375^{+0.040}_{-0.036}$	
u_2		$0.311^{+0.083}_{-0.087}$	
$\rho_\star$ (g cm^{-3})		$2.16^{+0.15}_{-0.13}$	
χ^2/d.o.f		12681/12417	

transit causes the strong correlation between its planetary radius and impact parameter. The values of impact parameters we determine are marginally consistent with those in Table 6.2, corresponding to the slightly different value of stellar density; these parameters would be determined more precisely with spectroscopic constraints on the stellar mass and radius.

In addition, we find that the difference between the impact parameters of Kepler-51b and KOI-620.02 is tightly constrained due to the strong correlation, in spite of their relatively large uncertainties: the MCMC posteriors for the two parameters yield $b\,(\text{KOI-620.02}) - b\,(\text{Kepler-51b}) = -0.001 \pm 0.01$. Since this difference is closely related to the minimum separation during a simultaneous transit of the two planets, it has an important role in assessing the occurrence of the PPE, as will be discussed in Section 6.5.

6.4 TTV Analysis

In this section, we perform a numerical analysis of the TTVs for the planetary parameters (especially their masses) to confirm KOI-620.02 as a planet and to more fully characterize the system. For simplicity, we assume the coplanar orbits for the three planets and fix the stellar mass at $M_\star = 1.04 M_\odot$. We make no attempt to model transit parameters other than the transit time.

We define transit centers as the minima of the star-planet distance in the plane of the sky (D), and calculate the simulated transit times in the following way. We integrate the planetary orbits using the fourth-order Hermite scheme with the shared time step (Section 4.1, Kokubo and Makino 2004). From the position and velocity of each planet, we calculate the time derivative of D and search for its root applying the Newton-Raphson method (Fabrycky 2010). All the simulations presented in this section are performed between BJD = 2454980 and BJD = 2456345, beginning at the same epoch T_0(BJD) = 2455720 (close to the center of the observation time).

We fit the three planets' TTVs simultaneously for the mass m, transit time closest to the epoch T_c, orbital period P, eccentricity e, and argument of periastron ω (measured from the sky plane) of each planet. Here P, e, and ω are the osculating orbital elements

Table 6.4. Transit Times of Kepler-51b (KOI-620.01)

Transit Number	t_c (BJD − 2454833)	$1\sigma_{\text{lower}}$	$1\sigma_{\text{lower}}$	χ^2/d.o.f	$O-C$ (days)
0	159.10975	0.00072	0.00072	2.14	0.00323
1	204.26437	0.00078	0.00076	1.86	0.00253
2	249.41453	0.00120	0.00152	3.24	−0.00262
3	294.57446	0.00251	0.00159	2.12	0.00199
4	339.72399	0.00083	0.00088	2.32	−0.00379
5	384.87799	0.00078	0.00079	4.04	−0.00510
6	430.03405	0.00076	0.00076	1.78	−0.00436
8	520.34240	0.00151	0.00168	0.80	−0.00663
9	565.49926	0.00106	0.00148	3.29	−0.00509
10	610.65682	0.00087	0.00095	1.00	−0.00285
11	655.81302	0.00080	0.00084	1.38	−0.00196
12	700.97595	0.00204	0.00156	2.19	0.00566
13	746.12646	0.00082	0.00086	1.10	0.00085
14	791.28654	0.00102	0.00129	1.79	0.00562
15	836.43982	0.00074	0.00074	2.24	0.00358
16	881.59882	0.00072	0.00071	0.91	0.00727
17	926.75475	0.00083	0.00078	1.42	0.00789
18	971.90566	0.00181	0.00262	1.95	0.00348
19	1017.05878	0.00083	0.00088	1.62	0.00129
20	1062.21217	0.00075	0.00075	2.50	−0.00064
21	1107.36887	0.00095	0.00097	0.94	0.00075
22	1152.52090	0.00088	0.00088	0.96	−0.00253
23	1197.67687	0.00097	0.00097	0.87	−0.00188
24	1242.83059	0.00087	0.00087	0.99	−0.00347
25	1287.98482	0.00086	0.00088	0.92	−0.00456
26	1333.14289	0.00091	0.00090	0.95	−0.00179
27	1378.29779	0.00088	0.00088	0.86	−0.00220
28	1423.45442	0.00091	0.00090	1.00	−0.00089
29	1468.61324	0.00089	0.00089	0.97	0.00261

Table 6.5. Transit Times of Kepler-51c (KOI-620.03)

Transit Number	t_c (BJD − 2454833)	$1\sigma_{\text{lower}}$	$1\sigma_{\text{lower}}$	χ^2/d.o.f	$O-C$ (days)
0	295.31257	0.00378	0.00384	0.98	−0.00057
1	380.64295	0.00358	0.00354	0.97	0.01337
2	465.95289	0.00287	0.00283	1.41	0.00687
3	551.26161	0.00319	0.00304	0.99	−0.00086
4	636.56677	0.00324	0.00325	2.04	−0.01214
7	892.51469	0.00384	0.00393	1.90	−0.01355
8	977.84149	0.00360	0.00364	1.16	−0.00319
10	1148.45861	0.00327	0.00327	1.00	−0.01896
11	1233.80785	0.00322	0.00324	0.89	0.01385
12	1319.11072	0.00331	0.00342	0.95	0.00027
14	1489.75414	0.00337	0.00340	0.88	0.01080

Table 6.6. Transit Times of KOI-620.02

Transit Number	t_c (BJD − 2454833)	$1\sigma_{\text{lower}}$	$1\sigma_{\text{lower}}$	χ^2/d.o.f	$O-C$ (days)
0	212.02417	0.00066	0.00066	2.67	−0.00829
1	342.20715	0.00063	0.00062	2.28	−0.00337
2	472.39116	0.00064	0.00064	2.08	0.00258
3	602.57341	0.00063	0.00063	2.17	0.00678
5	862.93196	0.00076	0.00070	3.88	0.00921
6	993.10424	0.00064	0.00065	2.35	0.00343
7	1123.28307	0.00065	0.00066	1.12	0.00420
8	1253.44963	0.00062	0.00063	0.89	−0.00730
9	1383.62994	0.00064	0.00064	0.99	−0.00505

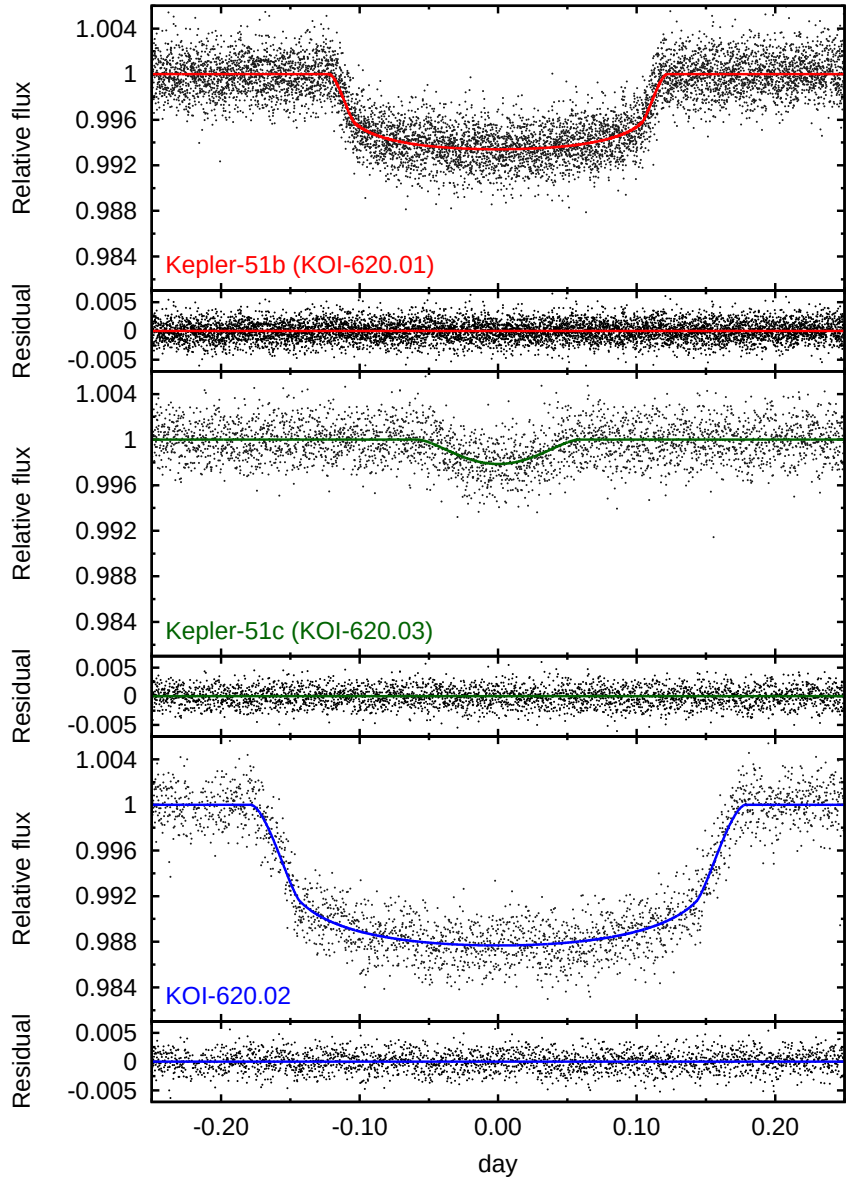

Figure 6.1 Phase-folded transit light curves of Kepler-51b (top), Kepler-51c (middle), and KOI-620.02 (bottom). Black dots are the observed fluxes and colored solid lines show the best-fit models.

Table 6.7. Best-fit parameters obtained from TTVs

Parameter	Kepler-51b	Kepler-51c	KOI-620.02
m ($M_\oplus$)	$2.1^{+1.5}_{-0.8}$	4.0 ± 0.4	7.6 ± 1.1
T_c (BJD $-$ 2454833)	881.5977 ± 0.0004	892.509 ± 0.003	862.9323 ± 0.0004
P (days)	45.1540 ± 0.0002	$85.312^{+0.003}_{-0.002}$	$130.194^{+0.005}_{-0.002}$
$e \cos \omega$	-0.016 ± 0.006	$0.010^{+0.013}_{-0.008}$	$0.005^{+0.011}_{-0.006}$
$e \sin \omega$	-0.04 ± 0.01	$-0.009^{+0.009}_{-0.013}$	$-0.006^{+0.008}_{-0.010}$
χ^2	51 (29 transits)	21 (11 transits)	11 (9 transits)
χ^2/d.o.f		83/34	

Note. — P in this table is one of the osculating orbital elements at the simulation epoch T_0, and so its value is different from the average period obtained from the transits in Table 6.3.

defined at the epoch T_0. Since we assume the coplanar orbits, we fix the initial values of the orbital inclinations $i = \pi/2$ and longitudes of the ascending nodes $\Omega = 0$. Chi-squares are computed from the simulated transit times as

$$\chi^2 = \sum_{j:\,\text{planets}} \sum_{\substack{i:\,\text{observed} \\ \text{transits}}} \left[\frac{t_{c,j}(i) - t^{\rm sim}_{c,j}(i)}{\sigma_j(i)} \right]^2 , \tag{6.1}$$

where $t^{\rm sim}_{c,j}(i)$, $t_{c,j}(i)$, and $\sigma_j(i)$ are the simulated central time, observed central time, and uncertainty of the i-th transit of planet j, respectively. For simplicity, we adopt averages of 1σ upper and lower limits of transit times as $\sigma_j(i)$.[3]

We first use the downhill simplex method by Nelder and Mead (Press et al. 1992) to find the minimum in the above χ^2, and then perform an MCMC analysis (Ford 2005, 2006) around this minimum. The median values of the MCMC posteriors, their 1σ uncertainties, and minimum value of χ^2 are shown in Table 6.7, and the corresponding best-fit simulated TTVs are plotted in Figure 6.2. We perform the same procedures also floating $M_\star$ with the Gaussian prior based on $M_\star = 1.04 \pm 0.12\, M_\odot$ (*c.f.*, Section 4.2.2), and obtain the consistent results with no better constraint on $M_\star$. Analysis taking account of the apparent non-coplanarity of Kepler-51c ($i \sim 89.4°$) does not alter the result, either.

In Figure 6.2, the sinusoidal TTVs of Kepler-51b and KOI-620.02 are well explained by their proximities to 2 : 1 and 3 : 2 resonances, respectively, with Kepler-51c: the periods of these two planets' TTVs inferred from the observed data (~ 770 days and ~ 2500 days) are in well agreement with the "super-period" $P^j = 1/|j/P_{\rm outer} - (j-1)/P_{\rm inner}|$ for a $j : j-1$ resonance defined by Lithwick et al. (2012) (see Equation 3.75). In addition, the best-fit masses of all the three planets, including the one of KOI-620.02, fall into the planetary regime. These facts strongly indicate that KOI-620.02 is a planet belonging to the same system as the other two.

[3]Even taking account of the asymmetry in the posteriors when calculating χ^2, the resulting parameters are consistent with those given here, but the value of χ^2 is slightly reduced.

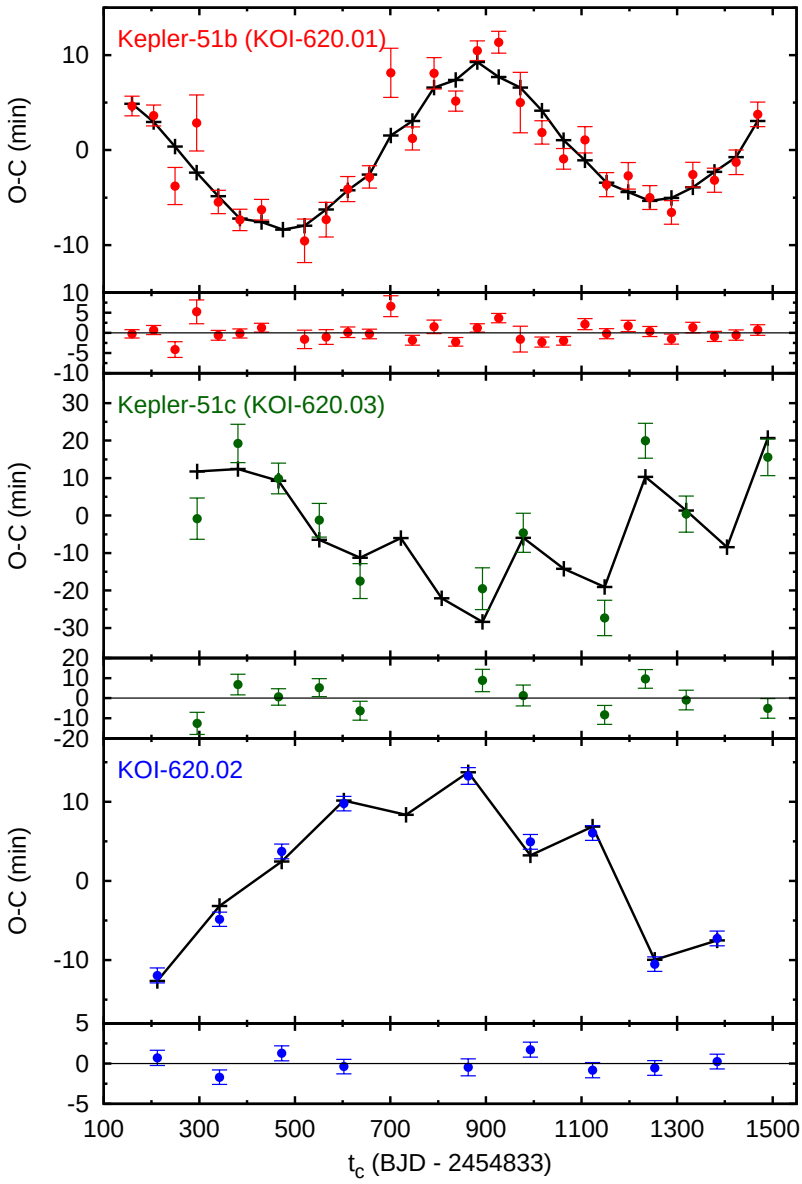

Figure 6.2 Best-fit numerical models (black solid lines) for the observed TTVs (colored points with error bars). Here we adopt the parameters that correspond to the χ^2 minimum, which are slightly different from the median values listed in Table 6.7.

Remarkably, the best-fit masses of all the three planets are less than that of Neptune in spite of their relatively large values of $R_p/R_\star$. At least for the mass of Kepler-51c, our value is also supported by another study: Hadden and Lithwick (2013) analyzed the *Kepler* data through Quarter 12 using analytic TTV formulae derived by Lithwick et al. (2012) (Section 3.2.2). In their formulae, the TTV amplitudes of a pair of coplanar planets in near a $j : j-1$ resonance are analytically given as functions of their masses, eccentricities, and orbital phases. Since the orbital phases are already constrained from transit observations, the formulae allow us to constrain the planets' masses and eccentricities in a degenerate way (*c.f.*, Appendix A). Assuming $e = 0$, they obtain two estimates for the mass of Kepler-51c, one using the inner pair ($9.7\,M_\oplus$) and one using the outer pair ($3.1\,M_\oplus$). Although the non-zero eccentricities easily alter these estimates by a factor of a few (Lithwick et al. 2012), these values are consistent with the mass of Kepler-51c that we obtain here.

Using $\rho_\star = 2.16^{+0.15}_{-0.13}\,\mathrm{g\,cm^{-3}}$ obtained from the transit light curves (Table 6.3) and $M_\star = 1.04 \pm 0.12 M_\odot$, we obtain $R_\star = 0.88 \pm 0.04\,R_\odot$, which is consistent with the value in Table 6.1. Note that $e = 0$ is assumed in determining the value of $\rho_\star$, though the correction is of order $e \sin\omega$ and smaller than the uncertainty of $\rho_\star$ in Table 6.3, according to the TTV results in Table 6.7. This value of $R_\star$, along with the values of $R_p/R_\star$ in Table 6.3 and m in Table 6.7, gives the radius and density of each planet listed in Table 6.8. In addition to the fact that they have relatively large uncertainties, the planetary radii could be slightly overestimated due to the star spots, as discussed in Section 6.3. Nevertheless, these results show that the bulk densities of all the planets in the Kepler-51 system are arguably among the lowest of the known planets, falling below that of the recently discovered sub-Saturn radius planet KOI-152d (Jontof-Hutter et al. 2013).

While their densities are much lower than those of the planets in the solar system, it is possible to form such planets with sufficiently rich gas envelopes. Lopez and Fortney (2013) calculated the radii of low-mass (1-20$M_\oplus$) planets for various values of envelope fraction (0.01-60 %), incident flux (0.1-1000$F_\oplus$), and age (10 Myr-10 Gyr). According to their Equation 3, the observed radii of the Kepler-51 planets can be explained if they have about 10% (Kepler-51b), 30% (Kepler-51c), and 40% (KOI-620.02) of their masses in their H/He envelopes, for the age of 0.3 Gyr. Note that the required H/He fractions increase with the system age, because the older planets tend to have smaller radii for fixed masses due to the gradual cooling of the gas envelopes; this may imply that the host star Kepler-51 is actually young, as suggested by the KIC classification (Table 6.1). This idea is also supported by Walkowicz and Basri (2013), who determined the age of Kepler-51 as 0.53 Gyr, though they note that the ages are highly uncertain for very young stars.

On the other hand, it seems more difficult to explain how they acquired the above fractions of H/He envelopes. Although the simulations by Rogers et al. (2011) (see, *e.g.*, their Table 2) show that such planets could be formed by core-nucleated accretion beyond the snow line followed by the inward migration to $T_{\rm eq} \sim 500\,\mathrm{K}$, their results are based on the somewhat arbitrary assumption that the planet migrates after the sufficient growth of its core and envelope. In situ accretion (Ikoma and Hori 2012) is also unlikely to account for the predicted atmospheric fractions, unless their natal disk was relatively cool and dissipated slowly.

In the above analysis, we adopt the value of $M_\star$ in Table 6.1, but not that of $R_\star$, which is only poorly constrained. More precise determination of the stellar (and hence planetary) mass and radius requires the constraints on the stellar parameters with spectroscopic observations.

Table 6.8. Planet Properties Obtained from Transit Light Curves and TTVs

Parameter	Kepler-51b	Kepler-51c	KOI-620.02
m ($M_\oplus$)	$2.1^{+1.5}_{-0.8}$	4.0 ± 0.4	7.6 ± 1.1
R_p ($R_\oplus$)	7.1 ± 0.3	$9.0^{+2.8}_{-1.7}$	9.7 ± 0.5
ρ_p (g cm^{-3})	$0.03^{+0.02}_{-0.01}$	$0.03^{+0.02}_{-0.03}$	0.046 ± 0.009
a (AU)	0.2514 ± 0.0097	0.384 ± 0.015	0.509 ± 0.020
e	0.04 ± 0.01	$0.014^{+0.013}_{-0.009}$	$0.008^{+0.011}_{-0.008}$
$T_{\rm eq}$ (K)	543 ± 11	439 ± 9	381 ± 8

Note. — We adopt $M_\star = 1.04 \pm 0.12\,M_\odot$ in calculating the values of semi-major axes. Equilibrium temperatures are calculated from $T_{\rm eff}$ in Table 6.1, $a/R_\star$ in Table 6.3, and e using $T_{\rm eq} = \sqrt{R_\star/2a}(1-e^2)^{-1/4}\,T_{\rm eff}$.

6.5 Analysis of the Double-Transit Light Curve: an Anomaly Similar to a PPE Event

In the double transit of Kepler-51b and KOI-620.02 that occurred around BJD = 2456346.8,[4] we identify an increase of the relative flux near the transit center. Considering the fact that KOI-620 shows ~ 12 mmag ($\sim 1\%$) variation associated with its rotation (McQuillan et al. 2013), this "bump" can be naturally explained by a spot-crossing event (*e.g.*, Silva 2003; Silva-Valio 2008; Rabus et al. 2009). Indeed, we find several transits of KOI-620.02 showing brief brightenings of similar amplitudes ($\sim 0.2\,\%$) as seen in this double-transit light curve. In addition, this double transit occurred during a gradual increase of the stellar flux, which indicates that a large star spot (or a group of star spots) was moving on the visible side of the star at that time. However, as we mentioned in the last part of Section 6.3, the small difference of their impact parameters obtained from the transit light curves requires that the PPE *should* have occurred in this double transit, provided that (i) their orbital planes are nearly aligned and that (ii) their cosine inclinations have the same signs. Since the inner planet Kepler-51b overtakes the outer one KOI-620.02 in this double transit, the minimum sky-plane separation becomes small enough under these conditions.

Motivated by this fact, we fit the observed double-transit light curve with the PPE model in Section 5.3 for $\Delta\Omega \equiv \Omega_{02} - \Omega_{\rm b}$, the longitude of the ascending node of KOI-620.02 relative to that of Kepler-51b. Note that here we choose the plane of the sky as a reference plane, and so $\Delta\Omega$ corresponds to the mutual inclination of the two planetary orbits in this plane (see also the lower panel of Figure 6.3). Also note that, in the following, we consider a general case where $\Delta\Omega$ can take any value from $-180°$ to $180°$, though we discussed only the aligned ($\Delta\Omega \sim 0$) case above as a motivation for the PPE scenario. This is because

[4]This transit corresponds to the transit number 30 of Kepler-51b, and number 10 of KOI-620.02. Both of these transits were not used in the TTV analysis in Section 6.4, and so they are not listed in Tables 6.4 and 6.6.

Table 6.9. Resulting Parameters of the PPE Fit to the Double-transit Light Curve

Parameter	Value
Kepler-51b	
$a/R_\star$	63.65 ± 0.33
$R_p/R_\star$	0.0741 ± 0.0017
b	$0.016^{+0.024}_{-0.012}$
t_c(BJD − 2454833)	1513.76694 ± 0.00083
KOI-620.02	
$a/R_\star$	128.93 ± 0.66
$R_p/R_\star$	0.1019 ± 0.0011
b	$0.039^{+0.038}_{-0.040}$
t_c(BJD − 2454833)	1513.78988 ± 0.00070
$\rho_\star$	2.393 ± 0.037
$\Delta\Omega$	$-25.3^{+6.2}_{-6.8}$
χ^2/d.o.f	807/859

Note. — In this fit, the impact parameter of KOI-620.02 is allowed to be either positive or negative, while that of Kepler-51b is fixed to be positive.

the occurrence of a PPE event is generally not limited to the aligned case, as shown in Section 5.4. The other parameters $R_p/R_\star$, b, and $\rho_\star$ are also floated except for u_1 and u_2, which are fixed at the values in Table 6.3. While we restrict the impact parameter b of Kepler-51b to be positive, we allow b of KOI-620.02 to be either positive or negative, taking into account that the two planets can have different signs of cosine inclinations. Using an MCMC algorithm, we find that this model gives a reasonably good fit with χ^2/d.o.f = 0.94, and obtain $\Delta\Omega = -25.3^{+6.2}_{-6.8}$ deg for the sky-plane mutual inclination of the two planets (Figure 6.3 and Table 6.9).

This value, if true, indicates that the orbital planes of Kepler-51b and KOI-620.02 are significantly misaligned, which means either of their orbital axes are tilted with respect to the stellar spin axis. This result may be in contrast to the spin-orbit alignments observed in five multi-transiting systems so far (Sanchis-Ojeda et al. 2012; Hirano et al. 2012b,a; Chaplin et al. 2013; Albrecht et al. 2013), but agrees with the recent discovery that the spin-orbit misalignment is not confined to hot-Jupiter systems (Huber et al. 2013a).

However, if their orbits are really significantly misaligned, it follows that this multi-transiting system is a rare object. For example, the conditional probability $p(02|\mathrm{b})$ that the outer KOI-620.02 transits when the inner Kepler-51b is known to transit is $p(02|\mathrm{b}) \simeq a_{02} \sin\phi/R_\star \sim 1/60$ for the mutual inclination of $\phi \sim 30$ deg and $a_{02}/R_\star \sim 130$ (see, *e.g.*, Ragozzine and Holman 2010). This value is smaller by the factor of $a_\mathrm{b} \sin\phi/R_\star \sim 30$ than in the aligned case, where $p(02|\mathrm{b}) \simeq a_\mathrm{b}/a_{02} \sim 1/2$.

In fact, a further examination of the PPE model reveals that it is consistent with the results of the phase-curve analysis in Section 6.3 only when both planets have $|b| \sim 0$ as in Table 6.9, making this scenario all the less likely. This situation is illustrated in Figure

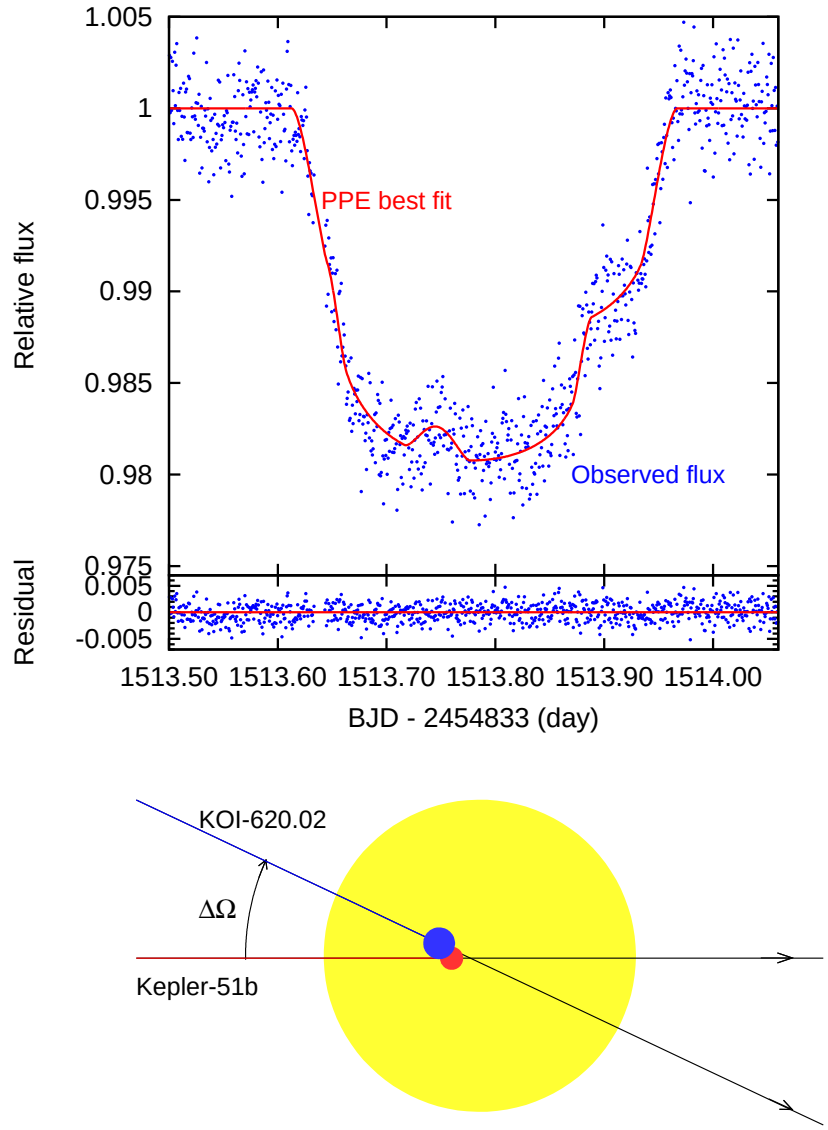

Figure 6.3 Upper: best-fit PPE model (red solid line) for the observed double-transit light curve (blue points). Errors of the observed fluxes are omitted for clarity. Lower: trajectories of the two planets for the best-fit PPE model. This is a snapshot at the time when the two planets are closest in the plane of the sky. An animation of this model is also available at `http://www-utap.phys.s.u-tokyo.ac.jp/~masuda/ppe_animation.gif`.

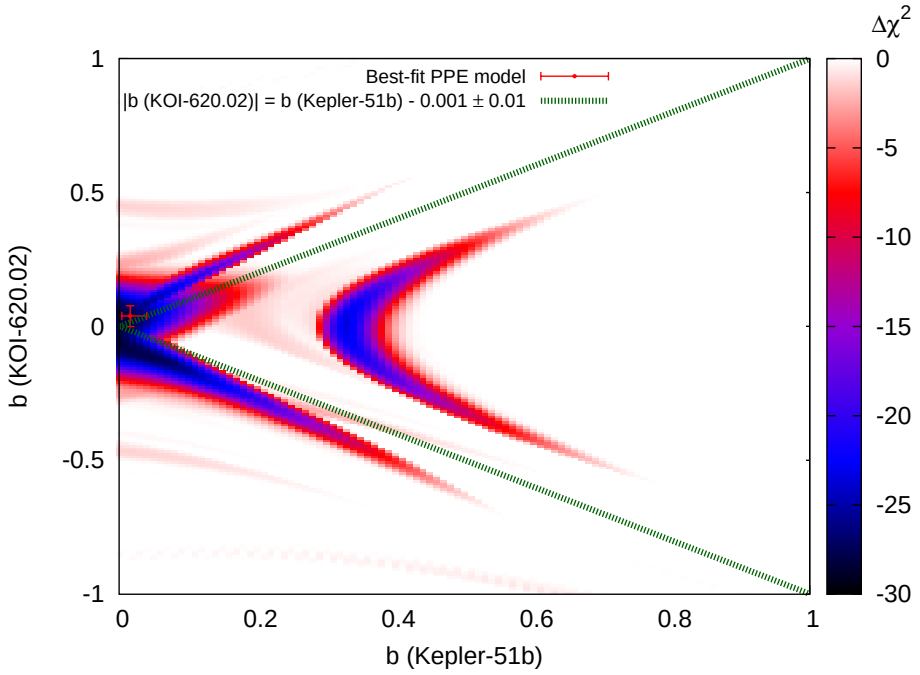

Figure 6.4 A plot to show the region of b(Kepler-51b)-b(KOI-620.02) plane where the PPE model is consistent with the phase-curve analysis. Color scale shows the maximum decrease in χ^2 by including the PPE occurrence into the model; each value is calculated for the grid of the impact parameters at the spacing of 0.01, by varying $\Delta\Omega$ from $-180°$ to $180°$ at the spacing of $1°$. The other transit parameters are fixed at the values in Table 6.9. Dotted green lines correspond to the constraint on the impact parameters of the two planets obtained from the phase-folded transit light curves in Section 6.3, and a red point with error bars denotes the best-fit values of b in Table 6.9. Note that only the region where b(Kepler-51b) > 0 is shown in this figure, because the results are symmetric with respect to $(0, 0)$.

6.4, where we examine the validity of the PPE model for all the possible values of the two planets' impact parameters. In this plot, the color scale shows the minimum value of the χ^2 difference between the PPE and non-PPE models, found by incrementing $\Delta\Omega$ by 1° from -180° to 180°. The grid scale of b is 0.01, and the other parameters are fixed at the best-fit values in Table 6.9. In the dark-blue region, the PPE model significantly improves the fit, while the dotted green lines correspond to the constraint from the phase-folded transits we mentioned in Section 6.3. Comparing these two regions, we find that only the values of b close to the PPE best fit (red point with error bars) are consistent with the PPE interpretation of the bump. Moreover, the impact parameters required by the PPE model are only marginally consistent with those obtained in Section 6.3 (Table 6.3), though they are close to the ones obtained by the *Kepler* team (Table 6.2).

It should also be noted that, if the orbit of the outermost planet has such a large mutual inclination with respect to the inner two, their orbits will precess rapidly. In this case, the resulting transit duration variations (TDVs) would be fairly large for the middle grazing planet, Kepler-51c. Nevertheless, no significant TDVs are apparently seen in the transits of this planet (Figure 6.1). With no constraints on the nodal angle of Kepler-51c, it may still be possible that the orbit of this planet is also tilted with respect to that of Kepler-51b so that the effect of precession is canceled out, but it would require fine tuning of the parameters. Furthermore, we must happen to observe this system when all the planets have small eccentricities as indicated from TTVs, while their eccentricities would vary as the system evolves under such a large mutual inclination.

These arguments about the transit probability, impact parameters, and expected orbital precession, imply that a PPE event that is consistent with all of the observations would be exceedingly rare; in other words, the PPE interpretation for the observed anomaly is essentially refuted. The observed bump is, therefore, probably due to a star spot or just a correlated noise. If it is the spot crossing, the detailed star-spot modeling may provide valuable information on the stellar obliquity (Dittmann et al. 2009; Silva-Valio et al. 2010; Sanchis-Ojeda et al. 2011; Nutzman et al. 2011; Sanchis-Ojeda et al. 2012, 2013), which is closely related to the orbital evolution history of the planets (*e.g.*, Queloz et al. 2000; Winn et al. 2005). This is beyond the scope of the analysis in this chapter.

There are several possible approaches to strengthen the above interpretation of the anomaly. First, follow-up observation of the next double transit where a PPE event might occur is unreasonable, because we have to wait at least until 2092 even if the orbital planes of the two planets are completely aligned. Secondly, the more accurate determination of the impact parameters would be helpful. If it is confirmed that the impact parameters of the two planets differ from zero with better precision, the discussion based on Figure 6.4 is enough to exclude the PPE scenario. In contrast, if both planets have $|b| \sim 0$ as suggested by the *Kepler* team (Table 6.2), we need to explain why the two planets *did not* overlap; if $\Delta\Omega \sim 0$ in this case, we should have observed a large bump that is totally inconsistent with the observed one. In order to better determine the impact parameters, the better constraint on $R_\star$ (or $\rho_\star$ itself) would again be quite beneficial, because the prior knowledge on $\rho_\star$ pins down their values, which are strongly correlated to that of $\rho_\star$. Lastly, as mentioned above, a thorough analysis of the dynamical model taking account of mutual orbital inclinations and (if necessary) star spots would provide a more decisive conclusion on the origin of this anomaly. Yet another possibility is the analysis of the long-term dynamical stability, which may rule out the misaligned configuration.

6.6 Summary of This Chapter

We have discussed the two topics in this chapter, characterization of the multi-transiting planetary system around Kepler-51 with TTV analysis (Sections 6.3 and 6.4) and interpretation of the light-curve feature similar to a PPE caused by the two planets in this system (Section 6.5). Here we briefly summarize each of the topics and give some additional comments.

1. Characterization of the Kepler-51 system.

We analyzed the transit light curves and TTVs of the three planets in the Kepler-51 system, which lie close to a $1:2:3$ resonance chain. Combining the planetary masses obtained from TTVs, and planet-to-star radius ratios and stellar density inferred from the transit light curves, we determined the properties of the three planets as follows: $m_{\rm b} = 2.1^{+1.5}_{-0.8}\,M_\oplus$, $R_{p\rm b} = 7.1 \pm 0.3\,R_\oplus$, $\rho_{p\rm b} = 0.03^{+0.02}_{-0.01}\,{\rm g\,cm^{-3}}$ for Kepler-51b (KOI-620.01), $m_{\rm c} = 4.0 \pm 0.4\,M_\oplus$, $R_{p\rm c} = 9.0^{+2.8}_{-1.7}\,R_\oplus$, $\rho_{p\rm c} = 0.03^{+0.02}_{-0.03}\,{\rm g\,cm^{-3}}$ for Kepler-51c (KOI-620.03), and $m_{02} = 7.6 \pm 1.1\,M_\oplus$, $R_{p02} = 9.7 \pm 0.5\,R_\oplus$, $\rho_{p02} = 0.046 \pm 0.009\,{\rm g\,cm^{-3}}$ for KOI-620.02. From these results, as well as the sinusoidal modulation consistent with their proximities to the resonances, we confirmed KOI-620.02 as a planet in this system (Kepler-51d), which has an equilibrium temperature close to the inner edge of the habitable zone.

The even more remarkable implication of our analysis is that all the three planets in this system have among the lowest densities yet determined, though a more detailed study taking account of the presence of star spots might increase these values. In fact, such low-density planets are frequently seen in other compact multi-transiting planetary systems; these include the systems around Kepler-9 (Holman et al. 2010), Kepler-11 (Lissauer et al. 2011; Migaszewski et al. 2012; Lissauer et al. 2013), Kepler-18 (Cochran et al. 2011), Kepler-30 (Sanchis-Ojeda et al. 2012), Kepler-56 (Huber et al. 2013a), Kepler-79 (Jontof-Hutter et al. 2013), Kepler-87 (Ofir et al. 2013), and Kepler-89 (KOI-94) (Chapter 5, Weiss et al. 2013; Masuda et al. 2013), all of which have planets with sub-Saturn densities. We will discuss this feature in more detail in Chapter 7.

2. Anomaly similar to a planet-planet eclipse event.

We also analyzed the double-transit light curve of Kepler-51b and KOI-620.02 around BJD = 2456346.8. The archived *Kepler* light curve shows a slight increase in the relative flux of Kepler-51, which could be explained by the PPE (planet-planet eclipse), the overlap of the two planets during their double-transit phase.

If the cosine inclinations of the two planets have the same signs, the impact parameters of the two planets strongly suggest that the PPE should have occurred in this double transit. Indeed, the PPE model well reproduces the observed anomaly for the sky-plane mutual inclination between the two planets of $\sim 25\,{\rm deg}$, which implies that their orbital planes are misaligned. This result, if true, indicates that either of their orbital planes are tilted with respect to the stellar spin axis, and makes the Kepler-51 system another important evidence that the spin-orbit misalignment is not confined to hot-Jupiter systems (Huber et al. 2013a).

However, this interpretation of the anomaly seems unlikely for the following reasons. First, such a large mutual inclination significantly reduces the probability that both of Kepler-51b and KOI-620.02 transit. Second, the PPE model is consistent with the result of phase-curve analysis only for limited values of the two planets' impact parameters.

Finally, the misaligned configuration would result in the rapid orbital precession, whose effect should have been readily detectable in the transit light curves of the middle grazing planet, Kepler-51c. Alternative interpretations of the anomaly include the correlated noise and the star-spot crossing. If the latter is the case, it may provide us the information on the stellar obliquity (Dittmann et al. 2009; Silva-Valio et al. 2010; Sanchis-Ojeda et al. 2011; Nutzman et al. 2011; Sanchis-Ojeda et al. 2012, 2013), which is definitely valuable in unveiling the orbital evolution history of the planets in this system.

In any case, it is rewarding to explore the origin of this anomaly, because it serves as an example of the false positive of a PPE event. Compared with the case of the Kepler-89 (KOI-94) system, where small light-curve modulation led to the clear detection of a PPE (Hirano et al. 2012a), the situation is less ideal for the Kepler-51 system analyzed in this chapter. Detailed investigation of the possible phenomena (*e.g.*, star spots) that could produce PPE-like features would help the future detection of this valuable event in such marginal conditions.

Chapter 7

Summary and Future Prospects

In this thesis, we characterized the two multi-transiting planetary systems around KOI-94 (Kepler-89) and Kepler-51, using the archived photometric light curves taken by the *Kepler* space telescope. We performed the dynamical modeling of their transit timing variations (TTVs), the deviations of transit times from the strict periodicity, and constrained the system parameters. In particular, the planetary masses obtained from TTVs are usually inaccessible with the photometric observations alone.

The KOI-94 system is a closely-packed, multi-transiting planetary system that first exhibited a rare event called a "planet-planet eclipse (PPE)." Among the four transiting planets reported before, we considered the TTVs of the outer three planets; we made sure that the innermost planet is too small to affect the TTVs of the other planets at the current level of observational precisions. We numerically fit the observed TTVs of KOI-94c, KOI-94d, and KOI-94e for their masses, eccentricities, and longitudes of periastrons, and obtain the best-fit parameters including the masses of the three planets, $m_{\rm c} = 9.4^{+2.4}_{-2.1} M_\oplus$, $m_{\rm d} = 52.1^{+6.9}_{-7.1} M_\oplus$, and $m_{\rm e} = 13.0^{+2.5}_{-2.1} M_\oplus$. While the resulting parameters are mostly in agreement with the recent RV analysis (Weiss et al. 2013), the mass of KOI-94d estimated from the TTV is significantly smaller than the RV value $m_{\rm d} = 106 \pm 11 M_\oplus$. In addition, we find that the TTV of the outermost planet KOI-94e is not well reproduced in the current modeling, suggesting the existence of another perturber in this system. In fact, the KOI-94 system is the second multi-planetary system for which both RV and TTV observations have been performed, and there has been few observations assuring that both methods really result in consistent solutions.[1] Hence the above discrepancies may pose a general question about possible systematics in either (or both) of the methods.

We also performed a similar TTV analysis in the multi-transiting planetary system around Kepler-51 (KOI-620). This system consists of two confirmed transiting planets, Kepler-51b ($P_{\rm b} = 45.2$ days) and Kepler-51c ($P_{\rm c} = 85.3$ days), and one transiting planet candidate KOI-620.02 ($P_{02} = 130.2$ days), which lie close to a $1:2:3$ resonance chain. Our analysis shows that their TTVs are consistently explained by the three-planet model, and constrain their masses as $m_{\rm b} = 2.1^{+1.5}_{-0.8} M_\oplus$ (Kepler-51b), $m_{\rm c} = 4.0 \pm 0.4 M_\oplus$ (Kepler-51c), and $m_{02} = 7.6 \pm 1.1 M_\oplus$ (KOI-620.02), thus confirming KOI-620.02 as a real planet in this system. These masses inferred from the TTVs are rather small compared with

[1] The first example is the Kepler-18 system, in which both techniques yield marginally consistent results (see Table 8 in Cochran et al. (2011)). Recently, Barros et al. (2014) used radial velocity observations to confirm the non-transiting planet predicted by the TTV analysis (Nesvorný et al. 2013). Both analyses show a good agreement for this case. See also the discussion below.

the planetary radii estimated from the stellar density and planet-to-star radius ratios determined from the transit light curves. Combining these masses and radii, we find that all the three planets in this system are indeed the lowest-density planets ever discovered, having $\rho_p \lesssim 0.05\,\mathrm{g\,cm^{-3}}$.

Both of the systems we analyzed here are typical "dynamically-packed" multi-transiting systems found by *Kepler*: their planets are orbiting in the proximity of the central star, and they often have planet pairs in near mean-motion resonances. In fact, since the planets in such systems show strong dynamical interaction and have relatively short periods, most of the planetary systems characterized with TTVs so far fall into this category. Remarkably, the two systems also resemble each other in that they host planets with densities lower than any planet in our solar system: KOI-94d, KOI-94e, and the three planets in the Kepler-51 system all have $\rho_p \lesssim 0.3\,\mathrm{g\ cm^{-3}}$, which is less than half of the density of Saturn, the least-dense planet in the solar system .

Indeed, low-density planets seem rather common among the *Kepler* planets confirmed with TTV techniques (Table 3.1). Figure 7.1 plots the exoplanetary masses and radii with measured uncertainties. The black circles are all the samples (mostly characterized with RVs), among which the planets found by *Kepler* are shown in red. The blue and green points with error bars are the planets characterized with TTVs (listed in Table 3.1), and green points are the subset characterized in this thesis. In this plot, we see that most of the non-TTV samples have mean densities larger than $\sim 0.1\rho_\oplus = 0.55\,\mathrm{g\ cm^{-3}}$ (dashed brown lines), while many of the TTV samples with $R_p \gtrsim 3R_\oplus$ have $\rho_p \lesssim 0.1\rho_\oplus$. This feature was also pointed out by Jontof-Hutter et al. (2013) and Weiss and Marcy (2013). Weiss and Marcy (2013) performed a t-test to compare the masses from RVs and TTVs for planets with $R_p > 1.5R_\oplus$, and found that the probability that they are drawn from the same distributions is only 9%.

This systematic difference between RV and TTV samples could be due to the sample selection bias, but there has been no quantitative explanations yet. First, it is unlikely that this difference is due to the sample bias of the *Kepler* planets, because the red points (*Kepler* samples other than TTV ones) seem rather uniformly distributed among the black ones in Figure 7.1. Second, Jontof-Hutter et al. (2013) argue that the planets suitable for TTV analysis tend to have lower masses, because they usually belong to dynamically-packed multi-transiting systems as discussed above; if they have too large masses, the system would become dynamically unstable due to the strong gravitational interaction among the planets. However, the mass upper limits based on the long-term stability (Table 3.1) allow a wide range of planetary masses up to $\sim 1000M_\oplus$, questioning the validity of this argument. More quantitative argument requires the stability analyses of specific systems well characterized with TTVs to see whether the planetary masses are really bound by the stability limit or not.

Another possibility is that the TTV method systematically underestimates (or RV method overestimates) the planetary masses for some unknown reason. For example, Weiss and Marcy (2013) mentions the possibility that other unseen planets in the system damp the TTV amplitudes and result in underestimating the planetary masses. However, there are only three systems so far for which both RVs and TTVs have been analyzed. The first example is the Kepler-18 system (Cochran et al. 2011), where the both methods yielded marginally consistent results. The second is the KOI-94 (Kepler-89) system analyzed in this thesis (Weiss et al. 2013; Masuda et al. 2013), in which the results from the two analyses were inconsistent, as discussed in Chapter 5. The third is the Kepler-88

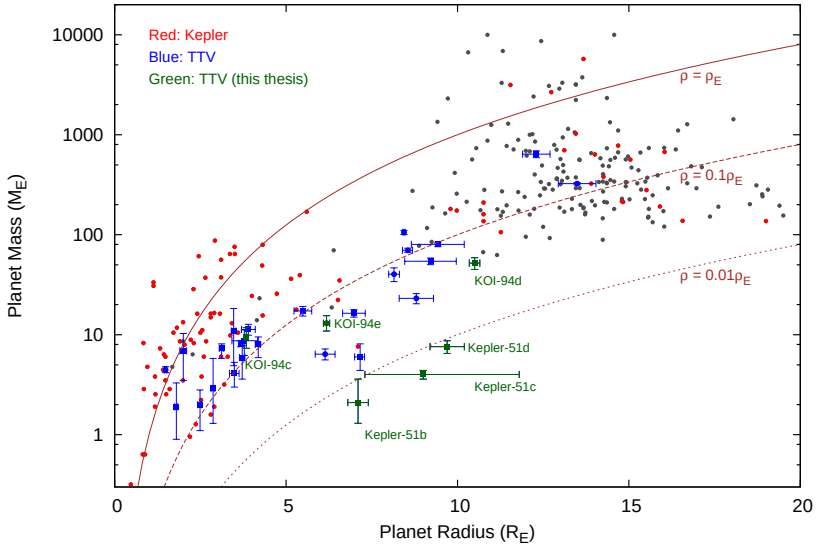

Figure 7.1 Mass-radius diagram of the exoplanets with well-determined masses and radii. Black circles are all the samples, and red circles denote the planets discovered by *Kepler*. These data are retrieved from the NASA Exoplanet Archive `http://exoplanetarchive.ipac.caltech.edu`. The planets characterized with TTVs (listed in Table 3.1) are shown in blue and green points with error bars, the latter of which are analyzed in this thesis. The planets in near $j : j-1$ resonances are plotted with filled squares. The brown lines are the contours of the mean planet density ρ_p: solid, dashed, and dotted lines correspond to $\rho_p = \rho_\oplus$, $0.1\rho_\oplus$, and $0.01\rho_\oplus$, respectively, where $\rho_\oplus = 5.5\,\mathrm{g\ cm^{-3}}$.

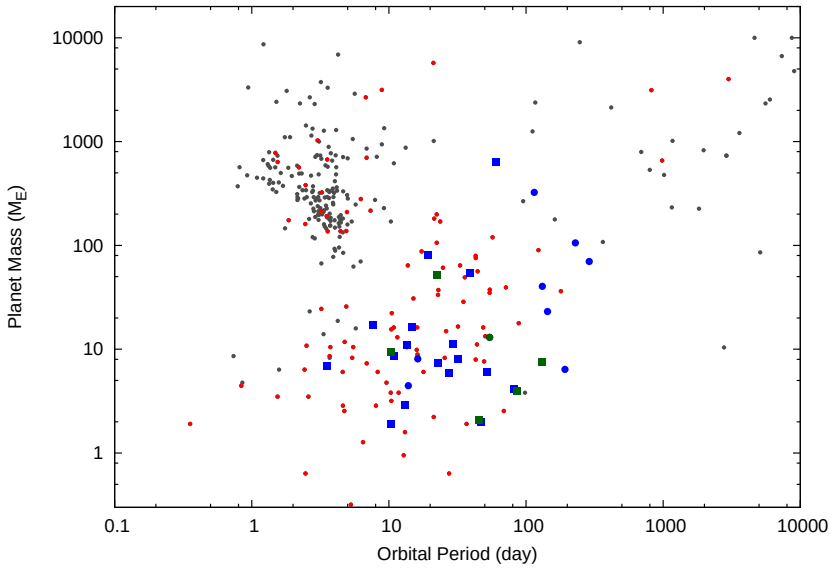

Figure 7.2 Mass-period diagram for the same sample as in Figure 7.1, with the same color code.

system, where RV observations (Barros et al. 2014) confirmed the properties of the non-transiting planet Kepler-88c predicted by the TTV analysis (Nesvorný et al. 2013). It is important, therefore, to increase the number of such samples and to examine to what extent the results of RV and TTV analyses coincide.

On the other hand, it is also possible that the observed low-density feature is not just the sample bias, but results from the formation process of the compact multi-transiting systems. N-body simulations (*e.g.*, Terquem and Papaloizou 2007; Ogihara and Ida 2009; Ogihara et al. 2013) have shown that the compact multi-planetary systems including resonances may form via the convergent disk migrations and resonance capture of the protoplanets, followed by the collisions induced by the disk-gas depletion. In this scenario, the planetary cores lose the gas envelopes due to the collisions, and may again acquire the gas envelopes by *in situ* accretion of the gas from the inner protoplanetary disk (Ikoma and Hori 2012). Although it seems difficult to explain the observed densities of the Kepler-51 planets with the current model, as discussed in Section 6.4, this kind of scenarios suggests that the formation process of dynamically-packed systems may differ from other ones. In the current sample, we see no clear difference between the TTV planets in the first order $(j : j - 1)$ resonances (blue and green squares in Figure 7.1) and the other TTV planets (blue and green circles), but it might be quantified more reliably with a larger number of samples.

The number of exoplanets characterized with TTVs is steadily increasing. With its sensitivity to the low-mass planets and four years of *Kepler* data, TTV techniques have been used to extend the parameter region towards the lower planetary mass and longer orbital period, as can be seen in Figure 7.2. Indeed, it would have been impossible to characterize most of these planets without TTVs, because their host stars are not suitable for spectroscopic observations. The contribution of this technique to future space missions like TESS is also promising. The analysis of TTVs will continue to offer a powerful photometric tool for our future exploration of the exoplanetary world.

Acknowledgments

I gratefully acknowledge my supervisor, Yasushi Suto, without whom this thesis would not have been completed. He gladly took time to discuss with me and patiently listened to my (sometimes rather pathological) worries about my research. Above all, his positive comments and the way he enjoys science have always encouraged me to move forward with my projects. I am also grateful to Teruyuki Hirano, who taught me the way of analyzing *Kepler* data and the fun of studying exoplanets. I also thank Atushi Taruya, Yuka Fujii, and Yuxin Xue, for almost always attending my seminars on exoplanets and motivating me to study this field in more detail. I also express special thanks to other (ex-)members of the University of Tokyo Theoretical Astrophysics group, who made my graduate student's life enjoyable. Finally, I would like to thank my family, who always respected my decision and helped me to study at graduate school.

Appendix A

Analysis of the TTV of KOI-94c using Analytic Formulae

Lithwick et al. (2012) derived analytic formulae for the TTV signals from two coplanar planets near a $j : j-1$ mean motion resonance (see Section 3.2.2). Here we apply these formulae to the TTVs of KOI-94c and KOI-94d, following the procedure in Lithwick et al. (2012).

We let unprimed and primed symbols stand for the quantities associated with inner and outer planets, respectively. Then $\delta t \equiv (\text{observed } t_c) - (t_c \text{ calculated from linear ephemeris})$ for the inner and outer planets are given by

$$\delta t = |V| \sin(\lambda^j + \arg V), \quad \delta t' = |V'| \sin(\lambda^j + \arg V'), \tag{A.1}$$

where λ^j, V, and V' are defined as follows.

The longitude of conjunction λ^j is defined as

$$\lambda^j \equiv j\lambda' - (j-1)\lambda, \tag{A.2}$$

where $\lambda' = 2\pi(t - T')/P'$ and $\lambda = 2\pi(t - T)/P$. If we measure angles with respect to the line of sight, T and T' are the times of any particular transits of the inner and outer planet, respectively. Here we choose $T\,(T')$ to be $t_0\,(t_0')$ in Table 5.7. Defining the super-period P^j and the normalized distance to resonance by

$$P^j \equiv \frac{1}{|j/P' - (j-1)/P|} \tag{A.3}$$

and

$$\Delta \equiv \frac{P'}{P}\frac{j-1}{j} - 1, \tag{A.4}$$

λ^j can be written as

$$\begin{aligned} \lambda^j &= -2\pi\left(\frac{j-1}{P} - \frac{j}{P'}\right)t + 2\pi\left(\frac{(j-1)T}{P} - \frac{jT'}{P'}\right) \\ &= -\frac{\Delta}{|\Delta|}\frac{2\pi}{P^j}\left(t - \frac{(1+\Delta)T - T'}{\Delta}\right). \end{aligned} \tag{A.5}$$

Thus, if $\Delta > 0$, λ^j is retrograde with respect to the orbital motion and is prograde for $\Delta < 0$.

The complex TTV amplitudes V and V' are given by

$$V = P\frac{\mu'}{\pi j^{2/3}(j-1)^{1/3}\Delta}\left(-f - \frac{3}{2}\frac{Z^*_{\rm free}}{\Delta}\right) \tag{A.6}$$

and

$$V' = P'\frac{\mu}{\pi j\Delta}\left(-g + \frac{3}{2}\frac{Z^*_{\rm free}}{\Delta}\right), \tag{A.7}$$

where f and g are the sums of the Laplace coefficients given by

$$f = -1.190 + 2.20\Delta = -1.032 < 0, \quad g = 0.4284 - 3.69\Delta = 0.1637 > 0 \tag{A.8}$$

for $j = 2$, $\Delta = 0.07174$, and $\mu\,(\mu')$ is the mass ratio of the inner (outer) planet to that of the star. They also introduce $Z_{\rm free}$ as a linear combination of the free complex eccentricities of the two planets

$$Z_{\rm free} = f z_{\rm free} + g z'_{\rm free}, \tag{A.9}$$

where $z_{\rm free}$ is defined as the "free" part of the complex eccentricity

$$z \equiv e\exp(i\varpi), \tag{A.10}$$

and obtained by subtracting $z_{\rm forced}$, the forced eccentricity due to the planet's proximity to resonance, from z. The forced eccentricities for the inner and outer planets are

$$\begin{pmatrix} z_{\rm forced} \\ z'_{\rm forced} \end{pmatrix} = -\frac{1}{j\Delta}\begin{pmatrix} \mu' f (P/P')^{1/3} \\ \mu g \end{pmatrix} {\rm e}^{{\rm i}\lambda^j}. \tag{A.11}$$

Since $\Delta \gtrsim 0.01$ and $\mu \lesssim 10^{-4}$ typically, $|z_{\rm forced}| \lesssim 10^{-2}$, in which case

$$Z_{\rm free} \simeq f e {\rm e}^{{\rm i}\varpi} + g e' {\rm e}^{{\rm i}\varpi'} = (f e\cos\varpi + g e'\cos\varpi') + {\rm i}(f e\sin\varpi + g e'\sin\varpi'). \tag{A.12}$$

(Xie 2013a). Note that in either the limit that $|Z_{\rm free}| \ll |\Delta|$ or $|Z_{\rm free}| \gg |\Delta|$, phases of the two planets' TTVs are anti-correlated, as can be seen from the expressions for V and V'. In this case, TTV signals of the two planets provide only three independent quantities, making it impossible to uniquely determine $|V|$, $|V'|$, ${\rm Re}(Z_{\rm free})$, and ${\rm Im}(Z_{\rm free})$.

Above expressions for V and V' imply that the phases as well as the amplitudes of the two TTV signals contain important information about their eccentricities. For ease of discussion, they define

$$\phi_{\rm ttv} \equiv \arg\left(V \times \frac{\Delta}{|\Delta|}\right), \quad \phi'_{\rm ttv} \equiv \arg\left(V' \times \frac{\Delta}{|\Delta|}\right). \tag{A.13}$$

With these definitions, $Z_{\rm free} = 0$ leads to $\phi_{\rm ttv} = 0\,{\rm deg}$ and $\phi'_{\rm ttv} = 180\,{\rm deg}$, independently of the sign of Δ. In this case, since λ^j decreases (increases) with time for $\Delta > 0$ ($\Delta < 0$), δt crosses zero from above (below) whenever $\lambda^j = 0$. If the observed TTVs have a phase shift with respect to $\phi_{\rm ttv} = 0\,{\rm deg}$ and $\phi'_{\rm ttv} = 180\,{\rm deg}$, this implies that non-zero $Z_{\rm free}$ exists. On the other hand, no phase shift does not necessarily mean $Z_{\rm free} = 0$, for the phase of $Z_{\rm free}$ may vanish by chance. Although it is impossible to judge whether $Z_{\rm free}$ is really zero or not in a single resonant pair with no phase shift, important conclusions can be obtained by statistical analyses (Wu and Lithwick 2013).

Table A.1. Complex TTVs for KOI-94c and KOI-94d

Δ	$\lvert V_{\rm c}\rvert$ (days)	$\phi_{\rm ttv,c}$ (deg)	$\lvert V_{\rm d}\rvert$ (days)	$\phi_{\rm ttv,d}$ (deg)	$\chi^2_{\rm c}$/d.o.f	$\chi^2_{\rm d}$/d.o.f
0.07174	0.0045 ± 0.0003	38 ± 3	0.00081 ± 0.00020	253 ± 16	0.85	8.6

Based on the formulation above, the transit times $t_{\rm trans}$ for the inner planet are written as

$$t_{\rm trans} = t_0 + P i_{\rm trans} + {\rm Re}(V)\sin\lambda^j + {\rm Im}(V)\cos\lambda^j, \tag{A.14}$$

where $i_{\rm trans} = 0, 1, \cdots$ is the transit number. For each observed $t_{\rm trans}$, we calculate λ^j using P and t_0 obtained by a linear fit (Table 5.7), and fit for the four parameters t_0, P, ${\rm Re}(V)$, and ${\rm Im}(V)$ by a least-square fit. We also repeat the same procedure for the outer planet, and obtain the results in Table A.1. The best-fit theoretical curve in Figure A.1 shows that the TTV of KOI-94c is well explained only by the effect from KOI-94d, having the same period as expected from their proximity to the 2 : 1 resonance. In contrast, the TTV of KOI-94d is poorly explained by the contribution from KOI-94c alone (Figure A.2). These results are consistent with our estimates in Table 5.8.

TTV amplitudes listed in Table A.1 give estimates for the masses of KOI-94d and KOI-94c. If we assume $Z_{\rm free} = 0$, *i.e.*, that both of the planets have zero eccentricities, Equation (A.6) translates the amplitude of KOI-94c's TTV $\lvert V_{\rm c}\rvert$ into the nominal mass $m_{\rm d} = 63 M_\oplus$.[1] We should note that the accuracy of this estimate is rather limited, because the slight phase shift in KOI-94c's TTV suggests that KOI-94d and/or KOI-94c have small but nonzero eccentricities. Nevertheless, this value is closer to that obtained from the N-body fit to TTVs ($52 \pm 7 M_\oplus$), rather than that obtained from RVs ($106 \pm 11 M_\oplus$), suggesting that KOI-94d also falls into the category of sub-Saturn density planets characterized with TTVs.

[1] $\lvert V_{\rm d}\rvert$ corresponds to a comparatively large nominal mass $m_{\rm c} = 36 M_\oplus$, but this value includes the contributions both from KOI-94c and KOI-94e.

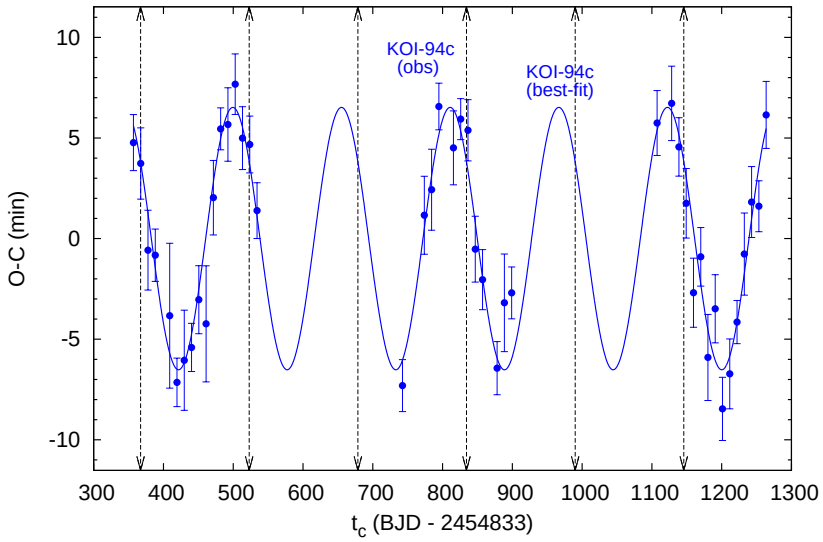

Figure A.1 Best-fit theoretical TTV (solid line) for the observed transit times of KOI-94c based on Equation (A.1) by Lithwick et al. (2012). Points with error bars are the observed TTVs of KOI-94c calculated with t_0 and P obtained from the fit including TTVs (see Equation (A.14)). Vertical arrows show the times at which $\lambda_j = 0$, *i.e.*, the longitude of conjunction points to the observer. The observed phase of the TTV is slightly shifted from these points, suggesting small but nonzero eccentricities.

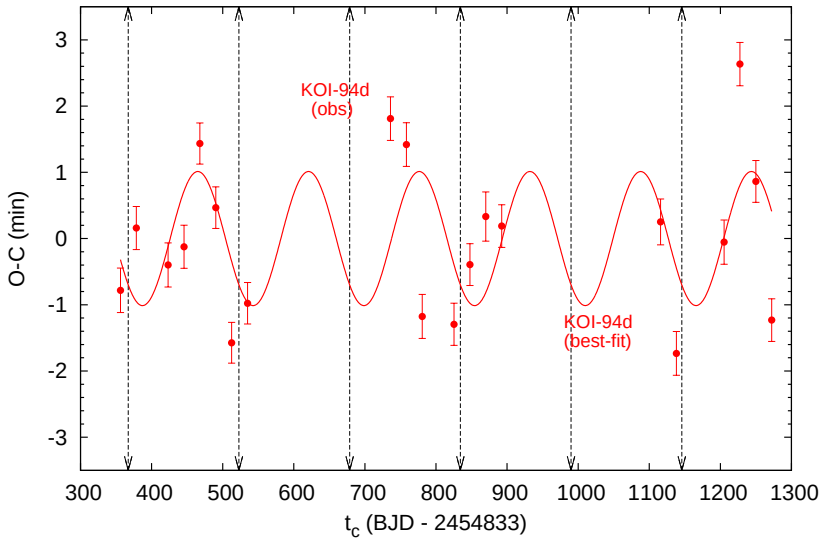

Figure A.2 Best-fit theoretical TTV (solid line) for the observed transit times of KOI-94d based on Equation (A.1) by Lithwick et al. (2012) (same as Figure A.1).

Appendix B

$\mathcal{O}(e)$ Formulation of the PPE

In Section 5.3, we modeled the PPE caused by two planets on circular orbits. Here we summarize how the $\mathcal{O}(e)$ correction modifies those results.

In the presence of a non-zero eccentricity, the impact parameter b is approximately given by Equation (2.43):

$$b = \frac{a\cos i}{R_\star} \cdot \frac{1-e^2}{1+e\sin\omega} \simeq \frac{a\cos i}{R_\star}(1-e\sin\omega). \tag{B.1}$$

This alters the expression (5.9) as

$$\boldsymbol{r}_j \simeq (1-e_j\cos f_j)\begin{pmatrix}\cos\Omega_j & -\sin\Omega_j \\ \sin\Omega_j & \cos\Omega_j\end{pmatrix}\begin{pmatrix}(a_j/R_\star)\cos(\omega_j+f_j) \\ b_j(1+e_j\sin\omega_j)\sin(\omega_j+f_j)\end{pmatrix}. \tag{B.2}$$

In addition, the expansion of $\omega + f$ around t_c (Equation 5.11) is modified as

$$\omega_j + f_j \simeq \frac{\pi}{2} + n_j(1+2e_j\sin\omega_j)(t-t_c^{(j)}). \tag{B.3}$$

Using Equation (B.3), $\boldsymbol{r}_j$ $(j=1,2)$ in Equation (B.2) can be expanded as

$$\boldsymbol{r}_j = \boldsymbol{v}_j\left[(1+e_j\sin\omega_j)(t-t_c^{(j)})\right] + \boldsymbol{r}_0^{(j)}, \tag{B.4}$$

where $\boldsymbol{v}_j$ and $\boldsymbol{r}_0^{(j)}$ are the same as defined in Equation (5.13), but now b is defined as Equation (B.1). Accordingly, the expression for d with $\mathcal{O}(e)$ terms included is obtained by replacing b_j and n_j in the circular case with $b_j(1-e_j\sin\omega_j)$ and $n_j(1+e_j\sin\omega_j)$, respectively.

References

S. J. Aarseth. Direct methods for N-body simulations. In J. U. Brackbill and B. I. Cohen, editors, *Multiple time scales*, pages 377–418, 1985.

E. Agol, J. Steffen, R. Sari, and W. Clarkson. On detecting terrestrial planets with timing of giant planet transits. MNRAS, 359:567–579, May 2005. doi: 10.1111/j.1365-2966.2005.08922.x.

S. Albrecht, J. N. Winn, G. W. Marcy, A. W. Howard, H. Isaacson, and J. A. Johnson. Low Stellar Obliquities in Compact Multiplanet Systems. ApJ, 771:11, July 2013. doi: 10.1088/0004-637X/771/1/11.

G. Anglada-Escudé, M. López-Morales, and J. E. Chambers. How Eccentric Orbital Solutions Can Hide Planetary Systems in 2:1 Resonant Orbits. ApJ, 709:168–178, January 2010. doi: 10.1088/0004-637X/709/1/168.

S. Ballard, D. Fabrycky, F. Fressin, D. Charbonneau, J.-M. Desert, G. Torres, G. Marcy, C. J. Burke, H. Isaacson, C. Henze, J. H. Steffen, D. R. Ciardi, S. B. Howell, W. D. Cochran, M. Endl, S. T. Bryson, J. F. Rowe, M. J. Holman, J. J. Lissauer, J. M. Jenkins, M. Still, E. B. Ford, J. L. Christiansen, C. K. Middour, M. R. Haas, J. Li, J. R. Hall, S. McCauliff, N. M. Batalha, D. G. Koch, and W. J. Borucki. The Kepler-19 System: A Transiting 2.2 R Planet and a Second Planet Detected via Transit Timing Variations. ApJ, 743:200, December 2011. doi: 10.1088/0004-637X/743/2/200.

S. C. C. Barros, R. F. Díaz, A. Santerne, G. Bruno, M. Deleuil, J.-M. Almenara, A. S. Bonomo, F. Bouchy, C. Damiani, G. Hébrard, G. Montagnier, and C. Moutou. SOPHIE velocimetry of Kepler transit candidates. X. KOI-142 c: first radial velocity confirmation of a non-transiting exoplanet discovered by transit timing. A&A, 561:L1, January 2014. doi: 10.1051/0004-6361/201323067.

N. M. Batalha, J. F. Rowe, S. T. Bryson, T. Barclay, C. J. Burke, D. A. Caldwell, J. L. Christiansen, F. Mullally, S. E. Thompson, T. M. Brown, A. K. Dupree, D. C. Fabrycky, E. B. Ford, J. J. Fortney, R. L. Gilliland, H. Isaacson, D. W. Latham, G. W. Marcy, S. N. Quinn, D. Ragozzine, A. Shporer, W. J. Borucki, D. R. Ciardi, T. N. Gautier, III, M. R. Haas, J. M. Jenkins, D. G. Koch, J. J. Lissauer, W. Rapin, G. S. Basri, A. P. Boss, L. A. Buchhave, J. A. Carter, D. Charbonneau, J. Christensen-Dalsgaard, B. D. Clarke, W. D. Cochran, B.-O. Demory, J.-M. Desert, E. Devore, L. R. Doyle, G. A. Esquerdo, M. Everett, F. Fressin, J. C. Geary, F. R. Girouard, A. Gould, J. R. Hall, M. J. Holman, A. W. Howard, S. B. Howell, K. A. Ibrahim, K. Kinemuchi, H. Kjeldsen, T. C. Klaus, J. Li, P. W. Lucas, S. Meibom, R. L. Morris, A. Prša, E. Quintana, D. T. Sanderfer, D. Sasselov, S. E. Seader, J. C. Smith, J. H. Steffen, M. Still, M. C. Stumpe, J. C. Tarter,

P. Tenenbaum, G. Torres, J. D. Twicken, K. Uddin, J. Van Cleve, L. Walkowicz, and W. F. Welsh. Planetary Candidates Observed by Kepler. III. Analysis of the First 16 Months of Data. ApJS, 204:24, February 2013. doi: 10.1088/0067-0049/204/2/24.

M. R. Bate, G. Lodato, and J. E. Pringle. Chaotic star formation and the alignment of stellar rotation with disc and planetary orbital axes. MNRAS, 401:1505–1513, January 2010. doi: 10.1111/j.1365-2966.2009.15773.x.

K. Batygin. A primordial origin for misalignments between stellar spin axes and planetary orbits. Nature, 491:418–420, November 2012. doi: 10.1038/nature11560.

Y. Bétrémieux and L. Kaltenegger. Transmission Spectrum of Earth as a Transiting Exoplanet from the Ultraviolet to the Near-infrared. ApJ, 772:L31, August 2013. doi: 10.1088/2041-8205/772/2/L31.

W. J. Borucki, D. Koch, G. Basri, N. Batalha, T. Brown, D. Caldwell, J. Caldwell, J. Christensen-Dalsgaard, W. D. Cochran, E. DeVore, E. W. Dunham, A. K. Dupree, T. N. Gautier, J. C. Geary, R. Gilliland, A. Gould, S. B. Howell, J. M. Jenkins, Y. Kondo, D. W. Latham, G. W. Marcy, S. Meibom, H. Kjeldsen, J. J. Lissauer, D. G. Monet, D. Morrison, D. Sasselov, J. Tarter, A. Boss, D. Brownlee, T. Owen, D. Buzasi, D. Charbonneau, L. Doyle, J. Fortney, E. B. Ford, M. J. Holman, S. Seager, J. H. Steffen, W. F. Welsh, J. Rowe, H. Anderson, L. Buchhave, D. Ciardi, L. Walkowicz, W. Sherry, E. Horch, H. Isaacson, M. E. Everett, D. Fischer, G. Torres, J. A. Johnson, M. Endl, P. MacQueen, S. T. Bryson, J. Dotson, M. Haas, J. Kolodziejczak, J. Van Cleve, H. Chandrasekaran, J. D. Twicken, E. V. Quintana, B. D. Clarke, C. Allen, J. Li, H. Wu, P. Tenenbaum, E. Verner, F. Bruhweiler, J. Barnes, and A. Prsa. Kepler Planet-Detection Mission: Introduction and First Results. *Science*, 327:977–, February 2010. doi: 10.1126/science.1185402.

W. J. Borucki, D. G. Koch, G. Basri, N. Batalha, T. M. Brown, S. T. Bryson, D. Caldwell, J. Christensen-Dalsgaard, W. D. Cochran, E. DeVore, E. W. Dunham, T. N. Gautier, III, J. C. Geary, R. Gilliland, A. Gould, S. B. Howell, J. M. Jenkins, D. W. Latham, J. J. Lissauer, G. W. Marcy, J. Rowe, D. Sasselov, A. Boss, D. Charbonneau, D. Ciardi, L. Doyle, A. K. Dupree, E. B. Ford, J. Fortney, M. J. Holman, S. Seager, J. H. Steffen, J. Tarter, W. F. Welsh, C. Allen, L. A. Buchhave, J. L. Christiansen, B. D. Clarke, S. Das, J.-M. Désert, M. Endl, D. Fabrycky, F. Fressin, M. Haas, E. Horch, A. Howard, H. Isaacson, H. Kjeldsen, J. Kolodziejczak, C. Kulesa, J. Li, P. W. Lucas, P. Machalek, D. McCarthy, P. MacQueen, S. Meibom, T. Miquel, A. Prsa, S. N. Quinn, E. V. Quintana, D. Ragozzine, W. Sherry, A. Shporer, P. Tenenbaum, G. Torres, J. D. Twicken, J. Van Cleve, L. Walkowicz, F. C. Witteborn, and M. Still. Characteristics of Planetary Candidates Observed by Kepler. II. Analysis of the First Four Months of Data. ApJ, 736:19, July 2011. doi: 10.1088/0004-637X/736/1/19.

C. J. Burke, S. T. Bryson, F. Mullally, J. F. Rowe, J. L. Christiansen, S. E. Thompson, J. L. Coughlin, M. R. Haas, N. M. Batalha, D. A. Caldwell, J. M. Jenkins, M. Still, T. Barclay, W. J. Borucki, W. J. Chaplin, D. R. Ciardi, B. D. Clarke, W. D. Cochran, B.-O. Demory, G. A. Esquerdo, T. N. Gautier, III, R. L. Gilliland, F. R. Girouard, M. Havel, C. E. Henze, S. B. Howell, D. Huber, D. W. Latham, J. Li, R. C. Morehead, T. D. Morton, J. Pepper, E. Quintana, D. Ragozzine, S. E. Seader, Y. Shah, A. Shporer,

P. Tenenbaum, J. D. Twicken, and A. Wolfgang. Planetary Candidates Observed by Kepler IV: Planet Sample From Q1-Q8 (22 Months). *ArXiv e-prints*, December 2013.

J. Cabrera, S. Csizmadia, H. Lehmann, R. Dvorak, D. Gandolfi, H. Rauer, A. Erikson, C. Dreyer, P. Eigmueller, and A. Hatzes. The Planetary System to KIC 11442793: A Compact Analogue to the Solar System. *ArXiv e-prints*, October 2013.

B. Cano and J. M. Sanz-Serna. Error Growth in the Numerical Integration of Periodic Orbits, with Application to Hamiltonian and Reversible Systems. *SIAM J. Numer. Anal.*, 34:1391–1417, August 1997. doi: 10.1137/S0036142995281152.

J. A. Carter, J. C. Yee, J. Eastman, B. S. Gaudi, and J. N. Winn. Analytic Approximations for Transit Light-Curve Observables, Uncertainties, and Covariances. ApJ, 689: 499–512, December 2008. doi: 10.1086/592321.

J. A. Carter, E. Agol, W. J. Chaplin, S. Basu, T. R. Bedding, L. A. Buchhave, J. Christensen-Dalsgaard, K. M. Deck, Y. Elsworth, D. C. Fabrycky, E. B. Ford, J. J. Fortney, S. J. Hale, R. Handberg, S. Hekker, M. J. Holman, D. Huber, C. Karoff, S. D. Kawaler, H. Kjeldsen, J. J. Lissauer, E. D. Lopez, M. N. Lund, M. Lundkvist, T. S. Metcalfe, A. Miglio, L. A. Rogers, D. Stello, W. J. Borucki, S. Bryson, J. L. Christiansen, W. D. Cochran, J. C. Geary, R. L. Gilliland, M. R. Haas, J. Hall, A. W. Howard, J. M. Jenkins, T. Klaus, D. G. Koch, D. W. Latham, P. J. MacQueen, D. Sasselov, J. H. Steffen, J. D. Twicken, and J. N. Winn. Kepler-36: A Pair of Planets with Neighboring Orbits and Dissimilar Densities. *Science*, 337:556–, August 2012. doi: 10.1126/science.1223269.

W. J. Chaplin, R. Sanchis-Ojeda, T. L. Campante, R. Handberg, D. Stello, J. N. Winn, S. Basu, J. Christensen-Dalsgaard, G. R. Davies, T. S. Metcalfe, L. A. Buchhave, D. A. Fischer, T. R. Bedding, W. D. Cochran, Y. Elsworth, R. L. Gilliland, S. Hekker, D. Huber, H. Isaacson, C. Karoff, S. D. Kawaler, H. Kjeldsen, D. W. Latham, M. N. Lund, M. Lundkvist, G. W. Marcy, A. Miglio, T. Barclay, and J. J. Lissauer. Asteroseismic Determination of Obliquities of the Exoplanet Systems Kepler-50 and Kepler-65. ApJ, 766:101, April 2013. doi: 10.1088/0004-637X/766/2/101.

W. J. Chaplin, S. Basu, D. Huber, A. Serenelli, L. Casagrande, V. Silva Aguirre, W. H. Ball, O. L. Creevey, L. Gizon, R. Handberg, C. Karoff, R. Lutz, J. P. Marques, A. Miglio, D. Stello, M. D. Suran, D. Pricopi, T. S. Metcalfe, M. J. P. F. G. Monteiro, J. Molenda-Żakowicz, T. Appourchaux, J. Christensen-Dalsgaard, Y. Elsworth, R. A. García, G. Houdek, H. Kjeldsen, A. Bonanno, T. L. Campante, E. Corsaro, P. Gaulme, S. Hekker, S. Mathur, B. Mosser, C. Régulo, and D. Salabert. Asteroseismic Fundamental Properties of Solar-type Stars Observed by the NASA Kepler Mission. ApJS, 210:1, January 2014. doi: 10.1088/0067-0049/210/1/1.

A. Claret and S. Bloemen. Gravity and limb-darkening coefficients for the Kepler, CoRoT, Spitzer, uvby, UBVRIJHK, and Sloan photometric systems. A&A, 529:A75, May 2011. doi: 10.1051/0004-6361/201116451.

W. D. Cochran, D. C. Fabrycky, G. Torres, F. Fressin, J.-M. Désert, D. Ragozzine, D. Sasselov, J. J. Fortney, J. F. Rowe, E. J. Brugamyer, S. T. Bryson, J. A. Carter, D. R. Ciardi, S. B. Howell, J. H. Steffen, W. J. Borucki, D. G. Koch, J. N. Winn, W. F.

Welsh, K. Uddin, P. Tenenbaum, M. Still, S. Seager, S. N. Quinn, F. Mullally, N. Miller, G. W. Marcy, P. J. MacQueen, P. Lucas, J. J. Lissauer, D. W. Latham, H. Knutson, K. Kinemuchi, J. A. Johnson, J. M. Jenkins, H. Isaacson, A. Howard, E. Horch, M. J. Holman, C. E. Henze, M. R. Haas, R. L. Gilliland, T. N. Gautier, III, E. B. Ford, D. A. Fischer, M. Everett, M. Endl, B.-O. Demory, D. Deming, D. Charbonneau, D. Caldwell, L. Buchhave, T. M. Brown, and N. Batalha. Kepler-18b, c, and d: A System of Three Planets Confirmed by Transit Timing Variations, Light Curve Validation, Warm-Spitzer Photometry, and Radial Velocity Measurements. ApJS, 197:7, November 2011. doi: 10.1088/0067-0049/197/1/7.

J. A. Dittmann, L. M. Close, E. M. Green, and M. Fenwick. A Tentative Detection of a Starspot During Consecutive Transits of an Extrasolar Planet from the Ground: No Evidence of a Double Transiting Planet System Around TrES-1. ApJ, 701:756–763, August 2009. doi: 10.1088/0004-637X/701/1/756.

L. R. Doyle, J. A. Carter, D. C. Fabrycky, R. W. Slawson, S. B. Howell, J. N. Winn, J. A. Orosz, A. Prša, W. F. Welsh, S. N. Quinn, D. Latham, G. Torres, L. A. Buchhave, G. W. Marcy, J. J. Fortney, A. Shporer, E. B. Ford, J. J. Lissauer, D. Ragozzine, M. Rucker, N. Batalha, J. M. Jenkins, W. J. Borucki, D. Koch, C. K. Middour, J. R. Hall, S. McCauliff, M. N. Fanelli, E. V. Quintana, M. J. Holman, D. A. Caldwell, M. Still, R. P. Stefanik, W. R. Brown, G. A. Esquerdo, S. Tang, G. Furesz, J. C. Geary, P. Berlind, M. L. Calkins, D. R. Short, J. H. Steffen, D. Sasselov, E. W. Dunham, W. D. Cochran, A. Boss, M. R. Haas, D. Buzasi, and D. Fischer. Kepler-16: A Transiting Circumbinary Planet. *Science*, 333:1602–, September 2011. doi: 10.1126/science.1210923.

D. C. Fabrycky. Non-Keplerian Dynamics. *ArXiv e-prints*, June 2010.

D. C. Fabrycky and J. N. Winn. Exoplanetary Spin-Orbit Alignment: Results from the Ensemble of Rossiter-McLaughlin Observations. ApJ, 696:1230–1240, May 2009. doi: 10.1088/0004-637X/696/2/1230.

D. C. Fabrycky, E. B. Ford, J. H. Steffen, J. F. Rowe, J. A. Carter, A. V. Moorhead, N. M. Batalha, W. J. Borucki, S. Bryson, L. A. Buchhave, J. L. Christiansen, D. R. Ciardi, W. D. Cochran, M. Endl, M. N. Fanelli, D. Fischer, F. Fressin, J. Geary, M. R. Haas, J. R. Hall, M. J. Holman, J. M. Jenkins, D. G. Koch, D. W. Latham, J. Li, J. J. Lissauer, P. Lucas, G. W. Marcy, T. Mazeh, S. McCauliff, S. Quinn, D. Ragozzine, D. Sasselov, and A. Shporer. Transit Timing Observations from Kepler. IV. Confirmation of Four Multiple-planet Systems by Simple Physical Models. ApJ, 750:114, May 2012. doi: 10.1088/0004-637X/750/2/114.

E. B. Ford. Quantifying the Uncertainty in the Orbits of Extrasolar Planets. AJ, 129: 1706–1717, March 2005. doi: 10.1086/427962.

E. B. Ford. Improving the Efficiency of Markov Chain Monte Carlo for Analyzing the Orbits of Extrasolar Planets. ApJ, 642:505–522, May 2006. doi: 10.1086/500802.

E. B. Ford, D. C. Fabrycky, J. H. Steffen, J. A. Carter, F. Fressin, M. J. Holman, J. J. Lissauer, A. V. Moorhead, R. C. Morehead, D. Ragozzine, J. F. Rowe, W. F. Welsh, C. Allen, N. M. Batalha, W. J. Borucki, S. T. Bryson, L. A. Buchhave, C. J. Burke, D. A. Caldwell, D. Charbonneau, B. D. Clarke, W. D. Cochran, J.-M. Désert, M. Endl,

M. E. Everett, D. A. Fischer, T. N. Gautier, III, R. L. Gilliland, J. M. Jenkins, M. R. Haas, E. Horch, S. B. Howell, K. A. Ibrahim, H. Isaacson, D. G. Koch, D. W. Latham, J. Li, P. Lucas, P. J. MacQueen, G. W. Marcy, S. McCauliff, F. R. Mullally, S. N. Quinn, E. Quintana, A. Shporer, M. Still, P. Tenenbaum, S. E. Thompson, G. Torres, J. D. Twicken, B. Wohler, and Kepler Science Team. Transit Timing Observations from Kepler. II. Confirmation of Two Multiplanet Systems via a Non-parametric Correlation Analysis. ApJ, 750:113, May 2012. doi: 10.1088/0004-637X/750/2/113.

Andrew Gelman, John B. Carlin, Hal S. Stern, and Donald B. Rubin. *Bayesian Data Analysis, Second Edition (Chapman & Hall/CRC Texts in Statistical Science)*. Chapman and Hall/CRC, 2 edition, July 2003. ISBN 158488388X.

P. Goldreich and S. Tremaine. Disk-satellite interactions. ApJ, 241:425–441, October 1980. doi: 10.1086/158356.

H. Goldstein, C. Poole, and J. Safko. *Classical mechanics*. Addison Wesley, 2002.

S. Hadden and Y. Lithwick. Densities and Eccentricities of 163 Kepler Planets from Transit Time Variations. *ArXiv e-prints*, October 2013.

T. Hirano, N. Narita, B. Sato, J. N. Winn, W. Aoki, M. Tamura, A. Taruya, and Y. Suto. Further Observations of the Tilted Planet XO-3: A New Determination of Spin-Orbit Misalignment, and Limits on Differential Rotation. PASJ, 63:L57–L61, December 2011a.

T. Hirano, Y. Suto, J. N. Winn, A. Taruya, N. Narita, S. Albrecht, and B. Sato. Improved Modeling of the Rossiter-McLaughlin Effect for Transiting Exoplanets. ApJ, 742:69, December 2011b. doi: 10.1088/0004-637X/742/2/69.

T. Hirano, N. Narita, B. Sato, Y. H. Takahashi, K. Masuda, Y. Takeda, W. Aoki, M. Tamura, and Y. Suto. Planet-Planet Eclipse and the Rossiter-McLaughlin Effect of a Multiple Transiting System: Joint Analysis of the Subaru Spectroscopy and the Kepler Photometry. ApJ, 759:L36, November 2012a. doi: 10.1088/2041-8205/759/2/L36.

T. Hirano, R. Sanchis-Ojeda, Y. Takeda, N. Narita, J. N. Winn, A. Taruya, and Y. Suto. Measurements of Stellar Inclinations for Kepler Planet Candidates. ApJ, 756:66, September 2012b. doi: 10.1088/0004-637X/756/1/66.

M. J. Holman and N. W. Murray. The Use of Transit Timing to Detect Terrestrial-Mass Extrasolar Planets. *Science*, 307:1288–1291, February 2005. doi: 10.1126/science.1107822.

M. J. Holman, D. C. Fabrycky, D. Ragozzine, E. B. Ford, J. H. Steffen, W. F. Welsh, J. J. Lissauer, D. W. Latham, G. W. Marcy, L. M. Walkowicz, N. M. Batalha, J. M. Jenkins, J. F. Rowe, W. D. Cochran, F. Fressin, G. Torres, L. A. Buchhave, D. D. Sasselov, W. J. Borucki, D. G. Koch, G. Basri, T. M. Brown, D. A. Caldwell, D. Charbonneau, E. W. Dunham, T. N. Gautier, J. C. Geary, R. L. Gilliland, M. R. Haas, S. B. Howell, D. R. Ciardi, M. Endl, D. Fischer, G. Fürész, J. D. Hartman, H. Isaacson, J. A. Johnson, P. J. MacQueen, A. V. Moorhead, R. C. Morehead, and J. A. Orosz. Kepler-9: A System of Multiple Planets Transiting a Sun-Like Star, Confirmed by Timing Variations. *Science*, 330:51–, October 2010. doi: 10.1126/science.1195778.

A. W. Howard. Observed Properties of Extrasolar Planets. *Science*, 340:572–576, May 2013. doi: 10.1126/science.1233545.

A. W. Howard, R. Sanchis-Ojeda, G. W. Marcy, J. A. Johnson, J. N. Winn, H. Isaacson, D. A. Fischer, B. J. Fulton, E. Sinukoff, and J. J. Fortney. A rocky composition for an Earth-sized exoplanet. Nature, 503:381–384, November 2013. doi: 10.1038/nature12767.

D. Huber, J. A. Carter, M. Barbieri, A. Miglio, K. M. Deck, D. C. Fabrycky, B. T. Montet, L. A. Buchhave, W. J. Chaplin, S. Hekker, J. Montalbán, R. Sanchis-Ojeda, S. Basu, T. R. Bedding, T. L. Campante, J. Christensen-Dalsgaard, Y. P. Elsworth, D. Stello, T. Arentoft, E. B. Ford, R. L. Gilliland, R. Handberg, A. W. Howard, H. Isaacson, J. A. Johnson, C. Karoff, S. D. Kawaler, H. Kjeldsen, D. W. Latham, M. N. Lund, M. Lundkvist, G. W. Marcy, T. S. Metcalfe, and J. N. Winn. Stellar Spin-Orbit Misalignment in a Multiplanet System. *ArXiv e-prints*, October 2013a.

D. Huber, V. Silva Aguirre, J. M. Matthews, M. H. Pinsonneault, E. Gaidos, R. A. García, S. Hekker, S. Mathur, B. Mosser, G. Torres, F. A. Bastien, S. Basu, T. R. Bedding, W. J. Chaplin, B.-O. Demory, S. W. Fleming, Z. Guo, A. W. Mann, J. F. Rowe, A. M. Serenelli, M. A. Smith, and D. Stello. Revised Stellar Properties of Kepler Targets for the Quarter 1-16 Transit Detection Run. *ArXiv e-prints*, December 2013b.

M. Ikoma and Y. Hori. In Situ Accretion of Hydrogen-rich Atmospheres on Short-period Super-Earths: Implications for the Kepler-11 Planets. ApJ, 753:66, July 2012. doi: 10.1088/0004-637X/753/1/66.

D. Jontof-Hutter, J. J. Lissauer, J. F. Rowe, and D. C. Fabrycky. KOI-152's Low Density Planets. *ArXiv e-prints*, October 2013.

K. Kinemuchi, T. Barclay, M. Fanelli, J. Pepper, M. Still, and S. B. Howell. Demystifying Kepler Data: A Primer for Systematic Artifact Mitigation. PASP, 124:963–984, September 2012. doi: 10.1086/667603.

E. Kokubo and J. Makino. A Modified Hermite Integrator for Planetary Dynamics. PASJ, 56:861–868, October 2004.

D. Lai, F. Foucart, and D. N. C. Lin. Evolution of spin direction of accreting magnetic protostars and spin-orbit misalignment in exoplanetary systems. MNRAS, 412:2790–2798, April 2011. doi: 10.1111/j.1365-2966.2010.18127.x.

J. J. Lissauer, D. C. Fabrycky, E. B. Ford, W. J. Borucki, F. Fressin, G. W. Marcy, J. A. Orosz, J. F. Rowe, G. Torres, W. F. Welsh, N. M. Batalha, S. T. Bryson, L. A. Buchhave, D. A. Caldwell, J. A. Carter, D. Charbonneau, J. L. Christiansen, W. D. Cochran, J.-M. Desert, E. W. Dunham, M. N. Fanelli, J. J. Fortney, T. N. Gautier, III, J. C. Geary, R. L. Gilliland, M. R. Haas, J. R. Hall, M. J. Holman, D. G. Koch, D. W. Latham, E. Lopez, S. McCauliff, N. Miller, R. C. Morehead, E. V. Quintana, D. Ragozzine, D. Sasselov, D. R. Short, and J. H. Steffen. A closely packed system of low-mass, low-density planets transiting Kepler-11. Nature, 470:53–58, February 2011. doi: 10.1038/nature09760.

J. J. Lissauer, D. Jontof-Hutter, J. F. Rowe, D. C. Fabrycky, E. D. Lopez, E. Agol, G. W. Marcy, K. M. Deck, D. A. Fischer, J. J. Fortney, S. B. Howell, H. Isaacson, J. M. Jenkins, R. Kolbl, D. Sasselov, D. R. Short, and W. F. Welsh. All Six Planets Known to Orbit Kepler-11 Have Low Densities. ApJ, 770:131, June 2013. doi: 10.1088/0004-637X/770/2/131.

Y. Lithwick, J. Xie, and Y. Wu. Extracting Planet Mass and Eccentricity from TTV Data. ApJ, 761:122, December 2012. doi: 10.1088/0004-637X/761/2/122.

E. D. Lopez and J. J. Fortney. Understanding the Mass-Radius Relation for Sub-Neptunes: Radius as a Proxy for Composition. *ArXiv e-prints*, November 2013.

C. Lovis and D. Fischer. Radial Velocity Techniques for Exoplanets. In S. Seager, editor, *Exoplanets*, pages 27–53. Tucson, AZ: University of Arizona Press, 2011.

S. H. Lubow and S. Ida. Planet Migration. In S. Seager, editor, *Exoplanets*, pages 347–371. Tucson, AZ: University of Arizona Press, 2011.

K. Mandel and E. Agol. Analytic Light Curves for Planetary Transit Searches. ApJ, 580: L171–L175, December 2002. doi: 10.1086/345520.

C. B. Markwardt. Non-linear Least-squares Fitting in IDL with MPFIT. In D. A. Bohlender, D. Durand, and P. Dowler, editors, *Astronomical Data Analysis Software and Systems XVIII*, volume 411 of *Astronomical Society of the Pacific Conference Series*, page 251, September 2009.

K. Masuda. Very Low-Density Planets around Kepler-51 Revealed with Transit Timing Variations and an Anomaly Similar to a Planet-Planet Eclipse Event. *ArXiv e-prints*, January 2014.

K. Masuda, T. Hirano, A. Taruya, M. Nagasawa, and Y. Suto. Characterization of the KOI-94 System with Transit Timing Variation Analysis: Implication for the Planet-Planet Eclipse. ApJ, 778:185, December 2013. doi: 10.1088/0004-637X/778/2/185.

M. Mayor and D. Queloz. A Jupiter-mass companion to a solar-type star. Nature, 378: 355–359, November 1995. doi: 10.1038/378355a0.

T. Mazeh, G. Nachmani, T. Holczer, D. C. Fabrycky, E. B. Ford, R. Sanchis-Ojeda, G. Sokol, J. F. Rowe, S. Zucker, E. Agol, J. A. Carter, J. J. Lissauer, E. V. Quintana, D. Ragozzine, J. H. Steffen, and W. Welsh. Transit Timing Observations from Kepler. VIII. Catalog of Transit Timing Measurements of the First Twelve Quarters. ApJS, 208:16, October 2013. doi: 10.1088/0067-0049/208/2/16.

D. B. McLaughlin. Some results of a spectrographic study of the Algol system. ApJ, 60: 22–31, July 1924. doi: 10.1086/142826.

A. McQuillan, T. Mazeh, and S. Aigrain. Stellar Rotation Periods of the Kepler Objects of Interest: A Dearth of Close-in Planets around Fast Rotators. ApJ, 775:L11, September 2013. doi: 10.1088/2041-8205/775/1/L11.

C. Migaszewski, M. Słonina, and K. Goździewski. A dynamical analysis of the Kepler-11 planetary system. MNRAS, 427:770–789, November 2012. doi: 10.1111/j.1365-2966.2012.21976.x.

Y. Ming, L. Hui-Gen, Z. Hui, and Z. Ji-Lin. 8 Planets in 4 Multi-planet Systems via TTVs in 1350 Days. *ArXiv e-prints*, August 2013.

J. Miralda-Escudé. Orbital Perturbations of Transiting Planets: A Possible Method to Measure Stellar Quadrupoles and to Detect Earth-Mass Planets. ApJ, 564:1019–1023, January 2002. doi: 10.1086/324279.

C. D. Murray and A. C. M. Correia. Keplerian Orbits and Dynamics of Exoplanets. In S. Seager, editor, *Exoplanets*, pages 15–23. Tucson, AZ: University of Arizona Press, 2011.

C. D. Murray and S. F. Dermott. *Solar system dynamics*. Cambridge University Press, 1999.

D. Naef, D. W. Latham, M. Mayor, T. Mazeh, J. L. Beuzit, G. A. Drukier, C. Perrier-Bellet, D. Queloz, J. P. Sivan, G. Torres, S. Udry, and S. Zucker. HD 80606 b, a planet on an extremely elongated orbit. A&A, 375:L27–L30, August 2001. doi: 10.1051/0004-6361:20010853.

M. Nagasawa, S. Ida, and T. Bessho. Formation of Hot Planets by a Combination of Planet Scattering, Tidal Circularization, and the Kozai Mechanism. ApJ, 678:498–508, May 2008. doi: 10.1086/529369.

S. Naoz, W. M. Farr, Y. Lithwick, F. A. Rasio, and J. Teyssandier. Hot Jupiters from secular planet-planet interactions. Nature, 473:187–189, May 2011. doi: 10.1038/nature10076.

N. Narita, B. Sato, T. Hirano, and M. Tamura. First Evidence of a Retrograde Orbit of a Transiting Exoplanet HAT-P-7b. PASJ, 61:L35–L40, October 2009.

D. Nesvorný. Transit Timing Variations for Eccentric and Inclined Exoplanets. ApJ, 701:1116–1122, August 2009. doi: 10.1088/0004-637X/701/2/1116.

D. Nesvorný and A. Morbidelli. Mass and Orbit Determination from Transit Timing Variations of Exoplanets. ApJ, 688:636–646, November 2008. doi: 10.1086/592230.

D. Nesvorný, D. M. Kipping, L. A. Buchhave, G. Á. Bakos, J. Hartman, and A. R. Schmitt. The Detection and Characterization of a Nontransiting Planet by Transit Timing Variations. *Science*, 336:1133–, June 2012. doi: 10.1126/science.1221141.

D. Nesvorný, D. Kipping, D. Terrell, J. Hartman, G. Á. Bakos, and L. A. Buchhave. KOI-142, The King of Transit Variations, is a Pair of Planets near the 2:1 Resonance. ApJ, 777:3, November 2013. doi: 10.1088/0004-637X/777/1/3.

P. A. Nutzman, D. C. Fabrycky, and J. J. Fortney. Using Star Spots to Measure the Spin-orbit Alignment of Transiting Planets. ApJ, 740:L10, October 2011. doi: 10.1088/2041-8205/740/1/L10.

A. Ofir, S. Dreizler, M. Zechmeister, and T.-O. Husser. An Independent Planet Search In The Kepler Dataset. II. An extremely low-density super-Earth mass planet around Kepler-87. *ArXiv e-prints*, October 2013.

M. Ogihara and S. Ida. N-Body Simulations of Planetary Accretion Around M Dwarf Stars. ApJ, 699:824–838, July 2009. doi: 10.1088/0004-637X/699/1/824.

M. Ogihara, S.-i. Inutsuka, and H. Kobayashi. Crowding-out of Giants by Dwarfs: An Origin for the Lack of Companion Planets in Hot Jupiter Systems. ApJ, 778:L9, November 2013. doi: 10.1088/2041-8205/778/1/L9.

Y. Ohta, A. Taruya, and Y. Suto. The Rossiter-McLaughlin Effect and Analytic Radial Velocity Curves for Transiting Extrasolar Planetary Systems. ApJ, 622:1118–1135, April 2005. doi: 10.1086/428344.

Y. Ohta, A. Taruya, and Y. Suto. Predicting Photometric and Spectroscopic Signatures of Rings Around Transiting Extrasolar Planets. ApJ, 690:1–12, January 2009. doi: 10.1088/0004-637X/690/1/1.

F. Pepe, A. C. Cameron, D. W. Latham, E. Molinari, S. Udry, A. S. Bonomo, L. A. Buchhave, D. Charbonneau, R. Cosentino, C. D. Dressing, X. Dumusque, P. Figueira, A. F. M. Fiorenzano, S. Gettel, A. Harutyunyan, R. D. Haywood, K. Horne, M. Lopez-Morales, C. Lovis, L. Malavolta, M. Mayor, G. Micela, F. Motalebi, V. Nascimbeni, D. Phillips, G. Piotto, D. Pollacco, D. Queloz, K. Rice, D. Sasselov, D. Ségransan, A. Sozzetti, A. Szentgyorgyi, and C. A. Watson. An Earth-sized planet with an Earth-like density. Nature, 503:377–380, November 2013. doi: 10.1038/nature12768.

W. H. Press, S. A. Teukolsky, W. T. Vetterling, and B. P. Flannery. *Numerical recipes in C. The art of scientific computing*. Cambridge University Press, 1992.

William H. Press, Saul A. Teukolsky, William T. Vetterling, and Brian P. Flannery. *Numerical Recipes 3rd Edition: The Art of Scientific Computing*. Cambridge University Press, New York, NY, USA, 3 edition, 2007. ISBN 0521880688, 9780521880688.

D. Queloz, A. Eggenberger, M. Mayor, C. Perrier, J. L. Beuzit, D. Naef, J. P. Sivan, and S. Udry. Detection of a spectroscopic transit by the planet orbiting the star HD209458. A&A, 359:L13–L17, July 2000.

G. D. Quinlan and S. Tremaine. Symmetric multistep methods for the numerical integration of planetary orbits. AJ, 100:1694–1700, November 1990. doi: 10.1086/115629.

M. Rabus, R. Alonso, J. A. Belmonte, H. J. Deeg, R. L. Gilliland, J. M. Almenara, T. M. Brown, D. Charbonneau, and G. Mandushev. A cool starspot or a second transiting planet in the TrES-1 system? A&A, 494:391–397, January 2009. doi: 10.1051/0004-6361:200811110.

D. Ragozzine and M. J. Holman. The Value of Systems with Multiple Transiting Planets. *ArXiv e-prints*, June 2010.

T. J. Rodigas and P. M. Hinz. Which Radial Velocity Exoplanets Have Undetected Outer Companions? ApJ, 702:716–723, September 2009. doi: 10.1088/0004-637X/702/1/716.

L. A. Rogers, P. Bodenheimer, J. J. Lissauer, and S. Seager. Formation and Structure of Low-density exo-Neptunes. ApJ, 738:59, September 2011. doi: 10.1088/0004-637X/738/1/59.

T. M. Rogers, D. N. C. Lin, and H. H. B. Lau. Internal Gravity Waves Modulate the Apparent Misalignment of Exoplanets around Hot Stars. ApJ, 758:L6, October 2012. doi: 10.1088/2041-8205/758/1/L6.

R. A. Rossiter. On the detection of an effect of rotation during eclipse in the velocity of the brigher component of beta Lyrae, and on the constancy of velocity of this system. ApJ, 60:15–21, July 1924. doi: 10.1086/142825.

R. Sanchis-Ojeda, J. N. Winn, M. J. Holman, J. A. Carter, D. J. Osip, and C. I. Fuentes. Starspots and Spin-orbit Alignment in the WASP-4 Exoplanetary System. ApJ, 733:127, June 2011. doi: 10.1088/0004-637X/733/2/127.

R. Sanchis-Ojeda, D. C. Fabrycky, J. N. Winn, T. Barclay, B. D. Clarke, E. B. Ford, J. J. Fortney, J. C. Geary, M. J. Holman, A. W. Howard, J. M. Jenkins, D. Koch, J. J. Lissauer, G. W. Marcy, F. Mullally, D. Ragozzine, S. E. Seader, M. Still, and S. E. Thompson. Alignment of the stellar spin with the orbits of a three-planet system. Nature, 487:449–453, July 2012. doi: 10.1038/nature11301.

R. Sanchis-Ojeda, J. N. Winn, G. W. Marcy, A. W. Howard, H. Isaacson, J. A. Johnson, G. Torres, S. Albrecht, T. L. Campante, W. J. Chaplin, G. R. Davies, M. N. Lund, J. A. Carter, R. I. Dawson, L. A. Buchhave, M. E. Everett, D. A. Fischer, J. C. Geary, R. L. Gilliland, E. P. Horch, S. B. Howell, and D. W. Latham. Kepler-63b: A Giant Planet in a Polar Orbit around a Young Sun-like Star. ApJ, 775:54, September 2013. doi: 10.1088/0004-637X/775/1/54.

S. Seager and G. Mallén-Ornelas. A Unique Solution of Planet and Star Parameters from an Extrasolar Planet Transit Light Curve. ApJ, 585:1038–1055, March 2003. doi: 10.1086/346105.

A. V. R. Silva. Method for Spot Detection on Solar-like Stars. ApJ, 585:L147–L150, March 2003. doi: 10.1086/374324.

A. Silva-Valio. Estimating Stellar Rotation from Starspot Detection during Planetary Transits. ApJ, 683:L179–L182, August 2008. doi: 10.1086/591846.

A. Silva-Valio, A. F. Lanza, R. Alonso, and P. Barge. Properties of starspots on CoRoT-2. A&A, 510:A25, February 2010. doi: 10.1051/0004-6361/200911904.

J. Southworth, P. J. Wheatley, and G. Sams. A method for the direct determination of the surface gravities of transiting extrasolar planets. MNRAS, 379:L11–L15, July 2007. doi: 10.1111/j.1745-3933.2007.00324.x.

J. H. Steffen, D. C. Fabrycky, E. B. Ford, J. A. Carter, J.-M. Désert, F. Fressin, M. J. Holman, J. J. Lissauer, A. V. Moorhead, J. F. Rowe, D. Ragozzine, W. F. Welsh, N. M. Batalha, W. J. Borucki, L. A. Buchhave, S. Bryson, D. A. Caldwell, D. Charbonneau, D. R. Ciardi, W. D. Cochran, M. Endl, M. E. Everett, T. N. Gautier, R. L. Gilliland, F. R. Girouard, J. M. Jenkins, E. Horch, S. B. Howell, H. Isaacson, T. C. Klaus, D. G.

Koch, D. W. Latham, J. Li, P. Lucas, P. J. MacQueen, G. W. Marcy, S. McCauliff, C. K. Middour, R. L. Morris, F. R. Mullally, S. N. Quinn, E. V. Quintana, A. Shporer, M. Still, P. Tenenbaum, S. E. Thompson, J. D. Twicken, and J. Van Cleve. Transit timing observations from Kepler - III. Confirmation of four multiple planet systems by a Fourier-domain study of anticorrelated transit timing variations. MNRAS, 421: 2342–2354, April 2012. doi: 10.1111/j.1365-2966.2012.20467.x.

J. H. Steffen, D. C. Fabrycky, E. Agol, E. B. Ford, R. C. Morehead, W. D. Cochran, J. J. Lissauer, E. R. Adams, W. J. Borucki, S. Bryson, D. A. Caldwell, A. Dupree, J. M. Jenkins, P. Robertson, J. F. Rowe, S. Seader, S. Thompson, and J. D. Twicken. Transit timing observations from Kepler - VII. Confirmation of 27 planets in 13 multiplanet systems via transit timing variations and orbital stability. MNRAS, 428:1077–1087, January 2013. doi: 10.1093/mnras/sts090.

C. Terquem and J. C. B. Papaloizou. Migration and the Formation of Systems of Hot Super-Earths and Neptunes. ApJ, 654:1110–1120, January 2007. doi: 10.1086/509497.

G. Torres, D. A. Fischer, A. Sozzetti, L. A. Buchhave, J. N. Winn, M. J. Holman, and J. A. Carter. Improved Spectroscopic Parameters for Transiting Planet Hosts. ApJ, 757:161, October 2012. doi: 10.1088/0004-637X/757/2/161.

J. A. Valenti and N. Piskunov. Spectroscopy made easy: A new tool for fitting observations with synthetic spectra. A&AS, 118:595–603, September 1996.

L. M. Walkowicz and G. S. Basri. Rotation periods, variability properties and ages for Kepler exoplanet candidate host stars. MNRAS, 436:1883–1895, December 2013. doi: 10.1093/mnras/stt1700.

L. M. Weiss and G. W. Marcy. The Mass-Radius Relation Between 63 Exoplanets Smaller than 4 Earth Radii. *ArXiv e-prints*, December 2013.

L. M. Weiss, G. W. Marcy, J. F. Rowe, A. W. Howard, H. Isaacson, J. J. Fortney, N. Miller, B.-O. Demory, D. A. Fischer, E. R. Adams, A. K. Dupree, S. B. Howell, R. Kolbl, J. A. Johnson, E. P. Horch, M. E. Everett, D. C. Fabrycky, and S. Seager. The Mass of KOI-94d and a Relation for Planet Radius, Mass, and Incident Flux. ApJ, 768:14, May 2013. doi: 10.1088/0004-637X/768/1/14.

W. F. Welsh, J. A. Orosz, J. A. Carter, D. C. Fabrycky, E. B. Ford, J. J. Lissauer, A. Prša, S. N. Quinn, D. Ragozzine, D. R. Short, G. Torres, J. N. Winn, L. R. Doyle, T. Barclay, N. Batalha, S. Bloemen, E. Brugamyer, L. A. Buchhave, C. Caldwell, D. A. Caldwell, J. L. Christiansen, D. R. Ciardi, W. D. Cochran, M. Endl, J. J. Fortney, T. N. Gautier, III, R. L. Gilliland, M. R. Haas, J. R. Hall, M. J. Holman, A. W. Howard, S. B. Howell, H. Isaacson, J. M. Jenkins, T. C. Klaus, D. W. Latham, J. Li, G. W. Marcy, T. Mazeh, E. V. Quintana, P. Robertson, A. Shporer, J. H. Steffen, G. Windmiller, D. G. Koch, and W. J. Borucki. Transiting circumbinary planets Kepler-34 b and Kepler-35 b. Nature, 481:475–479, January 2012. doi: 10.1038/nature10768.

J. N. Winn. Transits and Occultations. *ArXiv e-prints*, January 2010.

J. N. Winn. Exoplanet Transits and Occultations. In S. Seager, editor, *Exoplanets*, pages 55–77. Tucson, AZ: University of Arizona Press, 2011.

J. N. Winn, R. W. Noyes, M. J. Holman, D. Charbonneau, Y. Ohta, A. Taruya, Y. Suto, N. Narita, E. L. Turner, J. A. Johnson, G. W. Marcy, R. P. Butler, and S. S. Vogt. Measurement of Spin-Orbit Alignment in an Extrasolar Planetary System. ApJ, 631: 1215–1226, October 2005. doi: 10.1086/432571.

J. N. Winn, J. A. Johnson, S. Albrecht, A. W. Howard, G. W. Marcy, I. J. Crossfield, and M. J. Holman. HAT-P-7: A Retrograde or Polar Orbit, and a Third Body. ApJ, 703:L99–L103, October 2009. doi: 10.1088/0004-637X/703/2/L99.

R. A. Wittenmyer, S. Wang, J. Horner, C. G. Tinney, R. P. Butler, H. R. A. Jones, S. J. O'Toole, J. Bailey, B. D. Carter, G. S. Salter, D. Wright, and J.-L. Zhou. Forever Alone? Testing Single Eccentric Planetary Systems for Multiple Companions. ApJS, 208:2, September 2013. doi: 10.1088/0067-0049/208/1/2.

J. T. Wright, G. W. Marcy, A. W. Howard, J. A. Johnson, T. D. Morton, and D. A. Fischer. The Frequency of Hot Jupiters Orbiting nearby Solar-type Stars. ApJ, 753: 160, July 2012. doi: 10.1088/0004-637X/753/2/160.

Y. Wu and Y. Lithwick. Secular Chaos and the Production of Hot Jupiters. ApJ, 735: 109, July 2011. doi: 10.1088/0004-637X/735/2/109.

Y. Wu and Y. Lithwick. Density and Eccentricity of Kepler Planets. ApJ, 772:74, July 2013. doi: 10.1088/0004-637X/772/1/74.

Y. Wu and N. Murray. Planet Migration and Binary Companions: The Case of HD 80606b. ApJ, 589:605–614, May 2003. doi: 10.1086/374598.

J.-W. Xie. Transit Timing Variation of Near-resonance Planetary Pairs: Confirmation of 12 Multiple-planet Systems. ApJS, 208:22, October 2013a. doi: 10.1088/0067-0049/208/2/22.

J.-W. Xie. Transit Timing Variation of Near-Resonance Planetary Pairs. II. Confirmation of 30 planets in 15 Multiple Planet Systems. *ArXiv e-prints*, September 2013b.

J.-W. Xie, Y. Wu, and Y. Lithwick. Frequency of Close Companions among Kepler Planets - a TTV study. *ArXiv e-prints*, August 2013.

V. N. Zharkov and V. P. Trubitsyn. Determination of the equation of state of the molecular envelopes of Jupiter and Saturn from their gravitational moments. *Icarus*, 21:152–156, February 1974. doi: 10.1016/0019-1035(74)90131-6.

富阪幸治・花輪知幸・牧野淳一郎編. シリーズ現代の天文学 *14* シミュレーション天文学. 日本評論社, 2007.

跡部恵子, 酒井圭, 小南淳子, 小林浩, 武田隆顕, 井田茂. 微惑星系、惑星リング系の N 体計算. January 2006.